GEOCHEMISTRY OF MANGANESE OXIDES AND AGE OF MINERALIZATION AT THE SANTA EULALIA MINING DISTRICT, MEXICO

By

Heather Casey

Submitted in partial fulfillment of the requirements
for the Degree of Master of Science in Geology at
New Mexico Institute of Mining and Technology

Earth and Environmental Sciences Department
Socorro, New Mexico
June 2011

ABSTRACT

The Santa Eulalia Mining District, 22 km east of Chihuahua City, is one of the largest silver-lead-zinc producers in Mexico. The significance of this deposit is reflected in the large number of diverse studies on the base metal chimney and mantos deposits. This study focuses on a less studied feature of the district known as the argentiferous manganese oxide mineralization (AMOM) and whether it is part of the main stage of ore mineralization.

Electron microprobe and X-ray diffraction analyses determined the manganese oxide mineralogy consists of cryptomelane, coronadite, birnessite, todorokite mixed with goethite, talc, illite, and other clays. Stable isotope analyses of carbonates within and outside the AMOM indicate clear changes across the contact of manganese altered and unaltered limestone values. For comparison, calcite from the Luis Lopez Manganese District, south of Socorro, New Mexico, was analyzed for carbon and oxygen stable isotopes and was found to show a covariant relationship. Three different samples of AMOM, one cryptomelane and two todorokite, were dated using the $^{40}Ar/^{39}Ar$ method. The dates obtained from step-heating are 10.31 ± 0.13Ma and 10.37 ± 0.11Ma (dendrites) and 9.4 ± 0.5Ma and 9.6 ± 0.4Ma (veins) for the cryptomelane and 5.1 ± 1.7Ma and 1.9 ± 0.4Ma for the todorokites. Four intrusive rock samples from drill hole Cp 1813 were previously dated using K/Ar and were re-dated during this study using $^{40}Ar/^{39}Ar$. From the results obtained, the age of the felsite, quartz monzonite, upper diabase sill, and lower

diabase sill are 33.06 ± 0.11Ma, 38.7 ± 0.6Ma, 73.0 ± 1.3Ma, and 72.3 ± 1.5Ma, respectively.

Previous workers determined the felsites were the source of fluids responsible for the mineralization of the Ag-Pb-Zn (Cu) ore bodies. The ages of the AMOM samples are clearly younger than the main sulfide mineralization. The AMOM is either a weathering product of older sulfide ores or a superimposed mineralization event associated with Basin and Range tectonics.

Keywords: Santa Eulalia, Manganese Oxide, $^{40}Ar/^{39}Ar$ Geochronology, Stable Isotopes

TABLE OF CONTENTS

Page

LIST OF FIGURES……iv

LIST OF TABLES……...x

1. INTRODUCTION……...1
1.1 General Geology of Santa Eulalia……..2
1.1.1 Igneous Intrusions……...4
1.1.2 Ore bodies……...5
1.1.3 Sulfide Mineralization……6
1.1.4 Fluid Inclusions……...7
1.1.5 Stable Isotope Geochemistry……..8
1.1.6 Source of Sulfide Ore Fluids……10
1.1.7 K/Ar Geochronology……11
1.1.8 AMOM of Santa Eulalia……...12
1.2 Dating of Manganese Oxides……...15
1.3 Luis Lopez Manganese District……...19
1.4 Objectives of Current Study……21

2. METHODS……22
2.1 Mineral Identification……..22
2.1.1 Electron Microprobe Analyses……22
2.1.2 X-ray Diffraction Analyses……...23
2.2 Stable Isotope Geochemistry……...24
2.3 $^{40}Ar/^{39}Ar$ Geochronology Sample Preparation and Analyses……..25
2.3.1 Intrusive Rocks Sample Preparation……25
2.3.2 Manganese Oxides Sample Preparation……26
2.3.3 Irradiation Procedures……...27
2.3.4 Analytical Methods……...28

3. RESULTS……..29
3.1 Mineralogical Identification……29
3.1.1 Electron Microprobe Analyses……29
3.1.2 X-ray Diffraction Analyses……...33
3.1.3 Synthesis of Electron Microprobe and X-ray Diffraction……36
3.2 Stable Isotope Geochemistry……...38
3.3 $^{40}Ar/^{39}Ar$ Geochronology……45

3.3.1 Intrusive Rocks……46
3.3.2 Manganese Oxides……54

4. DISCUSSION……59
4.1 Mineralogy and Geochronology of the Intrusive Rocks……..59
4.1.1 Mineral Identification……...59
4.1.2 Geochronology……..60
4.2 Mineralogy and Geochronology of the AMOM……..62
4.2.1 Mineral Identification……...62
4.2.2 Geochronology……..63
4.3 Stable Isotope at Santa Eulalia……64
4.4 The Origin of AMOM……..66
4.4.1 Weathering Model for AMOM at Santa Eulalia……...66
4.4.2 Hot Spring Model for AMOM at Santa Eulalia……67
4.5 Stable Isotopes at Luis Lopez……..72

5. CONCLUSION……..75

APPENDIX A. SAMPLE PHOTOS……77

APPENDIX B. ELECTRON MICROPROBE ANALYSES……85

APPENDIX C. X-RAY DIFFRACTION……..91
C.1 Intrusive Rocks……91
C.2 Manganese Oxides……100

APPENDIX D. STABLE ISOTOPES……112

APPENDIX E. $^{40}AR/^{39}AR$ GEOCHRONOLOGY……115
E.1 Intrusive Rocks Data……115
E.1.1 Data Tables……115
E.1.2 Step-heating Spectra……...119
E.1.3 Isochrons……122
E.2 Manganese Oxides Data……125
E.2.1 Data Tables……125
E.2.2 Step-heating Spectra……...128
E.2.3 Isochrons……129

REFERENCES……133

LIST OF FIGURES

Page

Figure 1-1: Area map. Modified from (Haynes and Kesler, 1988)……..…1

Figure 1-2: Stratigraphic column for the Sierra Santa Eulalia, Chihuahua, Mexico with K/Ar dates and sulfur isotopes (Megaw, 1990) …….……3

Figure 1-3: Schematic drawing of the cross-cutting relationships between the felsites and diabase sills and the lamprophyres……...11

Figure 1-4: Conceptual model for the hydrothermal formation of the Luis Lopez Manganese District, New Mexico…….....15

Figure 1-5: Coronadite Group crystal structure. The elements in the tunnel site indicate this is the mineral cryptomelane……....17

Figure 1-6: Location of the Luis Lopez Manganese District in New Mexico…….....19

Figure 2-1: Photograph of the SE-PKM-1 thin section used for microprobe analyses….27

Figure 3-1: All microprobe analyses plotted with %K_2O versus %MnO…….….30

Figure 3-2: Relationship of manganese oxides and other minerals in SE-PKM microprobe backscatter image……...30

Figure 3-3: Microprobe data using data points with at least 44% MnO and at least 2% of one of the components, eliminating high Fe or Ca data points and trace elements……...32

Figure 3-4: Microprobe data using points with at least 44% MnO and at least 2% of one of the components, eliminating high Fe, high Ca data points and analyses with K_2O, PbO, and ZnO less than 2%.....33

Figure 3-5: SE-PKM-1 scans of separates dated using the $^{40}Ar/^{39}Ar$ method……...34

Figure 3-6: The two todorokite separates dated using the $^{40}Ar/^{39}Ar$ method……35

Figure 3-7: Flow chart of proceses followed to identify the minerals in the AMOM…...37

Figure 3-8: Microprobe data $\%K_2O$ vs. % MnO plotted by inferred mineral…...……38

Figure 3-9: $\delta^{13}C$ vs. $\delta^{18}O$ values for calcite and limestone (Megaw, 1990) and new limestone samples (this study) for Santa Eulalia……...40

Figure 3-10: Santa Eulalia $\delta^{13}C$ plotted against distance from ore veins in meters (Megaw, 1990)……...40

Figure 3-11: Santa Eulalia $\delta^{18}O$ plotted against distance from ore veins in meters (Megaw, 1990)……...41

Figure 3-12: $\delta^{13}C$ and $\delta^{18}O$ values of calcite for Luis Lopez and Water Canyon, New Mexico……...41

Figure 3-13: Luis Lopez data with $\delta^{13}C_{HCO3-}$ vs. $\delta^{18}O_{H2O}$…….42

Figure 3-14: $\delta^{13}C$ vs. $\delta^{18}O$ of calcite of seven rocks at the MCA mine…….43

Figure 3-15: $\delta^{13}C$ vs. $\delta^{18}O$ of calcite from two rocks at Nogal Canyon……44

Figure 3-16: $\delta^{13}C$ vs. $\delta^{18}O$ of calcite of two rocks at the Black Canyon mine……..44

Figure 3-17: $\delta^{13}C$ vs. $\delta^{18}O$ of calcite of six rocks at Water Canyon……..45

Figure 3-18: West-East cross-section of drill hole Cp1813, looking North……..…46

Figure 3-19: $^{40}Ar/^{39}Ar$ Step-Heating Spectra for Runs 59516-01, 59517-01 (Felsic Core). Plagioclase (black) and groundmass (red)…….48

Figure 3-20: $^{40}Ar/^{39}Ar$ Step-Heating Spectra for Runs 59518-01, 59519-05 (Cp1813 2070'). Plagioclase (black) and K-feldspar (red)……...49

Figure 3-21: Inverse Isochron for Run 59518-01 (Cp 1813 2070', plagioclase)……...50

Figure 3-22: Inverse Isochron for Run 59519-05 (Cp 1813 2070', K-feldspar)……...50

Figure 3-23: $^{40}Ar/^{39}Ar$ Step-Heating Spectra for Runs 59511-01, 59514-01, 59516-01 (Cp1813 92', Core 1, and Felsic Core). Cloudy plagioclase from Cp1813 92' (black), Core 1(red), and Felsic Core (green)…….51

Figure 3-24: $^{40}Ar/^{39}Ar$ Step-Heating Spectra for Runs 59510-01, 59513-01 (Cp1813 92' and Core 1). Separates from Cp1813 92' (black) and Core 1 (red) initially thought to be clear plagioclase…….53

Figure 3-25: $^{40}Ar/^{39}Ar$ Step-Heating Spectra for Runs 59512-01, 59515-01 (Cp1813 92' and Core 1). Biotite from Cp1813 92' (black) and Core 1 (red)……...54

Figure 3-26: $^{40}Ar/^{39}Ar$ Step-Heating Spectra for SE-PKM-1: a) Runs 59771-01 and 59772-02 (veins); b) Runs 59773-01 and 59774-01 (dendrites)……56

Figure 3-27: $^{40}Ar/^{39}Ar$ Step-Heating Spectra for Runs 59775-01, 59776-01 (SE-bulk and SE-PGE). Todorokite from SE-bulk (black) and SE-PGE (red)……58

Figure 4-1: K/Ar (black) (Clark et al., 1979; Megaw, 1990) and $^{40}Ar/^{39}Ar$ (red) age distribution for the intrusive rocks…….62

Figure 4-2: Relationship of carbon and oxygen isotope values within AMOM and unaltered limestone. Courtesy of Megaw (1990)……...65

Figure 4-3: Schematic weathering model for the formation of AMOM based on Spurr (1911) and observations of Megaw (1990)……67

Figure 4-4: Location of Santa Eulalia, outlined in black, and Peña Blanca, outlined in red, near Chihuahua, Mexico (Mexicana, 1985)……...68

Figure 4-5: Model for deep fluid circulation and precipitation of hydrothermal minerals in faults (Lueth et al., 2005)……...69

Figure 4-6: Schematic cross-section of possible relationships between RGR, manganese, and hot spring mineralization……71

Figure 4-7: Schematic model for the precipitation of AMOM at Santa Eulalia with fluid movement based on Mailloux et al. (1999) (red) and fluid movement based on basin dewatering-MVT type from the east (blue)……...72

Figure A-1: SEPKM rock sample……..77

Figure A-2: SEPGD rock sample……...77

Figure A-3: SEPGE rock sample……...77

Figure A-4: SE-bulk rock sample……..78

Figure A-5: MCA-1 rock sample……...78

Figure A-6: MCA-2 rock sample……...78

Figure A-7: MCA-3 rock sample……...79

Figure A-8: MCA-4 rock sample……...79

Figure A-9: MCA-5 rock sample……...79

Figure A-10: MCA-6 rock sample…….80

Figure A-11: MCA-7 rock sample…….80

Figure A-12: Nogal-1 rock sample……80

Figure A-13: Nogal-2 rock sample……81

Figure A-14: PG-1 rock sample…….81

Figure A-15: PG-2 rock sample…….81

Figure A-16: BC-1 rock sample……82

Figure A-17: BC-2 rock sample…….82

Figure A-18: Nancy #9189 rock sample, 15.5cm (6 in) across…….82

Figure A-19: 003301 rock sample…….83

Figure A-20: 003303 rock sample…….83

Figure A-21: 003304 rock sample…….83

Figure A-22: 003304A rock sample……..84

Figure A-23: 003304B rock sample……...84

Figure A-24: 003308 rock sample…….84

Figure C-1: “Clear plagioclase” from Cp1813 92’……91

Figure C-2: “Clear plagioclase” from Core 1……92

Figure C-3: “Cloudy plagioclase” from Felsic core……..94

Figure C-4: “Cloudy plagioclase” from Cp1813 2070’…….95

Figure C-5: “Cloudy plagioclase” from Cp1813 92’…….96

Figure C-6: “Cloudy plagioclase” from Core 1…….97

Figure C-7: “K-feldspar”from Cp1813 2070’……97

Figure C-8: Biotite from Cp1813 92’……98

Figure C-9: Biotite from Core 1…….98

Figure C-10: SE-PKM-1, vein A…….102

Figure C-11: SE-PKM-1, vein A hard…….104

Figure C-12: SE-PKM-1, cluster D…….106

Figure C-13: SE-PKM-1, dendrite E……...108

Figure C-14: SE-bulk-1, dendrite A…….110

Figure C-15: SE-PGE-1, dendrite A……111

Figure D-1: Mexican calcite plotted with a) $\delta^{13}C$ and b) $\delta^{18}O$……112

Figure D-2: Correction curves for data a) $\delta^{13}C$, b) $\delta^{18}O$……..112

Figure E-1: Step-heating spectra for Felsic core……..119

Figure E-2: Step-heating spectra for Cp1813 2070’……119

Figure E-3: Step-heating spectra for Cp1813 92'……120

Figure E-4: Step-heating spectra for Core 1……121

Figure E-5: Inverse Isochron for Run 59516-01 (Felsic Core, plagioclase)……122

Figure E-6: Inverse Isochron for Run 59517-01 (Felsic Core, groundmass)……..122

Figure E-7: Inverse Isochron for Run 59518-01 (Cp 1813 2070', plagioclase)……..122

Figure E-8: Inverse Isochron for Run 59519-05 (Cp 1813 2070', K-feldspar)……...123

Figure E-9: Inverse Isochron for Run 59511-01 (Cp 1813 92', cloudy plagioclase)…..123

Figure E-10: Inverse Isochron for Run 59514-01 (Core 1, cloudy plagioclase)…….123

Figure E-11: Inverse Isochron for Run 59513-01 (Core 1, clear plagioclase)…….124

Figure E-12: Inverse Isochron for Run 59510-01 (Cp 1813 92', clear plagioclase)…...124

Figure E-13: Inverse Isochron for Run 59512-01 (Cp 1813 92', biotite)……124

Figure E-14: Inverse Isochron for Run 59515-01 (Core 1, biotite)…….125

Figure E-15: Step-heating spectra for SE-PKM……..128

Figure E-16: Step-heating spectra from SE-bulk and SE-PGE……...129

Figure E-17: Inverse isochron for SE-PKM-1 vein A…….129

Figure E-18: Inverse isochron for SE-PKM-1 vein A (hard)……..130

Figure E-19: Inverse isochron for SE-PKM-1 dendrite D……...130

Figure E-20: Inverse isochron for SE-PKM-1 dendrite E……...131

Figure E-21: Inverse isochron for SE-bulk……..131

Figure E-22: Inverse isochron for SE-PGE…….132

LIST OF TABLES

Page

Table 3-1: Manganese oxide minerals and formulas (Vasconcelos, 1999; Back and Mandarino, 2008)……...33

Table 3-2: Minerals identified in six manganese oxide separates…….35

Table B-1: Microprobe data for SE-PKM-1, SE-PGD, SE-PGE-1, SE-PGE-2, SE-bulk-1, SE-bulk-2, and SE-bulk-3……..85

Table D-1: Isotope standards……...112

Table D-2: All Luis Lopez and Santa Eulalia data……..112

Table E-1: Argon isotopic data for intrusive separates……115

Table E-2: Argon isotopic data for manganese oxide separates……..125

This thesis is accepted on behalf of the
Faculty of the Institute by the following committee:

_____

Advisor

_____

_____

_____

_____

_____

Date

I release this document to the New Mexico Institute of Mining and Technology.

_____

Student's Signature Date

1. INTRODUCTION

The Santa Eulalia District is located approximately 22 kilometers east of Chihuahua City, Mexico (Figure 1-1) and is one of the most extensively studied base metal manto deposits in the world (Megaw, 1990). Santa Eulalia is an important silver-lead-zinc district that has been mined for hundreds of years (Hewitt, 1968). Previous workers noted a close relationship between the felsite intrusions and the sulfide mineralization. This study addresses the question of whether a less studied part of the deposit, known as the argentiferous manganese oxide mineralization (AMOM), is part of the main stage of ore mineralization. If the AMOM is part of the main ore stage, it may provide a broad alteration halo for further exploration of the sulfide deposits.

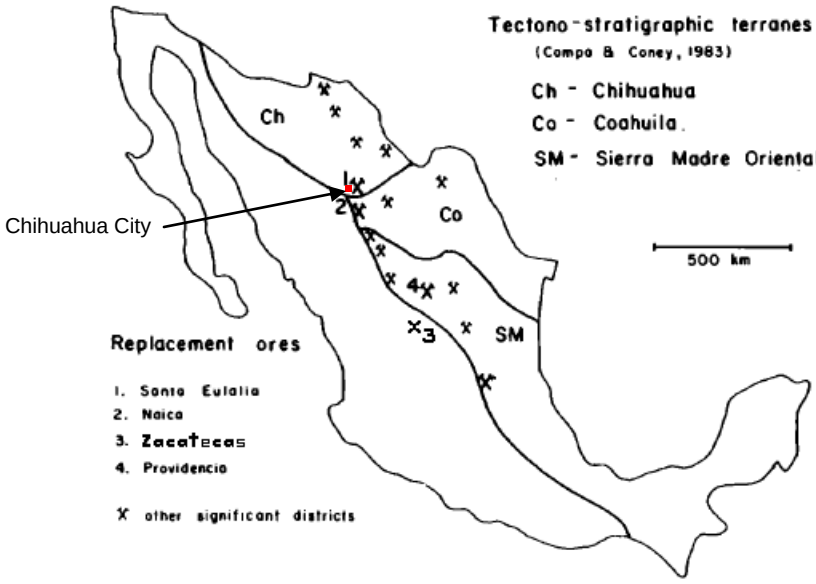

Figure 1-1: Area map. Modified from (Haynes and Kesler, 1988).

1.1 General Geology of Santa Eulalia

Aspects of previous work include field observations of mineral location (Spurr, 1911; Prescott, 1916; Walker and Walker, 1956; Hewitt, 1968), type of ore bodies (Hewitt, 1968; Megaw, 1986b; Megaw, 1990), and mineral zoning (Spurr, 1911; Prescott, 1916; Hewitt, 1968; Malakhov, 1968; Walter, 1985; Bond, 1986; Aguirre, 1987; Megaw, 1990; Lueth et al., 2000). Other work has been done in fluid inclusions (Megaw, 1990), stable isotopes (Ohmoto, 1972; Miranda and Megaw, 1986; Megaw, 1990), and K/Ar dating (Clark et al., 1979; Megaw, 1990).

The Santa Eulalia District is separated into two sub-distinct areas known as the West Camp and the East Camp. Both areas are located within the Sierra Santa Eulalia close to a major tectonic boundary (Figure 1-1). The rock units of the Sierra Santa Eulalia (Figure 1-2) include lower Cretaceous limestone and evaporites folded into a doubly plunging anticline, which were then covered by lower Tertiary volcanic and volcaniclastic rocks. Mid-Tertiary ash-flow tuffs and basalts from the Santo Domingo Caldera overlie the lower Tertiary volcanic rocks. The sierra extends 30 km from north to south and 18 km from east to west (Hewitt, 1968; Campa, 1985; Megaw, 1986b; Megaw, 1990).

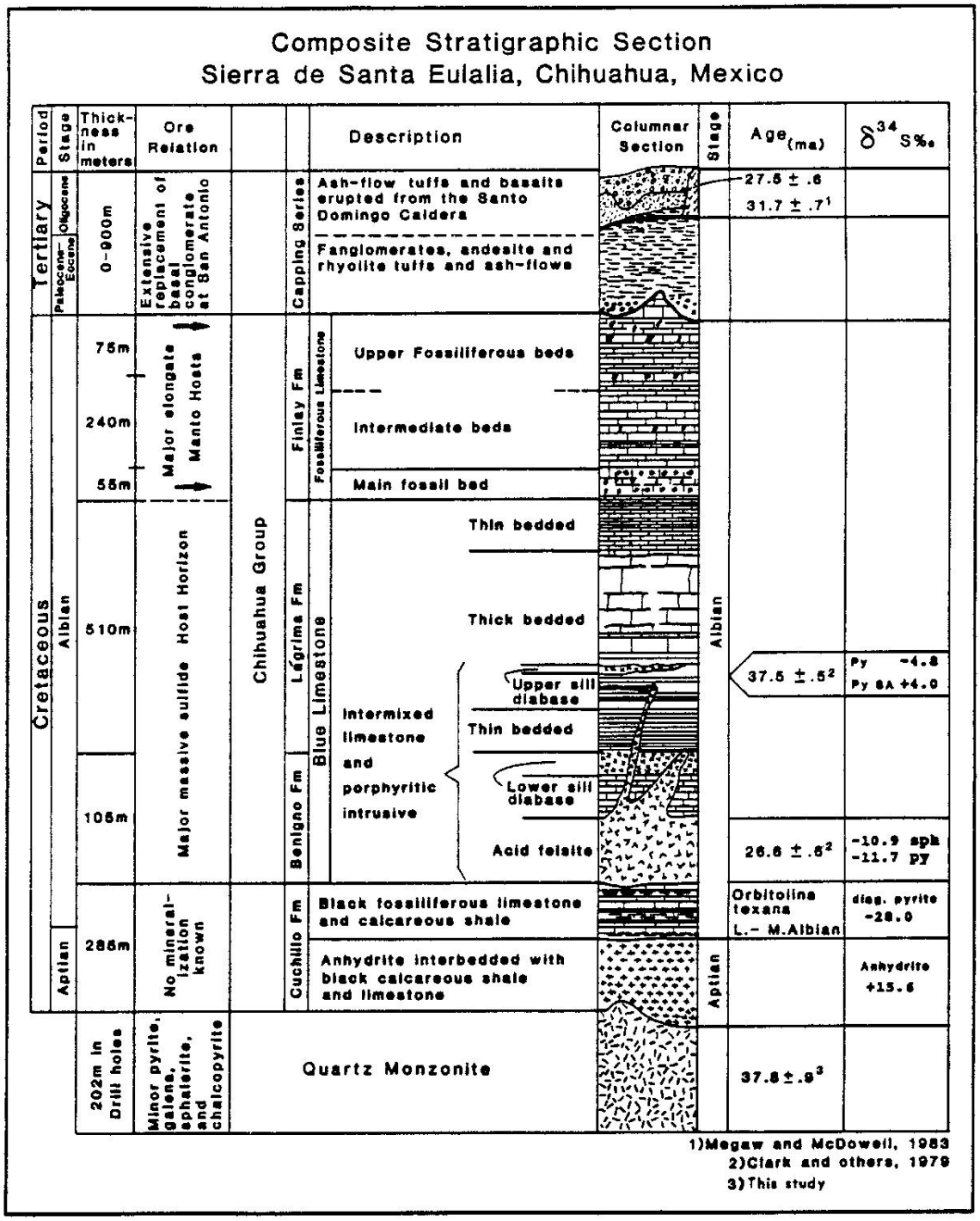

Figure 1-2: Stratigraphic column for the Sierra Santa Eulalia, Chihuahua, Mexico with K/Ar dates and sulfur isotopes (Megaw, 1990).

1.1.1 Igneous Intrusions

There are eleven igneous intrusions identified in the Santa Eulalia District (Megaw, 1986b; Megaw, 1990), but only the deep quartz monzonite, diabase sills, felsites, and lamprophyres (Figure 1-2) were considered in this study.

The quartz monzonite in the district is known to be "greenish, medium-grained, equigranular holocrystalline intrusive rock composed of plagioclase, k-feldspar, augite, hornblende, and magnetite with rare quartz" (Hewitt, 1968; Megaw, 1986b; Megaw, 1990).

The diabase sills "have been identified as dolerite, diabase, diabasic dolerite, doleritic diabase, and sodic diorite by R. J. Coloby and F. F. Grout and as a quartz-bearing dolerite approaching a quartz monzonite by C. P. Berkey" (Hewitt, 1968). The sills are "greenish, fine to medium-grained, aphanitic to porphyritic basic intrusive rock composed of plagioclase laths, hornblende, and sparse olivine" (Megaw, 1986b; Megaw, 1990). Although the normative classification is nepheline monzonite, this rock has historically been called a diabase and that classification will be kept throughout this paper (Hewitt, 1968; Megaw, 1990).

Megaw (1990) noted that the felsite "contains sparse quartz, K-feldspar, and plagioclase phenocrysts in a very fine-grained to aphanitic matrix of quartz and feldspar". More specifically, Max P. Erickson identified samples as "quartz porphyries with 3mm phenocrysts of quartz, orthoclase, albite, and plagioclase" (Hewitt, 1968). This rock type can be found in the West Camp as dikes and sills and in the East Camp as the "core of the symmetrically zoned San Antonio skarns" (Hewitt, 1968).

The lamprophyres “consist of fine-grained plagioclase and hornblende in an aphanitic groundmass of plagioclase and mafics. They cut ore and all other intrusive rocks and are compositionally distinct” (Megaw, 1986b).

1.1.2 Ore bodies

The ore bodies of Santa Eulalia take on many forms including mantos, chimneys, replacement veins, and associated bedding replacement (Hewitt, 1968). The West Camp contains mantos and chimneys of massive sulfides, while the East Camp is mostly made of “symmetrically zoned, intrusion-cored skarns with associated massive sulfides” (Megaw, 1986b).

The localization of ore bodies at Santa Eulalia has been a topic of extensive study. Most studies have focused on structural ore controls. One proposed idea is an intersection of a vertical fissure containing ore fluids and a favorable limestone results in a manto, while two fissures intersecting results in a chimney (Spurr, 1911; Hewitt, 1968). This may be most evident in the southern block (Hewitt, 1968). Prescott (1916) noted the four main fissure trends of N-S, N10E, N10W, and N30W were important for silver-lead-zinc fluid movement. All other trends were noted as important for oxidizing fluids. Prescott (1916) also felt the northerly trending fractures were the important pre-mineral ore structures. Some believe certain ore bodies may be controlled by fractures, but not all ore bodies can be explained by this idea (Benham, 1928a). Another idea is ore bodies form in locations containing ore-bearing solutions where a favorable route to the surface is present (Walker and Walker, 1956; Hewitt, 1968).

1.1.3 Sulfide Mineralization

Sulfide mineralization is the most important ore mineralogy of the district comprising pyrrhotite, pyrite, sphalerite, and galena with local chalcopyrite and arsenopyrite and trace amounts of other sulfides (Megaw, 1990; Lueth et al., 2000). Other minerals reported in the district include discrete grains of native silver, acanthite (pseudomorphous after argentite), pyrargyrite, argentopyrite, and polybasite (Megaw, 1986c) as well as gold and fizelyite (Megaw, 1990).

Bond (1986) described the zoning in the East Camp as "silicate-rich to sulfide-rich mineral assemblage as one passes upwards in the San Antonio graben and outwards from the San Antonio dike." Arsenopyrite, pyrrhotite, and chalcopyrite were observed to increase with depth, while galena decreases with depth (Bond, 1986). He also noted the increase of black, manganiferous calcite veinlets and pink limestone from the eighth level upwards (Bond, 1986). Minerals in the East Camp also exhibit geochemical zonation. At the San Antonio mine, lead and antimony concentrations in ores increase toward the surface, whereas arsenic, bismuth, silver, and selenium increase with depth (Lueth et al., 2000). Lueth et al. (2000) noted silver values of galena in skarn ore are higher than silver values in manto samples. Zoning is also revealed by metal ratios, with ratios determined by Bond (1986) and Walter (1985) showing increases in Ag/Pb, and Cu/Ag and decreases in Ag/Zn, Pb/Zn, Pb/Cu, Pb/Bi, and Sb/Bi with depth (Lueth et al., 2000).

The West Camp exhibits a large-scale metal zonation, but no obvious zonation is noted within individual ore bodies (Megaw, 1990), also noted by Prescott (1916). Lueth et al. (2000) noted ores in the northern West Camp are higher in Ag, Fe, and Si and poorer in As, Pb, Zn compared to the southern ore bodies. They also noted galenas from

chimney deposits tend to have higher concentrations of silver and antimony than the mantos, although samples from deep mantos are similar to chimneys, and silver and antimony values are consistently higher near the Condesa fracture than in samples from the Central West Camp. Similar to the metal zonation, the metal ratios in the West camp are relatively consistent within individual ore bodies (Aguirre, 1987), but they vary slightly on a larger scale (Lueth et al., 2000). Silicate ore bodies usually have higher Ag/Sb and Ag/Pb ratios than chimneys and breccias (Megaw, 1990; Lueth et al., 2000).

While there is an over-all trend of N/NW for the ore bodies of the Santa Eulalia District, there is a NE trend for the deep sulfide mantos in the southern block and for those ore bodies in the lower fossiliferous bed, as well as, a W/SW trend for the northern end of the district (Hewitt, 1968).

1.1.4 Fluid Inclusions

Megaw (1990) has extensively analyzed fluid inclusions for the Santa Eulalia District. He found that skarn and sulfide-hosted fluorite from the East Camp show primary inclusion homogenization temperatures from 150 to 450 °C, with the majority between 175 to 350 °C. The salinities for the East Camp are as high as 26.3 equivalent wt% NaCl for primary inclusions, with some samples indicating salinities as low as 2 to 8 and 7 to 10 equivalent wt% NaCl (Megaw, 1990). Secondary inclusions for the East Camp have homogenization temperatures of 80 to 200 °C, with apparent salinities of between 0.5 and 3.5 equivalent wt% NaCl (Megaw, 1990).

Megaw (1990) also studied fluid inclusions for the West Camp and found that primary fluid inclusions show a homogenization temperature range of 175 to 400 °C,

with the majority falling between 200 and 375 °C. Maximum salinities of 26.3 equivalent wt% NaCl were found for the West Camp with some samples indicating salinities as low as 2 to 11 equivalent wt% NaCl (Megaw, 1990). The secondary inclusions for the West Camp indicate temperatures with between 180 to 275 °C and salinities between 0.5 and 4 equivalent wt% NaCl (Megaw, 1990).

Lueth et al. (2000) found temperatures between 268 °C and 477 °C based on temperature calculations for sulfur isotope equilibrium pairs of sphalerite and galena. These temperatures are mostly consistent with but a little higher than the temperatures of homogenization of fluid inclusions for both camps. Lueth et al. (2000) compared variations in Ag and Sb concentrations in galena to experimental data of Amcoff (1976) and found a maximum solid solution of 5 atomic percent would correspond to crystallization temperatures below 217 °C. They also found Ag-Sb substitution to be strongest in the deepest portions of the West camp and suggest it may reflect temperature control near inferred fluid sources. Other previous workers found that ore minerals did not begin to precipitate until the felsites dikes and sills breached the diabase sills; this may coincide with a thermal boundary (Hewitt, 1968; Megaw, 1990; Lueth et al., 2000). Although, there is a suggestion of a temperature gradient across the district, Megaw (1990) noted there is insufficient distribution of fluid inclusion data points to document such a feature.

1.1.5 Stable Isotope Geochemistry

Many units in the Santa Eulalia District have been studied for their isotopic values. The unaltered Finlay Limestone gives values of -0.8 ‰ and 21.8 ‰ for $\delta^{13}C$ and

$\delta^{18}O$, respectively (Megaw, 1990). The $\delta^{13}C$ value is within the normal range and $\delta^{18}O$ value is considered lower than the accepted value for the Cretaceous limestone (Veizer and Hoefs, 1976; Megaw, 1990). Megaw (1990) also studied the sulfur isotopes at Santa Eulalia and noted that anhydrite from the Cuchillo Formation and cubic pyrite from the black, organic-rich, shaly upper portion of the Cuchillo Formation have very different $\delta^{34}S$ values of +15.6 ‰ and -28 ‰, respectively. Both of these values are considered normal for the specific types of units (Ohmoto and Rye, 1979; Claypool et al., 1980; Megaw, 1990). The sulfur isotopes of galena in the district which are in isotopic equilibrium with sphalerite also have a large range of values from -16.18 to +4.2 ‰ (Megaw, 1990).

Megaw (1990) noted the East Camp experienced an erratic and polyphase history of mineralization, typical of telescoped mineralization, resulting in no consistent isotopic pattern. This part of the district has a wide range and higher sulfur isotopic values over short distances attributed to the superimposed mineralization with higher concentrations of dissolved sulfur species compared to the West camp where the isotope range is similar (although more negative) and spread out over greater distances (Ohmoto, 1972; Megaw, 1990).

The West Camp exhibits a crude zoning pattern with elevation and distance from the deep southern chimney deposits (Megaw, 1990). The variation in sulfur isotope compositions is over 15 ‰ ranging from -15.83 to -0.87 ‰ $\delta^{34}S$ (Lueth et al., 2000). Miranda (1986) noted normal sulfides with values between -7 and -11 ‰ $\delta^{34}S$ (CDT), while values averaging -13.4 ‰ are typical of mineralization in the Condesa Breccia, the Condesa Chimney, and the Inglaterra Silicate Body. The most negative values found near

the southern chimneys, such as the Condesa fracture, also exhibit the highest Ag and Sb values, and the least negative values in the upper and northern portions of the camp, such as the Central West camp, exhibit low to moderate Ag and Sb values in galena (Lueth et al., 2000). Miranda (1986) also noted other areas of the Condesa Fissure exhibit sulfur values similar to the normal West Camp values and suggests the sulfides in the Condesa zone were emplaced during different pulses of mineralization. The range in sulfur isotopes values and zoning is attributed to a combination of varying initial $\delta^{34}S$ values and Rayleigh distillation (Megaw, 1990).

There is no direct correlation between sulfur isotopes and fluid inclusion temperatures, salinity, ore type, ore metal ratios, or iron sulfide species in either camp (Megaw, 1990). According to Lueth et al. (2000), the sulfur isotope zonation, galena Ag-Sb substitution, and galena Ag/Sb ratios may reflect distance from inferred fluid sources resulting from temperature gradients which were influenced by changing sulfur/metal ratios and resulted in isotopic disequilibrium between sulfide species (Ohmoto, 1972; Megaw, 1990).

1.1.6 Source of Sulfide Ore Fluids

Megaw (1990) interpreted the felsite intrusions to be the source of fluids for the sulfide mineralization due to the close temporal and spatial association between mineralization and brecciation and the felsites. It was noted that a series of distinctive felsite intrusions were emplaced before, during, and after mineralization. Ore body emplacement and variable geochemical conditions are indicated by fluid inclusion, mineralographic, and felsite cross-cutting relationships. This suggests minerals were

deposited from separate fluid packets with different initial $\delta^{34}S$ values that overlapped in time and space (Megaw, 1990).

1.1.7 K/Ar Geochronology

Some units in the Santa Eulalia area have previously been dated using the K/Ar method (Figure 1-2). These units gave ages of 31.7 Ma for a sanidine in a high potassium calc-alkalic rhyolite (Megaw and McDowell, 1983), 37.8 Ma for plagioclase phenocrysts in a quartz monzonite (Megaw, 1990), 37.5 Ma for plagioclase from two diabase sill end members in the West Camp (Clark et al., 1979), 26.6 Ma for feldspar from two felsites in the West Camp (Clark et al., 1979), and 32.2 ± 0.4 Ma for a hornblende from the Potosi Dike lamprophyre (Megaw, 1990). The lamprophyres crosscut felsites, diabase sills, and the intrusive breccias, indicating that the lamprophyres should be younger (Figure 1-3). In addition, the lamprophyres are mineralized or altered where they contact ore bodies. This presents a discrepancy due to the K/Ar dates indicating that the felsite, which is thought to be the mineralization source in the district, is younger than the cross-cutting and mineralized lamprophyres (Megaw, 1990).

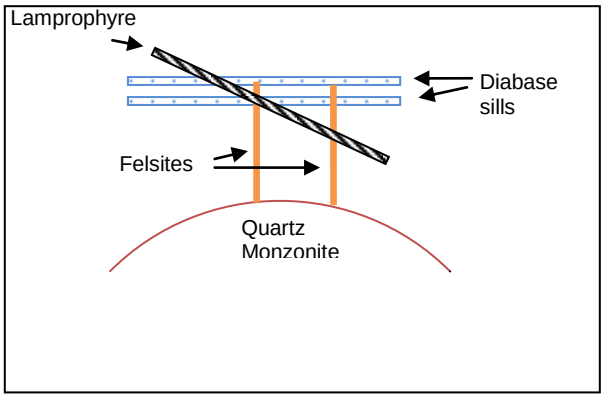

Figure 1-3: Schematic drawing of the cross-cutting relationships between the felsites and diabase sills and the lamprophyres.

1.1.8 AMOM of Santa Eulalia

The main mineralization at Santa Eulalia is the sulfide mineralization, but another less studied type of mineralization found within the district is the argentiferous manganese oxide mineralization (AMOM). This type of mineralization is found in both the East and West camps and is hosted in limestone and the volcanic capping rocks (Megaw, 1990).

Spurr (1911) has extensively described mineral zoning in the district and noted that AMOM is located within 9 to 15 m of major ore bodies and contains 35 to 1500 ppm of silver with silver content decreasing with distance from the ore bodies. He found that silver decreases and manganese increases with depth, but the manganese disappears at greater depths (Spurr, 1911). Hewitt (1968) noted the presence of lead-zinc-iron ores with modest silver ranging from 250 to 400 g in the southern normal sulfides and “irony” ore with minor lead content and rich in silver with content as high as 1 kg in the northern oxide bodies.

AMOM can be found in several locations throughout the district. The Finlay Limestone hosts most of the best developed limestone-hosted AMOM with it located adjacent to, above, and/or below oxidized normal sulfide mantos and chimneys, silicate bodies, and skarns that lie within 400 m of the surface (Spurr, 1911; Megaw, 1986a, 1987; Megaw, 1990). Well developed AMOM is also found in the East Camp along the West Fault of the San Antonio Graben and along both faults of the Dinamita Graben in the area between the Dinamita and Josefina Shafts (Megaw, 1990). Minor amounts of AMOM have been found in the San Antonio Mine adjacent to unoxidized ores hosted by the Lagrima Formation and oxide ores in the basal limestone Capping Series

Conglomerate (Bond, 1987; Megaw, 1990). The AMOM is hosted in volcanic rocks in both the West and East Camps. AMOM in the West Camp preferentially affects the Capping Series members that lie below the lowermost fined-grained andesitic tuff bed and in the East Camp it is most pervasive on the hill immediately south of the San Antonio Shaft (Megaw, 1990). According to X-ray diffraction analyses performed by Megaw (1990), the main manganese minerals hosted in limestone are pyrolusite, coronadite, and hollandite, but the volcanic-hosted manganese minerals are hollandite, ramsdellite, coronadite, pyrolusite, todorokite, hetaerolite, groutite, and nsutite. Manganese and silver minerals are not always found together and it has been noted that while silver decreases with depth, the manganese minerals increase (Spurr, 1911; Megaw, 1990). Megaw (1990) noted that although grades vary, assays of veinlet fillings exceeding 25 ppm silver and 0.5 % lead are common, and Spurr (1911) noted AMOM containing 35 to 1500 ppm silver occurs within 9-15 m of major ore bodies with the silver content decreasing progressively away from ore bodies. Elements in limestone-hosted AMOM were qualitatively analyzed by argon-plasma spectrophotometry (Megaw, 1987) and quantitatively by atomic absorption and neutron activation analysis (Bond, 1987; Megaw, 1990). Anomalous levels of Ag, Pb, Zn, Cu, Cd, Mn, Fe, and Ba were identified (Megaw, 1990). The East Camp AMOM has high levels of V, Cd, Co, Ni, Bi, which are also found in higher concentrations in East Camp ores than in West Camp ores (Burnham, 1959; Bond, 1987).

The origin of AMOM in the district is controversial. Some considered the AMOM to be hypogene and a valuable exploration tool (Kimball, 1870; Dahlgren, 1883; Rice, 1908; Prescott, 1910; Megaw, 1990), but Spurr (1911) thought the AMOM was formed

due to ore body oxidation and was unrelated to primary minerals dispersion. After Spurr made his conclusions about the AMOM, some workers did continue to map AMOM in detail (Benham, 1928b, 1929; Clendenin, 1933). The AMOM at Santa Eulalia has been found in some strata occupied by sulfide mineralization (Megaw, 1990). Megaw (1987) found the anomalous levels of Ag, Pb, Zn, Cu, Cd, Mn, Fe, and Ba drop to background levels after crossing out of the AMOM. Megaw (1990) thought that the presence of Santa Eulalia AMOM above ore bodies, the presence of sulfides within the AMOM, the anomalous metal content, and its occurrence in the sulfide zone of the San Antonio Mine, strongly indicate it is a hypogene product and related to the sulfide mineralization.

Santa Eulalia and Luis Lopez are examples of districts with complex manganese-oxide mineral deposits. A potential model for hypogene AMOM was presented for the Luis Lopez Manganese District, south of Socorro, New Mexico (Lueth et al., 2004). They proposed this district formed under similar conditions as Santa Eulalia. Figure 1-4 is a conceptual model for Luis Lopez (Lueth et al., 2004). Features, including the locations of the quartz monzonite, felsites, sulfide mineralization, and AMOM, of Santa Eulalia have been placed on the diagram. The felsites at Santa Eulalia do not reach the surface as they do in the Luis Lopez district, and instead of playa sediments, Santa Eulalia has volcanic capping rocks. If this model is used for Santa Eulalia, the felsites represent the source of the sulfide mineralization. As the hot fluids move away from the primary location of the felsites in the hydrothermal system, the fluids cool and deposit the AMOM distal to the sulfide mineralization.

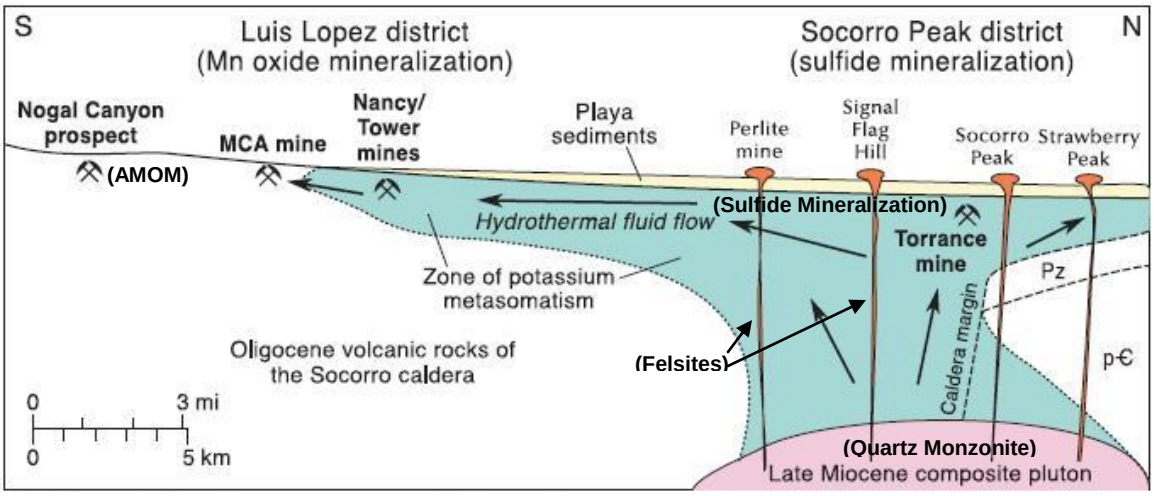

Figure 1-4: Conceptual model for the hydrothermal formation of the Luis Lopez Manganese District, New Mexico. Comments in parentheses (AMOM, Sulfide Mineralization, Felsites, and Quartz Monzonite) pertain to the Santa Eulalia District, Mexico. Modified from Lueth et al. (2004).

Although many think the AMOM is hypogene, Megaw (1990) suggests there may be supergene manganese oxide mineralization present in the district. It has been noted that hydrothermal and supergene manganese minerals may be hard to differentiate because minerals precipitated from a manganese-bearing hydrothermal solution that becomes increasingly oxidized under shallow level, low temperature conditions, may be the same as manganese oxide minerals formed in a supergene environment (Crerar et al., 1980; Megaw, 1990). Megaw (1990) suggests the presence of groutite and todorokite may indicate local supergene overprints on the hypogene AMOM.

1.2 Dating of Manganese Oxides

Manganese minerals are less commonly dated by K/Ar and $^{40}Ar/^{39}Ar$ methods than other minerals. No manganese oxides were previously dated in the Santa Eulalia area. Many studies, mostly focused on hypogene processes, have shown that coronadite

group manganese oxide minerals can be dated using the K/Ar method (Yahvili and Gukasyan, 1974; Varentsov and Golovin, 1987; Pracejus, 1989; Segev et al., 1991; Vasconcelos et al., 1992; Lippolt and Hautmann, 1995; Vasconcelos, 1999). Vasconcelos (1992, 1994) found that supergene coronadite group manganese oxides produce reliable dates using K/Ar and $^{40}Ar/^{39}Ar$ dating methods.

Manganese oxide minerals are commonly fine-grained and may be subject to recoil. If crystal domains are less than 5 microns the ^{39}Ar recoil may influence the step-heating spectra (Huneke and Smith, 1976). Although manganese oxides are usually subject to recoil, some studies have found the recoil loss is relatively small and does not prevent successful dating (Vasconcelos et al., 1994a; Vasconcelos et al., 1995; Ruffet et al., 1996; Vasconcelos, 1999). A more recent study by Lueth et al. (2004) utilized hydrothermal manganese oxide minerals in the Luis Lopez district, New Mexico. In this study, they found loss of ^{39}Ar related to recoil to be minimal and found the age determinations to agree with field observations.

Some minerals that may be best suited for K/Ar and $^{40}Ar/^{39}Ar$ dating include hollandite, cryptomelane, coronadite, romanechite, todorokite, vernadite, and birnessite (Vasconcelos, 1999). The crystal structures for these minerals are tunnels for hollandite, cryptomelane, coronadite, romanechite, and todorokite (Figure 1-5) and layered for vernadite and birnessite (Vasconcelos, 1999). The coronadite mineral group, including hollandite, cryptomelane, coronadite, and manjiroite, is well suited for K-Ar and $^{40}Ar/^{39}Ar$ dating because they may contain potassium and other cations in well-defined crystallographic sites, but the Ar retentivity may vary due to degree of crystallinity, grain size, and variations in the ionic radius and amount of vacancies in the tunnel sites

(Vasconcelos, 1999). Manganese oxide minerals may hold many different elements in their crystal structure, and it has been noted that Ba+2, K+, Pb+, and other large cations

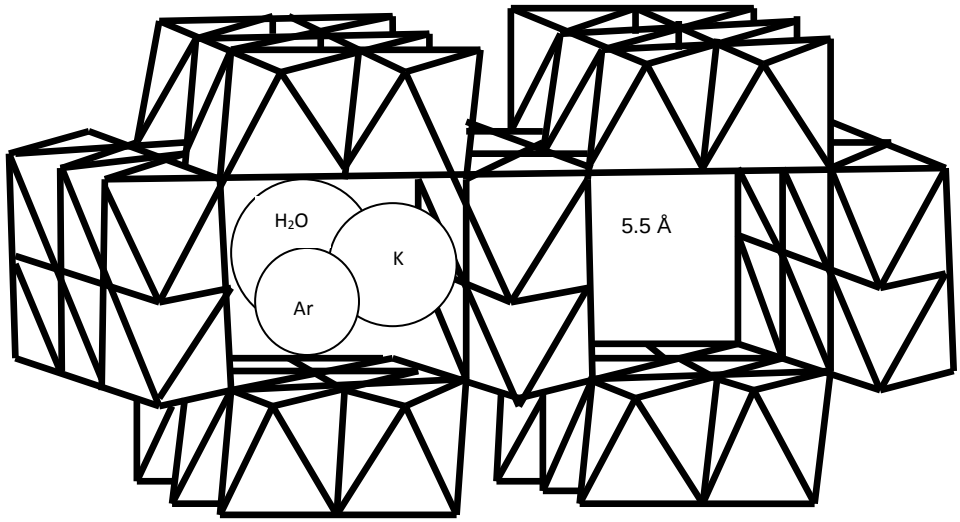

Figure 1-5: Coronadite Group crystal structure. The elements in the tunnel site indicate this is the mineral cryptomelane.

occupying the A site give stability to the coronadite group structure (Burns and Burns, 1979; Miura, 1986; Tsuji et al., 1993). If smaller cations occupy the A sites in the crystallographic structure, the mineral may be more susceptible to cation exchange (Burns and Burns, 1979) and thermal transformations (Vasconcelos et al., 1994b).

The first and most common coronadite group mineral dated by K/Ar or $^{40}Ar/^{39}Ar$ is cryptomelane (Chukhrov et al., 1966; Vasconcelos, 1992). Cryptomelane is well suited for dating due to the high potassium content (up to 5.5 wt%) and the high K and $^{40}Ar^{*}$ retentivity in the tunnel sites (Vasconcelos et al., 1995). The cryptomelane mineral has a crystallographic structure of a 2 x 2 tunnel (Figure 1-5). Vasconcelos (1999) compared cryptomelane using three different methods including TEM to look at the thermal behavior (Vasconcelos et al., 1994b), Ar analyses in a temperature-controlled resistance

furnace (RF) (Vasconcelos et al., 1995), and thermogravimetric analyses for the same samples. He found the collapse of the tunnel structure and not volume diffusion of the elements within the tunnel sites is responsible for the release of K and Ar from the tunnel sites.

Another mineral that may be appropriate for dating is todorokite. Todorokite is a complex 3 x 3 tunnel structure (Post and Bish, 1988). Vasconcelos (1999) noted water molecules in the todorokite crystal structure may be found in both well-defined crystallographic sites and as a disordered water component. Todorokite can hold up to 10-12 wt% water in the crystallographic structure (Bish and Post, 1989), which is released when heating from 200 to 500 °C, resulting in significant weight loss (Vasconcelos, 1999). Although manganese oxides have a tunnel structure, they are not capable of the same amount of cation exchange as zeolites, because the manganese oxide tunnels are not linked infinitely in the tunnel direction (Bish and Post, 1989). A study performed by Vasconcelos (1999), analyzed a todorokite sample crushed to different sieve sizes and analyzed at two different labs. Although the samples have similar potassium values, they show different results. One interpretation is that todorokite may not retain Ar quantitatively in the tunnel sites and Ar loss may result from crushing or the bake-out process performed before analyses (Vasconcelos, 1999). There is still much work needed to determine the appropriateness of using todorokite for these dating methods.

Birnessite is another mineral that is a potential candidate for either K/Ar or $^{40}Ar/^{39}Ar$ dating. It has been shown by electron diffraction patterns and Rietveld refinement to have a layered structure with ordered interlayer water molecules and

cations (Post, 1990). The Na-birnessite structure has been shown to collapse from 7 to 5 Å in the vacuum of an electron microscope (Post, 1990). This is possibly due to the loss of interlayer water creating an unstable structure that may prevent successful analyses of birnessite dated by K/Ar and $^{40}Ar/^{39}Ar$ (Vasconcelos, 1999). More work will need to be performed to determine the suitability of birnessite for these dating methods.

1.3 Luis Lopez Manganese District

The Luis Lopez Manganese District is located southwest of Socorro, NM (Figure 1-6) within the eastern part of the Socorro caldera (Eggleston et al., 1983). It contains several manganese deposits including the MCA, Tower, Nancy, Black Canyon, and Gloriana mines, as well as other areas.

Figure 1-6: Location of the Luis Lopez Manganese District in New Mexico.

Temperatures of homogenization determined by Norman et al. (1983) indicate a dynamic system repeatedly changing between hydrostatic and lithostatic pressures. This

may be explained by open fractures with hydrostatic pressure, which are then filled by precipitated minerals resulting in lithostatic pressure, and then new fractures forming with hydrostatic pressure (Norman et al., 1983). This process may explain the banded mineralization seen in the district.

In a previous study by Eggleston et al. (1983), samples from different mines in the Luis Lopez district were analyzed for oxygen and carbon isotopic compositions. This data revealed an area of $\delta^{18}O$ enrichment over the "red alteration zone," thought to be formed from hydrothermal processes (Eggleston et al., 1983). Although Eggleston et al. (1983) proposed the idea of rhyolitic volcanism near Socorro Peak as the source of heat to drive the hydrothermal system, Lueth et al. (2004) goes even further by proposing the heat source is an upper crustal composite granitic pluton associated with the Socorro Peak rhyolite lava domes. The $\delta^{13}C$ values of -2.5 and -0.5 ‰ (PDB) are similar to other epithermal vein deposits (Ohmoto and Rye, 1979; Eggleston et al., 1983), and Eggleston et al. (1983) suggest the Luis Lopez manganese deposits formed from a circulating hydrothermal system dominated by meteoric water. In this hypothesis, they thought $\delta^{18}O$ rich waters leached manganese from the Hells Mesa Tuff, which was then precipitated to formed the manganese deposits, which are dated between 6.33 and 6.71 Ma (Lueth et al., 2004). Lueth et al. (2004) noted an unaltered rhyolite dike and a compositionally and texturally equivalent rhyolite plug, dated at 11.05 ± 0.05 Ma and 10.99 ± 0.06 Ma, respectively, in the Hells Mesa Tuff. Both cut the "red alteration zone" while the rhyolite plug is cut by manganese veins (Lueth et al., 2004). Due to the incompatibility of the model proposed by Eggleston et al. (1983) with the field relationships and the age dates,

the overall theory of the processes is plausible, but the source of the manganese proposed by Eggleston et al. (1983) seems less likely.

Lueth et al. (2004) proposed a model for the formation of the Luis Lopez deposits (Figure 1-4). This model indicates a hydrothermal system formed from hot fluids circulating and moving progressively to the south. As the hydrothermal fluids moved away from the rhyolite intrusions in the caldera and cooled, they precipitated the manganese oxide minerals along faults and fractures. The Luis Lopez District is thought to be similar to the Santa Eulalia District (Megaw, 1990; Lueth et al., 2004), and the general genetic model for the Luis Lopez Manganese District (Figure 1-4) may be used to represent similar processes at Santa Eulalia.

1.4 Objectives of Current Study

There are four main objectives for this study: 1) Identify the manganese oxide minerals in each sample; 2) Evaluate oxygen and carbon isotopes for information concerning the source of fluid, evolution of fluid, etc.; 3) Re-date the intrusive rocks using the $^{40}Ar/^{39}Ar$ method to resolve previous inconsistencies in the K/Ar dating of Megaw (1990); 4) Date manganese oxides from the AMOM and compare to the ages of the intrusive rocks, especially the felsite intrusions, to determine if sulfide and AMOM are contemporaneous.

2. METHODS

The data for Santa Eulalia was collected from samples sent by P.K.M. Megaw and P.C. Goodell (UTEP). The four manganese oxide samples from Santa Eulalia are from the West Camp, hosted in limestone, and include SE-PKM, collected by P.K.M. Megaw, and SE-PGE, SE-PGD, and SE-bulk, collected by P.C. Goodell. The four intrusive rocks from Santa Eulalia include Core 1, Felsite Core, Cp1813 2070', and Cp1813 92', collected by P.K.M. Megaw. The data for Luis Lopez and Water Canyon was measured from samples collected by V. Lueth and samples personally collected during this study.

2.1 Mineralogical Identification

Three methods were employed for the mineral identification. These include petrographic microscope work, electron microprobe analyses, and X-ray diffraction analyses. The petrographic work was only used to identify mineral grains used for the $^{40}Ar/^{39}Ar$ dating process while preparing mineral separates of the intrusive and manganese oxide rocks at New Mexico Institute of Mining and Technology.

2.1.1 Electron Microprobe Analyses

Microprobe quantitative point analyses were made to identify the types and relative amounts of certain elements in the samples, including K, Mn, Zn, Pb, Ba, Na,

Ag, Fe, Si, and Ca. This data helped provide guidance for what part of the sample may exhibit relatively higher amounts of K and may prove more useful for $^{40}Ar/^{39}Ar$ dating of the manganese oxides. The relative amounts of the elements may also indicate the presence of certain manganese oxide minerals, which can then be confirmed during the X-ray diffraction analyses.

Electron Microprobe analyses were performed at New Mexico Institute of Mining and Technology on the Cameca SX-100 microprobe. Quantitative point analyses were performed on seven thin sections made from four Santa Eulalia rock samples, SE-PKM, SE-PGE, SE-PGD, and SE-bulk. The beam current was 20 nA producing a spot size of approximately 1 mm. The counting times were 40 seconds for Na and Ba, 10 sec for Zn and Ag, and 20 sec for Mg, Si, K, Ca, Mn, Fe, S, and Pb. All microprobe data can be found in Appendix B.

2.1.2 X-ray Diffraction Analyses

X-ray diffraction (XRD) analyses were performed to identify the type of manganese oxide and other minerals present in each sample. This helped to understand which separates contain fewer unnecessary minerals such as quartz, calcite, or goethite, as well as, to understand the behavior of the samples during the $^{40}Ar/^{39}Ar$ dating process.

XRD analyses were obtained for manganese oxide and matrix separates of four carbonate rock samples, SE-PKM, SE-PGE, SE-PGD, and SE-bulk, and mineral separates of four intrusive rocks, Core 1, Felsite Core, Cp1813 2070', and Cp1813 92'. The XRD separates were prepared by taking the separate made for $^{40}Ar/^{39}Ar$ analyses and crushing to powder. The powder was place on an XRD sample holder, making sure to

keep it below the top of the holder, and placed in the Panalytical X'pert Pro XRD machine at New Mexico Institute of Mining and Technology. The samples were run from a 2θ position of 6.0084 to 69.9794 with a step size of 0.0170. The scan step time was 10.1600 seconds for short scans and 152.4000 seconds for longer runs. All analyses were run with a continuous scan, a scanning PSD mode, a 2θ PSD length of 2.12, a 2θ offset of 0.0000, Cu as the anode material, and in spinning mode. The machine was set to 40 mA and 45 kV. The manganese oxide samples prepared for $^{40}Ar/^{39}Ar$ analyses were analyzed with XRD to determine if they were appropriate for dating analyses, where as the intrusive separates were analyzed to help interpret the $^{40}Ar/^{39}Ar$ step heating analyses. All XRD data can be found in Appendix C.

2.2 Stable Isotope Geochemistry

Rock samples were prepared and carbon and oxygen stable isotope data was collected to determine the origin of fluids responsible for AMOM mineralization in the Santa Eulalia District. Previous $\delta^{18}O$ and $\delta^{13}C$ data for the Luis Lopez areas of the MCA Mine, Tower Mine, and Gloriana Mine from a previous class project at New Mexico Institute of Mining and Technology collected under the supervision of A. Campbell and new isotopic data from the Luis Lopez areas of the MCA Mine, Nogal Canyon, Pretty Girl Mine, Black Canyon Mine, and Nancy Mine along with data from the Water Canyon, (Magdalena area) were compared to new data from Santa Eulalia to see if the mineralization of the two districts is similar.

Carbon and oxygen isotope data were collected for four Santa Eulalia samples, fifteen Luis Lopez samples, and six Water Canyon samples. The samples were prepared

by crushing and weighing out ~0.25 mg of the material, including ~0.25 mg for the $CaCO_3$ standards and ~0.50 mg for the $BaCO_3$ standard, and placing in a round bottom vial. The vial is capped with a green cap containing a gray septum. A blank with no sample was placed at the beginning of the run, then the standards, and after the standards every eighth vial contained a duplicate separate of the lab standard Mexican Calcite. After all the vials were prepared with the separates, they were flushed with He for ~3 minutes. After the He flush, ~10 drops of phosphoric acid were added to each vial, excluding the blank which contained no sample. The vials sat in the heating block at 45 °C for four hours before the run was started. The samples were run on the Finnigan Delta XP Plus Isotope Ratio Mass Spectrometer with a PAL autosampler and Gas Bench II continuous flow gas delivery system. All stable isotope data can be found in Appendix D.

2.3 $^{40}Ar/^{39}Ar$ Geochronology Sample Preparation and Analyses

2.3.1 Intrusive Rocks Sample Preparation

This study involved dating intrusive rock samples to better understand the timing of magmatism in the area. Previous dates were determined using the K/Ar method. This study uses the $^{40}Ar/^{39}Ar$ method, which gives dates that are more precise and can account for argon loss or non-atmospheric argon. In addition, this study attempts to resolve an incompatibility between the K/Ar dates of the lamprophyre and the K/Ar dates of the diabase sills and felsites, relative to cross-cutting relationships.

The four intrusive rock samples, Core 1 (lower diabase sill), Felsic Core (felsite), Cp1813 2070’ (quartz monzonite), and Cp1813 92’ (upper diabase sill), were crushed and sieved to a size of approximately 250 to 400 μm to minimize composite grains. The sieve

fraction was then rinsed in distilled H_2O to clean the grains and remove any excess rock dust. After identifying the desired mineral grains, they were hand-picked to make sample separates for each rock sample. After analyzing the intrusive separates with the $^{40}Ar/^{39}Ar$ dating method, XRD was used to identify the minerals of similar separates.

2.3.2 Manganese Oxides Sample Preparation

Samples of manganese oxide were dated using the $^{40}Ar/^{39}Ar$ dating method to establish the time of mineralization of these minerals. Comparison of this data with the intrusive rocks helped to assess whether the felsites caused the manganese mineralization.

The carbonate-hosted rocks, SE-PKM, SE-PGE, SE-PGD, and SE-bulk, exhibit different textures of manganese oxide mineralization (Appendix A). Figure 2-1 shows vein and dendritic mineralization in sample SE-PKM, one of the three manganese rocks dated. Each texture was individually separated. In order to make each separate, each rock was broken into chunks representing each mineralization style and placed into separate glass beakers. Undiluted HCl was added to each beaker to dissolve the $CaCO_3$. The separates were then rinsed in H_2O and dried in the oven. Once dried, unwanted minerals such as quartz, micas, and iron oxides were picked out of the separates. Once the separates were considered clean, they were analyzed by X-ray diffraction to select which mineral separates were best suited for the $^{40}Ar/^{39}Ar$ dating process.

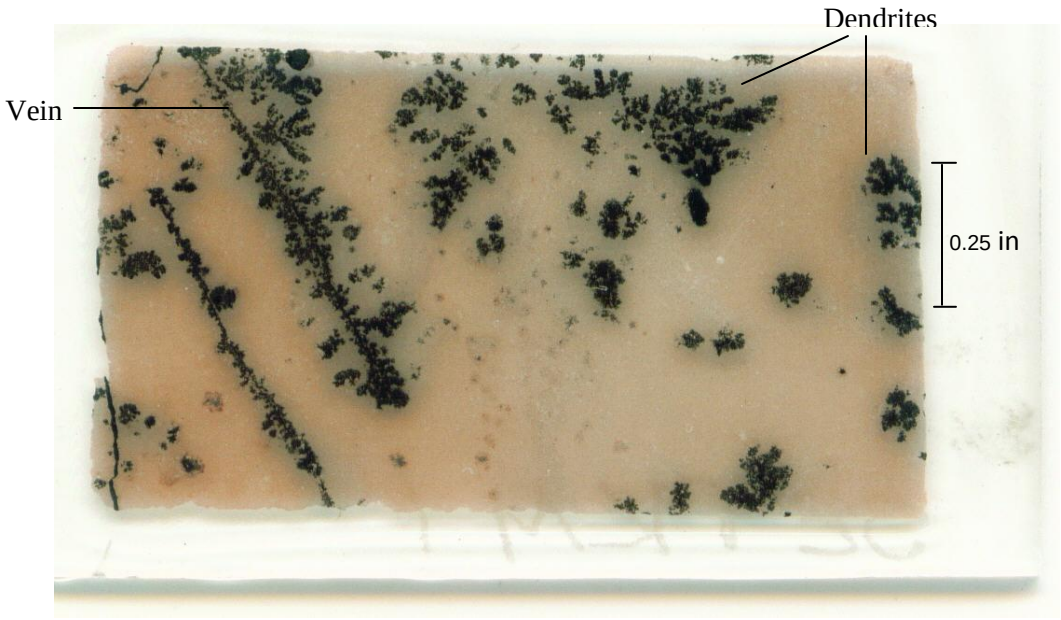

Figure 2-1: Photograph of the SE-PKM-1 thin section used for microprobe analyses. Relationship of veins and dendrites is shown.

2.3.3 Irradiation Procedures

The intrusive rock mineral separates were placed in 20-hole irradiation trays and irradiated for approximately 10 hours, and the manganese oxide mineral separates were placed in 6-hole irradiation trays and irradiated for approximately 7 hours. Both irradiation batches were irradiated along with 28.02 Ma (Renne et al., 1998) neutron fluence monitor Fish Canyon sanidine in the USGS TRIGA reactor at the Denver Federal Center, Colorado. Once the samples returned from the reactor, they were loaded into laser trays for analyses. The intrusive rock separates were placed in a 61-hole laser tray in a manner that resembled a checkered pattern, skipping holes that are next to other holes with separates in them, and the manganese oxide separates were loaded into a 10-hole laser tray.

2.3.4 Analytical Methods

Each separate was step-heated to produce an age-spectrum. The step-heating schedule depended on the type of separate. To determine the heating schedule for the K-feldspar, a similar K-feldspar was step-heated to see how much argon was released at certain temperatures. For the other intrusive rock minerals, we used heating schedules previously determined for the specific mineral. The step-heating schedules for the manganese oxide separates were determined by running a manganese oxide separate using a previously determined schedule used at NMGRL to see if it was appropriate for the manganese oxide samples.

The step-heating was performed by heating with the NMGRL CO_2 laser and analyzed in the MAP 215-50 at New Mexico Institute of Mining and Technology, Socorro, New Mexico. The intrusive rock samples were heated for 30 seconds at each specified temperature, and the manganese oxide samples were heated for 45 seconds at the specified temperatures. The clean up times for the intrusive rocks for the 1^{st} and 2^{nd} stages were 90 seconds each for all minerals except the biotite, where they were 120 seconds each. The manganese oxide sample clean up times for the 1^{st} and 2^{nd} stages were 540 seconds and 180 seconds, respectively. The CO_2 laser beam was defocused to about 4x4 mm for the intrusive rock samples and about 6x6 mm for the manganese oxide samples to heat the separates more evenly. The detectors used for the intrusive rocks include both the Multiplier and Faraday, with the Faraday detector only being used when the sample yielded large ^{37}Ar beams, and only the Multiplier was used for the manganese oxide samples. The data tables, J factors, watts for each heating step, and correction factors can be found in Appendix E.

3. RESULTS

3.1 Mineral Identification

Microprobe and X-ray diffraction analyses were performed for four rocks from Santa Eulalia to determine the mineralogy of the manganese oxides. All data for microprobe and XRD analyses are located in Appendix B and C, respectively.

3.1.1 Electron Microprobe Analyses

Two hundred and twenty-seven points have been quantitatively analyzed in four different rock samples (Appendix B) from Santa Eulalia. Fifty-three of the points have at least 59 %FeO. One of the 227 points has 85 %CaO. Of the points with at least 44 %MnO, 25 have at least 13 %PbO, 1 has at least 10 %ZnO, and 20 have at least 2 %K_2O (Figure 3-1). During microprobe analyses, the samples were determined to have manganese oxides intimately intergrown with other minerals, such as calcite (Figure 3-2).

Initially, the microprobe analyses were focused on evaluating the potential effectiveness of using the $^{40}Ar/^{39}Ar$ dating method for the manganese oxides. The manganese oxides must contain enough K_2O, to be useful in the $^{40}Ar/^{39}Ar$ dating method. Figure 3-1 shows %MnO ranging from 0 to about 95 % and %K_2O from 0 to almost 5 %. The four rocks have different ranges in K_2O, while the ranges of MnO for the samples are

similar. SEPKM and SEPGE have the largest range of $\%K_2O$ and SEPKM has the largest range of %MnO.

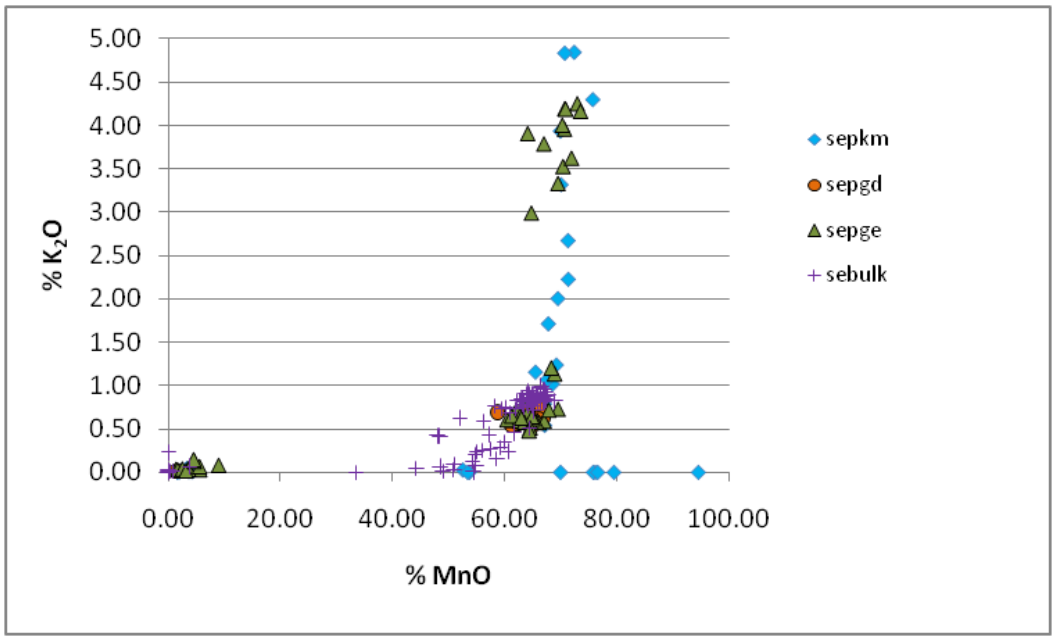

Figure 3-1: All microprobe analyses plotted with $\%K_2O$ versus %MnO.

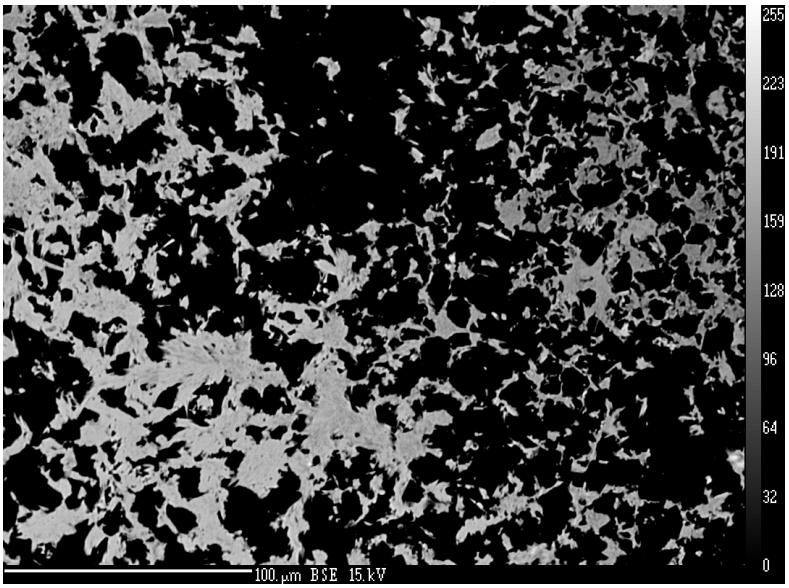

Figure 3-2: Relationship of manganese oxides (gray) and other minerals, such as calcite (black) in SE-PKM microprobe backscatter image. Elements with higher atomic weights are lighter in color than those with lower atomic weights.

Ternary diagrams were constructed to indicate which manganese minerals are present in those microprobe analyses that contain at least 44 %MnO. A minimum of 44 %MnO was chosen because this is the lowest %MnO value greater than those determined to be mixed phases and non-manganese phases. XRD analyses were used to confirm the interpretations from the microprobe analyses.

The ternary diagram in figure 3-3 shows the microprobe analyses containing at least 44 %MnO and normalized to the three components of K_2O+PbO+ZnO, CaO, and MgO. Only points with at least 44 %MnO were used in this figure to ensure high Fe, possibly goethite, and calcite data points were not reassigned as a manganese mineral, and all the points on the diagram have at least 2 % of one of the components to ensure trace elements are not included in the mineral identification. This diagram is mainly used to identify the birnessite and todorokite data points. There are two main groupings of points on this diagram that plot close to the CaO - MgO side of the diagram. These groups are interpreted to be birnessite and todorokite. Due to the similarity in the chemical formulas of birnessite and todorokite (Table 3-1) it is difficult to differentiate between the two minerals through chemical analyses. X-ray diffraction analyses were used to differentiate between the two minerals.

Figure 3-4 is a ternary diagram with the components of K_2O, PbO, and ZnO. The analyses on this diagram contain at least 44 %MnO, at least 2% of one of the components, and the points are normalized to the three components. This diagram is used to differentiate cryptomelane, coronadite, and chalcophanite in the electron microprobe data sets. Numerous analyses plot close to the K_2O corner along the K_2O - ZnO side of the diagram and contain less than 20 %PbO. These points are interpreted to be

cryptomelane because of high manganese (~65-75 %MnO, with most between 70 and 73 %MnO) and high potassium (~2-5 $\%K_2O$, with most between 3.5 and 4.3 $\%K_2O$). The points that plot close to PbO are interpreted to be coronadite because of high lead (~13-30 %PbO) and high manganese (~45-60 %MnO) content and low amounts of iron, calcium, potassium, sodium, and other elements, as indicated by electron microprobe analyses. There are two points that plots in the corner of ZnO. The one closest to the ZnO corner is interpreted to be chalcophanite because of the high zinc (~10 %ZnO) and high manganese (~60 %MnO) content, and the other point is todorokite or birnessite because of the high manganese (~65 %MnO), high calcium (~2 %CaO), high magnesium (~2 %MgO), and potassium of moderate level (~0.5 $\%K_2O$). There is one point that plots towards the center of the diagram and is interpreted to be birnessite or todorokite because of the moderate manganese (~59 %MnO), high calcium (~3.5 %CaO), high magnesium (~1.4 %MgO), and moderate potassium (~0.7 $\%K_2O$).

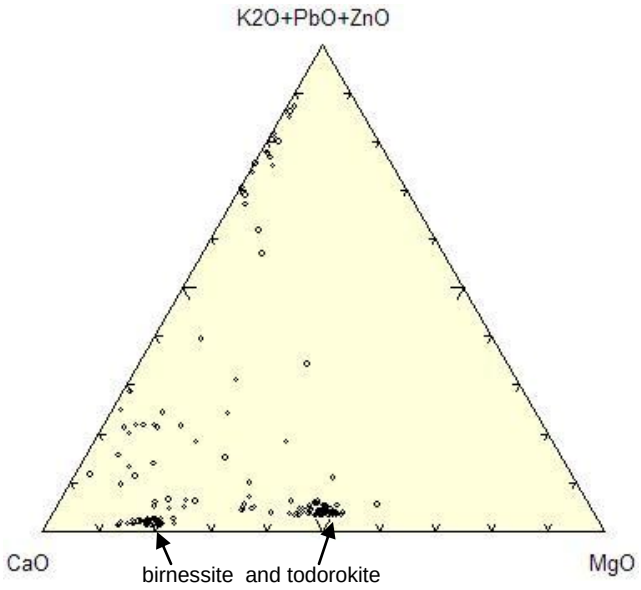

Figure 3-3: Microprobe data using data points with at least 44% MnO and at least 2% of one of the components, eliminating high Fe or Ca data points and trace elements. The data are normalized to the components of K_2O+PbO+ZnO, CaO, and MgO.

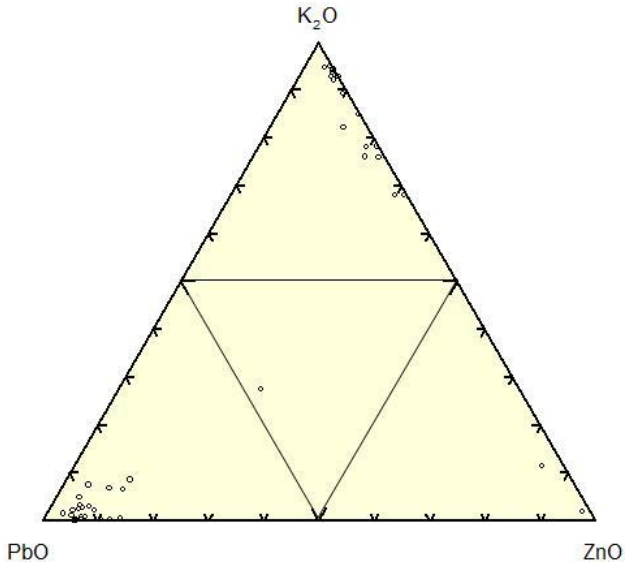

Figure 3-4: Microprobe data using points with at least 44% MnO and at least 2% of one of the components, eliminating high Fe, high Ca data points and analyses with K_2O, PbO, and ZnO less than 2%. The data are normalized to the components of K_2O, PbO, and ZnO.

Table 3-1: Manganese oxide minerals and formulas (Vasconcelos, 1999; Back and Mandarino, 2008).

Mineral	**Formula**	**Group**
Cryptomelane	$(K,Ba)_{1-2}Mn_8O_{16}.xH_2O$	Coronadite
Coronadite	$(Pb,Ba,K)_{1-2}Mn_8O_{16}.xH_2O$	Coronadite
Chalchophanite	$(Zn,Fe,Mn)Mn_3O_7.3H_2O$	Chalcophanite
Todorokite	$(Ca,Na,K)(Mg,Mn^{2+})Mn_5O_{12}.xH_2O$	Coronadite
Birnessite	$(Na,Ca,K)(Mg,Mn)Mn_6O_{14}.5H_2O$	Birnessite

3.1.2 X-ray Diffraction Analyses

Several separates were prepared for X-ray diffraction analyses from four rock samples containing manganese oxides hosted in carbonate from Santa Eulalia. These were analyzed to identify both minerals in the manganese oxides and in the carbonates of each rock. Table 3-2 summarizes the XRD results of the manganese oxide separates.

Separates similar to those run for $^{40}Ar/^{39}Ar$ analyses of the intrusive rocks were also prepared and run. All XRD scans are located in Appendix C.

Four separates from SE-PKM-1 were analyzed using XRD during preparation for $^{40}Ar/^{39}Ar$ analyses and are presented in figure 3-5. The presence of many similar peaks indicates the mineral separates share a similar mineralogy. Although the four separates have many peaks in common, there are a few peaks that only show up in a few of the scans. Cryptomelane and coronadite peaks are identified in all four separates, indicating the presence of the minerals in all the separates for SE-PKM-1. Talc was present for the veins, but absent for the dendrites. Goethite was found within the dendrites, but absent for the veins. Other minerals such as birnessite, quartz, and illite were also identified in some of the separates.

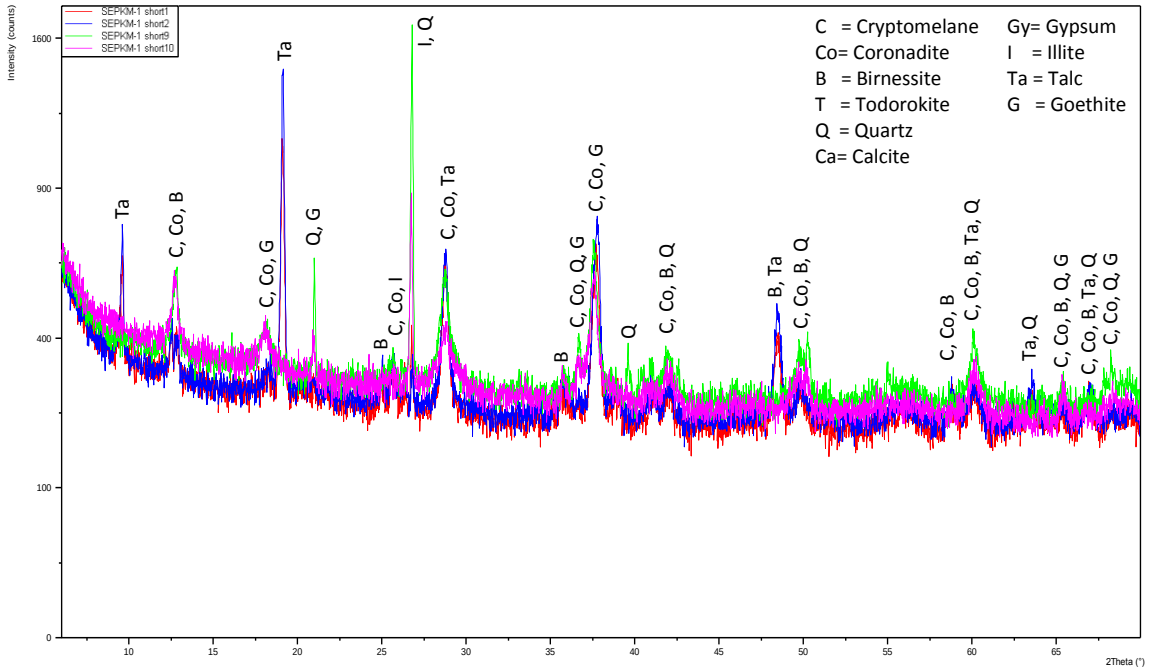

Figure 3-5: SE-PKM-1 scans of separates dated using the $^{40}Ar/^{39}Ar$ method. The red and blue are from veins and the green and magenta are from dendrites.

The separates from SE-bulk-1 and SE-PGE-1 were analyzed using XRD during preparation for $^{40}Ar/^{39}Ar$ analyses and are presented in figure 3-6. These two separates have many similar peaks for the mineral todorokite indicating the presence of the mineral in both separates. SE-bulk-1 has many peaks corresponding to calcite that do not show up in the SE-PGE-1 separate indicating the presence of more calcite in SE-bulk-1. The presence of more calcite in SE-bulk-1 may be due to the calcite being intimately intergrown with the manganese minerals (Figure 3-2).

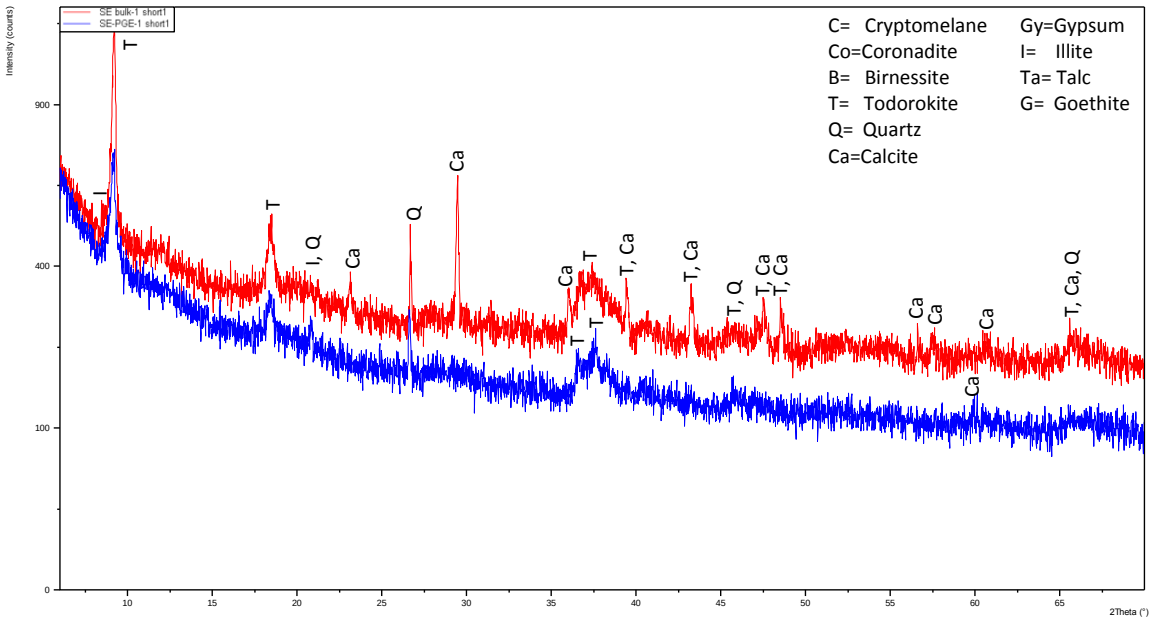

Figure 3-6: The two todorokite separates dated using the $^{40}Ar/^{39}Ar$ method. The red is SE-bulk-1 and the blue is SE-PGE-1.

Table 3-2: Minerals indentified in six manganese oxide separates. The scan colors for SE-PKM-1 correspond to colors in figure 3-5, and scan colors for SE-bulk-1 and SE-PGE-1 correspond to figure 3-6.

Sample	Scan Color	Mineral Morphology	Manganese Minerals	Other Minerals
SE-PKM-1	red	Vein	Birnessite, Coronadite, Cryptomelane	Talc, Other clays
	blue	Vein	Birnessite, Coronadite, Cryptomelane	Quartz, Illite, Talc, Other clays
	green	Dendrite	Coronadite, Cryptomelane	Goethite, Quartz
	magenta	Dendrite	Birnessite, Coronadite, Cryptomelane	Quartz
SE-bulk-1	red	Dendrite	Todorokite	Calcite, Quartz
SE-PGE-1	blue	Dendrite	Todorokite	Goethite, Quartz, Illite

3.1.3 Synthesis of Electron Microprobe and X-ray Diffraction

Figure 3-7 shows the processes followed to determine the minerals present in the AMOM samples. Using both the microprobe and XRD analyses, mineralogies were assigned to the quantitative microprobe data points and plotted in figure 3-8. The manganese minerals determined through microprobe analyses are cryptomelane (including low K cryptomelane), birnessite, todorokite, coronadite, and chalcophanite (Figure 3-8). Other minerals inferred by the microprobe data include calcite and a high Fe phase, possibly goethite. There are also a few mixed phase microprobe points, possibly resulting from the microprobe beam hitting more than one crystal therefore analyzing more than one mineral in the sample, designated as unknown (Figure 3-8). XRD analyses confirm many of the minerals inferred by the microprobe analyses including cryptomelane, birnessite, todorokite, coronadite, calcite, and goethite. XRD analyses also indicate the presence of quartz and clay minerals including talc and illite. No chalcophanite was found during the XRD analyses, but chalcophanite shares many of the same major XRD peaks as cryptomelane and coronadite and may have been overlooked. Birnessite and todorokite have similar quantitative analyses in the microprobe analyses and XRD analyses were used to differentiate between them in the microprobe analyses. Microprobe and XRD analyses of the AMOM samples did not detect any significant silver and no sulfosalts were found in the samples studied.

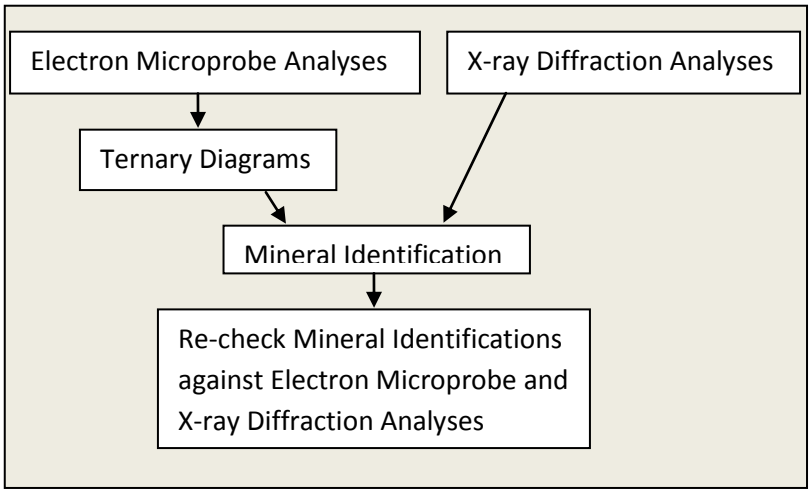

Figure 3-7: Flow chart of processes followed to identify the minerals in the AMOM.

Figure 3-8 shows some interesting relationships between different potassium and manganese values. There are two groupings of birnessite. One group contains between 1 and 1.75 $\%K_2O$ and MnO just below 70 %. The other group contains approximately 0 $\%K_2O$ and MnO around 75 to 80 %. This may be due to the substitution of different elements in the birnessite structure. Sodium, calcium, and potassium can substitute for one another in one structure site, while magnesium and manganese can substitute for each other in another structure site (Vasconcelos, 1999). Another interesting feature seen in this figure is that as the %MnO and $\%K_2O$ covary until the manganese reaches about 70 %. At about 70 %MnO, the potassium can range up to increase to almost 5 $\%K_2O$. Different manganese oxide minerals can be interpreted at specific areas along this curve. The major and trace elements of AMOM at Santa Eulalia are similar to other manganese deposits. Major and trace elements at the Luis Lopez district in New Mexico show manganese of about 40 to 50 %Mn, lead of about 0.45 to 5 %Pb, and zinc of about 0.04 to 0.60 %Zn (Norman et al., 1983).

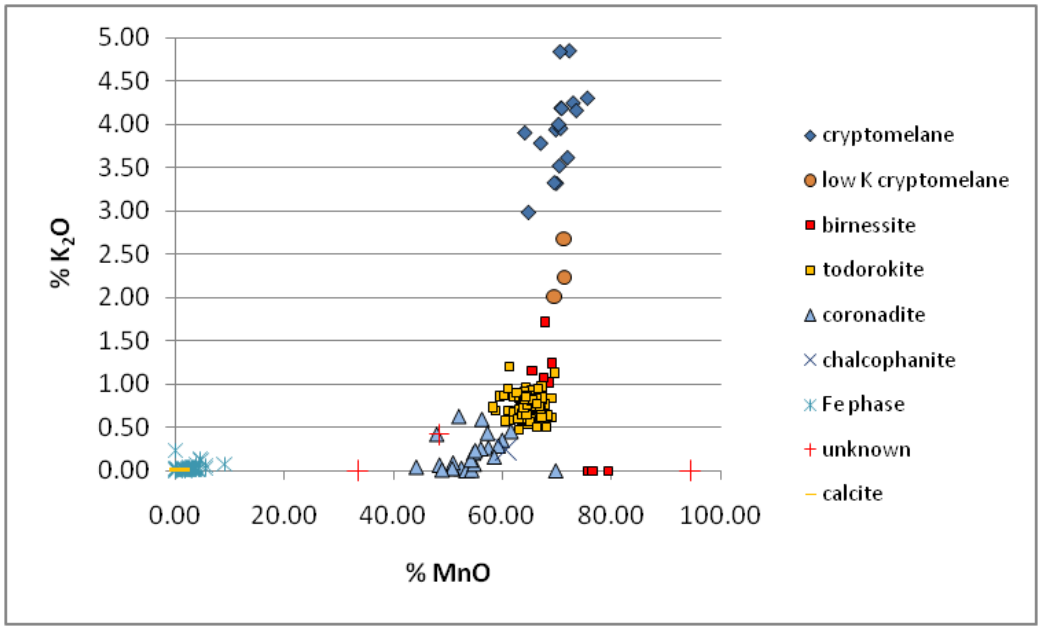

Figure 3-8: Microprobe data %K_2O vs. %MnO plotted by inferred mineral.

3.2 Stable Isotope Geochemistry

Carbon and oxygen isotopes were analyzed for limestones from the Santa Eulalia District, Mexico and calcites from the Luis Lopez Manganese District and Water Canyon areas, New Mexico. The reproducibility of $\delta^{13}C$ on duplicate samples ranges from 0.04 to 0.38 ‰, with an average of ± 0.12 ‰ and the reproducibilty of $\delta^{18}O$ on duplicate samples ranges from 0.13 to 0.40 ‰, with an average of ± 0.20 ‰. All stable isotope data for Santa Eulalia, Luis Lopez, and Water Canyon are located in Appendix D.

All data for Santa Eulalia, including limestone and calcite values determined by Megaw (1990) and during this study, are plotted in figure 3-9. The limestone values range from -7.6 to 3.0 ‰ $\delta^{13}C$ and 13.5 to 24.3 ‰ $\delta^{18}O$. $\delta^{13}C$ values of new Santa Eulalia limestone samples range from -7.6 to -2.2 ‰ and $\delta^{18}O$ values range from 16.6 to 23.6 ‰ (Figure 3-9), and three hydrothermal calcite separates have values of -10.1, -10.0, and -

1.6 ‰ $\delta^{13}C$ and 12.8, 12.7, and 15.4 ‰ $\delta^{18}O$, respectively. The background values of the Finlay Limestone near Santa Eulalia are approximately -0.8 ‰ and 21.8 ‰ for $\delta^{13}C$ and $\delta^{18}O$, respectively (Megaw, 1990). $\delta^{13}C$ and $\delta^{18}O$ data reported by Megaw (1990) were plotted against distance from ore veins in figures 3-10 and 3-11, respectively. Both $\delta^{13}C$ and $\delta^{18}O$ values become lighter nearer the vein.

Old and new $\delta^{13}C$ and $\delta^{18}O$ values of calcite for Luis Lopez are plotted in figure 3-12 along with new calcite data for Water Canyon. $\delta^{13}C$ values for Luis Lopez range from -7.7 to 1.2 ‰ and $\delta^{18}O$ values range from 11.6 to 24.5 ‰. $\delta^{13}C$ values for Water Canyon range from -0.6 to -4.3 ‰ and $\delta^{18}O$ values range from 15.3 to 19.7 ‰. The values in figure 3-12 show an inverse relationship between the $\delta^{13}C$ and $\delta^{18}O$ values.

The $\delta^{13}C_{HCO3-}$ and $\delta^{18}O_{H2O}$ were calculated for Luis Lopez from $\delta^{13}C$ and $\delta^{18}O$ values of calcite, using equation from Deines et al. (1974) and Kim and O'Neil (1997) and average temperatures determined by Norman et al. (1983), and are plotted in figure 3-13. This figure shows the range of $\delta^{13}C_{HCO3-}$ is from -6.5 to 2 ‰ and the range of $\delta^{18}O_{H2O}$ is from 10 to 25 ‰. Fluid values were not calculated for all calcite values, including Water Canyon, Nogal Canyon, and Pretty Girl, due to the lack of temperature information.

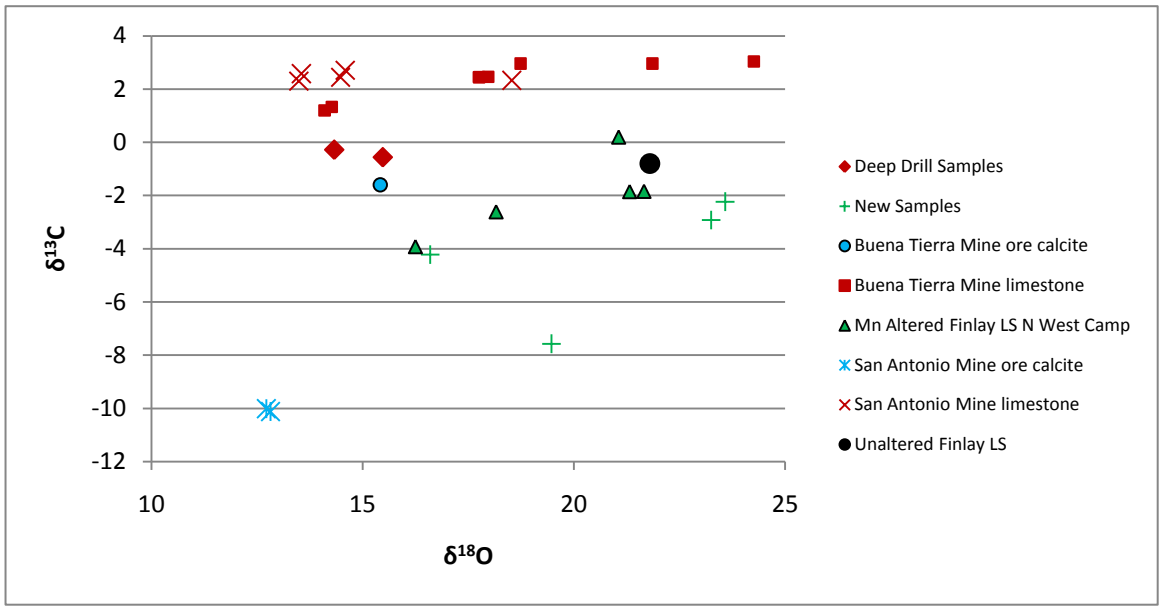

Figure 3-9: $\delta^{13}C$ vs. $\delta^{18}O$ values for calcite and limestone (Megaw, 1990) and new limestone samples (this study) for Santa Eulalia.

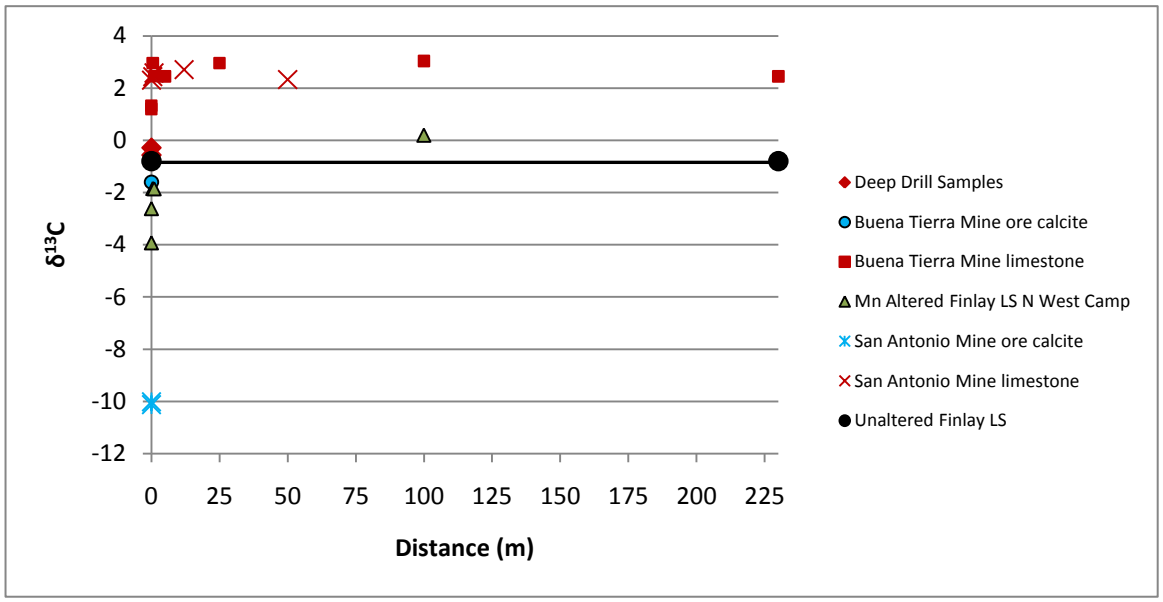

Figure 3-10: Santa Eulalia $\delta^{13}C$ plotted against distance from ore veins in meters (Megaw, 1990). Unaltered Finaly Limestone is considered background with $\delta^{13}C$ value of -0.8 ‰.

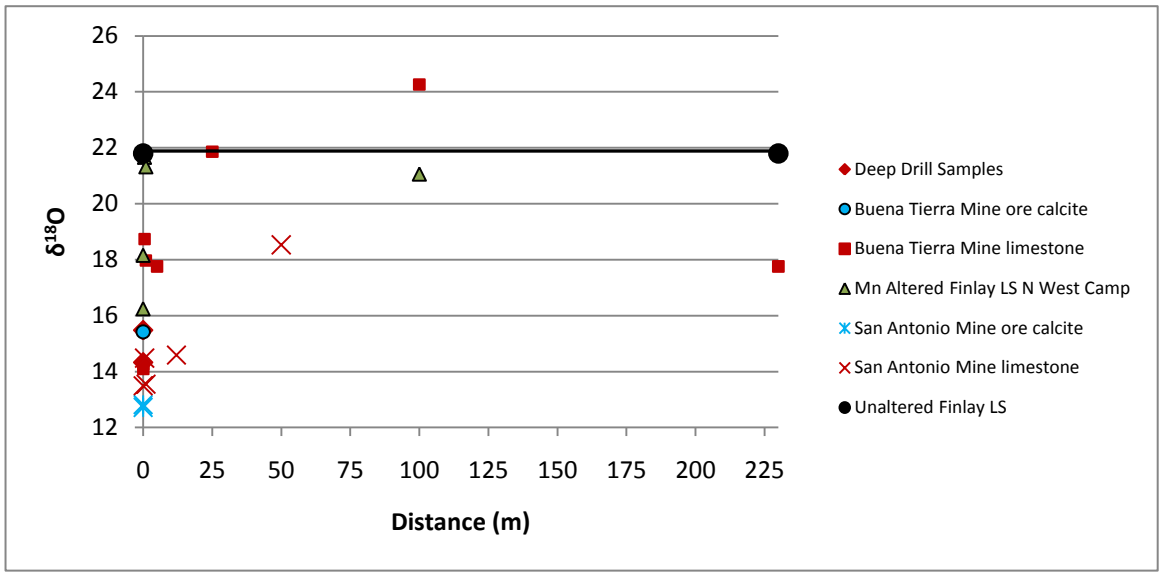

Figure 3-11: Santa Eulalia $\delta^{18}O$ plotted against distance from ore veins in meters (Megaw, 1990). Unaltered Finaly Limestone is considered background with $\delta^{18}O$ value of 21.8 ‰.

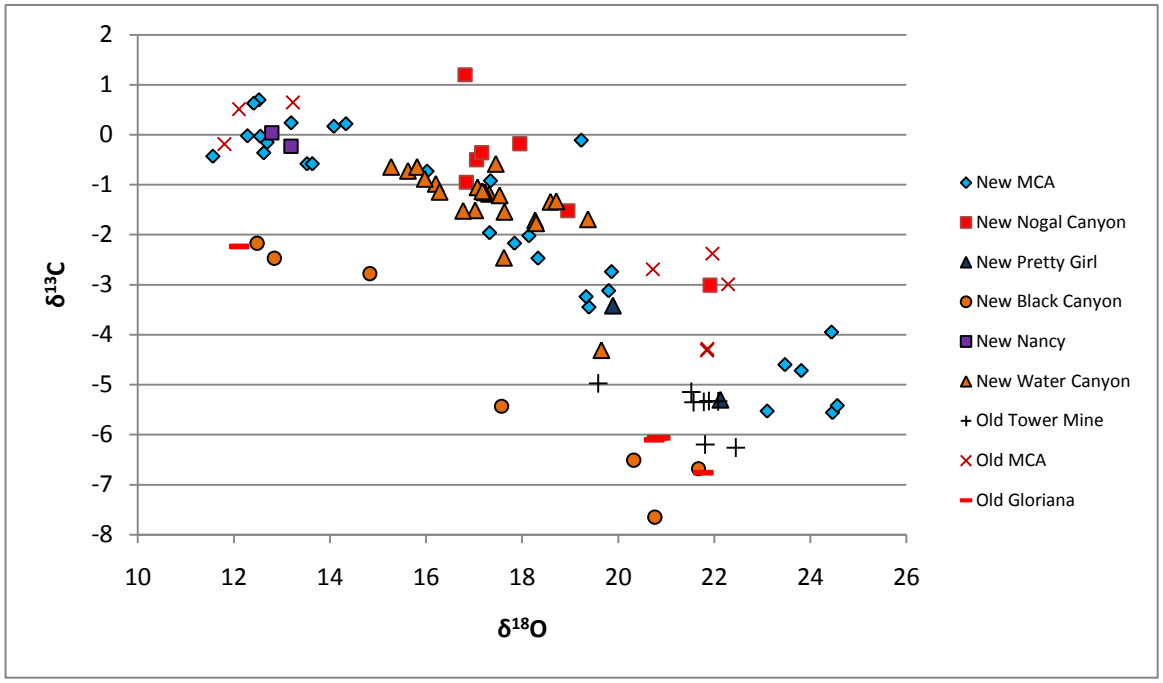

Figure 3-12: $\delta^{13}C$ and $\delta^{18}O$ values of calcite for Luis Lopez and Water Canyon, New Mexico.

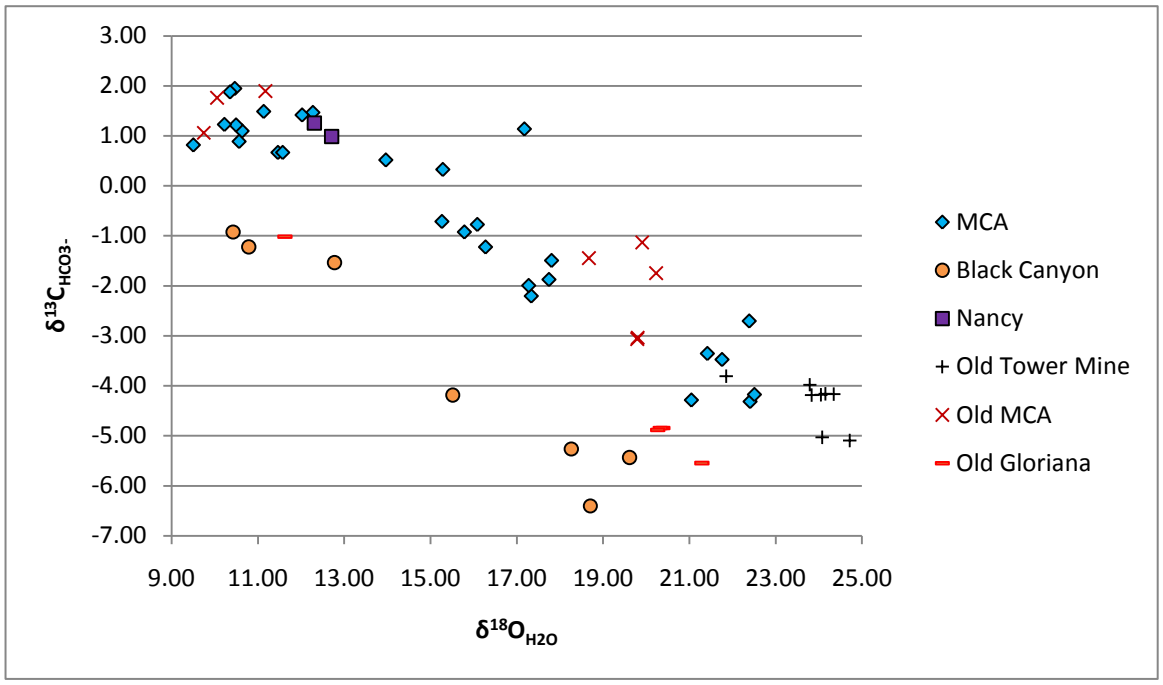

Figure 3-13: Luis Lopez data with $\delta^{13}C_{HCO3-}$ vs. $\delta^{18}O_{H2O}$. Equations from Deines et al. (1974) and Kim and O'Neil (1997) and temperatures determined by Norman et al. (1983) were used to calculate $\delta^{13}C_{HCO3-}$ and $\delta^{18}O_{H2O}$, respectively.

Rock samples at Luis Lopez and Water Canyon show variations in the carbon and oxygen isotopes between calcite bands. Figures 3-14 through 3-17 show the carbon and oxygen calcite values of individual rocks from different locations. Sequential carbonate bands were sampled. In some rock samples the order of calcite band formation may be inferred by textures and are labeled with numbers, with "1" being the first formed. The order of calcite band formation in other rocks is not as easily inferred and is labeled with letters to designate the relative timing even though it is not clear which end of the trend is first.

Most rock samples at the MCA mine (Figure 3-14) exhibit a strikingly linear trend in the carbon and oxygen isotope values. Some rock samples, such as MCA-1, MCA-2, and MCA-7 do not vary along this linear trend, but instead exhibit a small

variation around one end of the over-all trend. MCA-4 has one point that is different than the over-all linear trend of the rock, but this point is not too far from the over-all trend of the MCA mine.

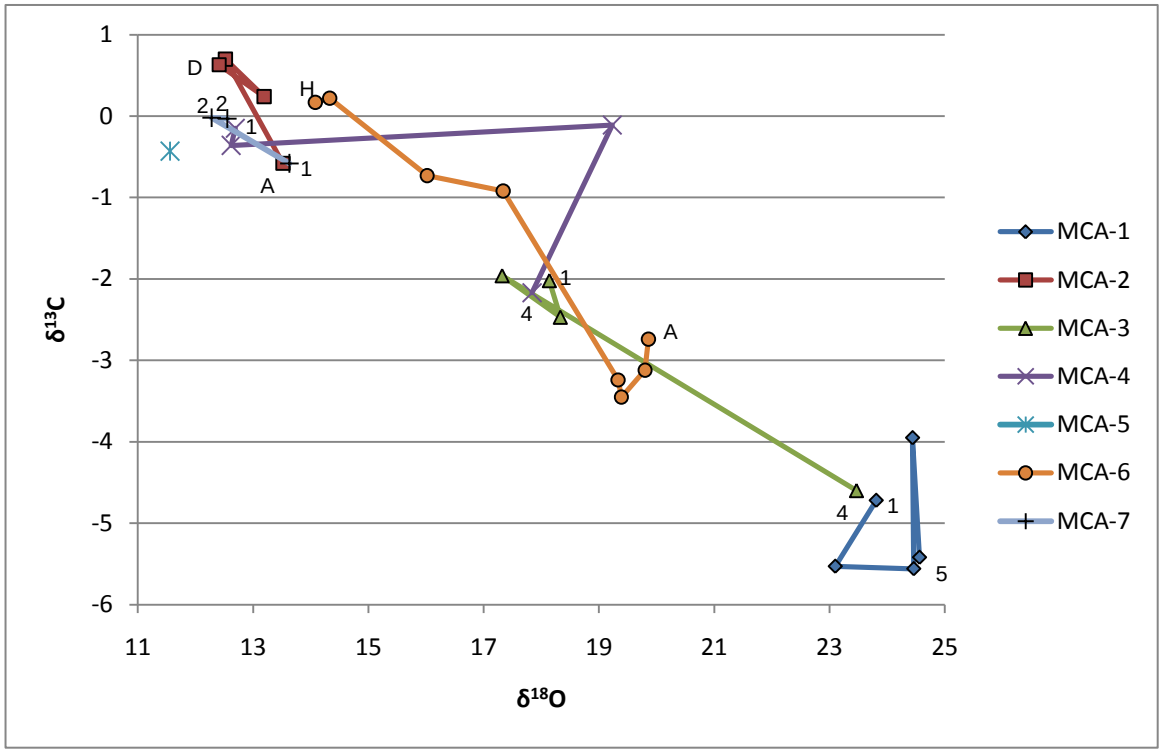

Figure 3-14: $\delta^{13}C$ vs. $\delta^{18}O$ of calcite of seven rocks at the MCA mine.

Figures 3-15 and 3-16 show the carbon and oxygen values of calcite of individual rock samples at Nogal Canyon and Black Canyon mine, respectively. The rock Nogal-2 shows a small variation in carbon and oxygen isotopes before moving along a linear trend with progressively heavier oxygen and lighter carbon values (Figure 3-15). The rock BC-2 shows a large variation in carbon and oxygen isotopes values that jump back and forth along a linear trend (Figure 3-16).

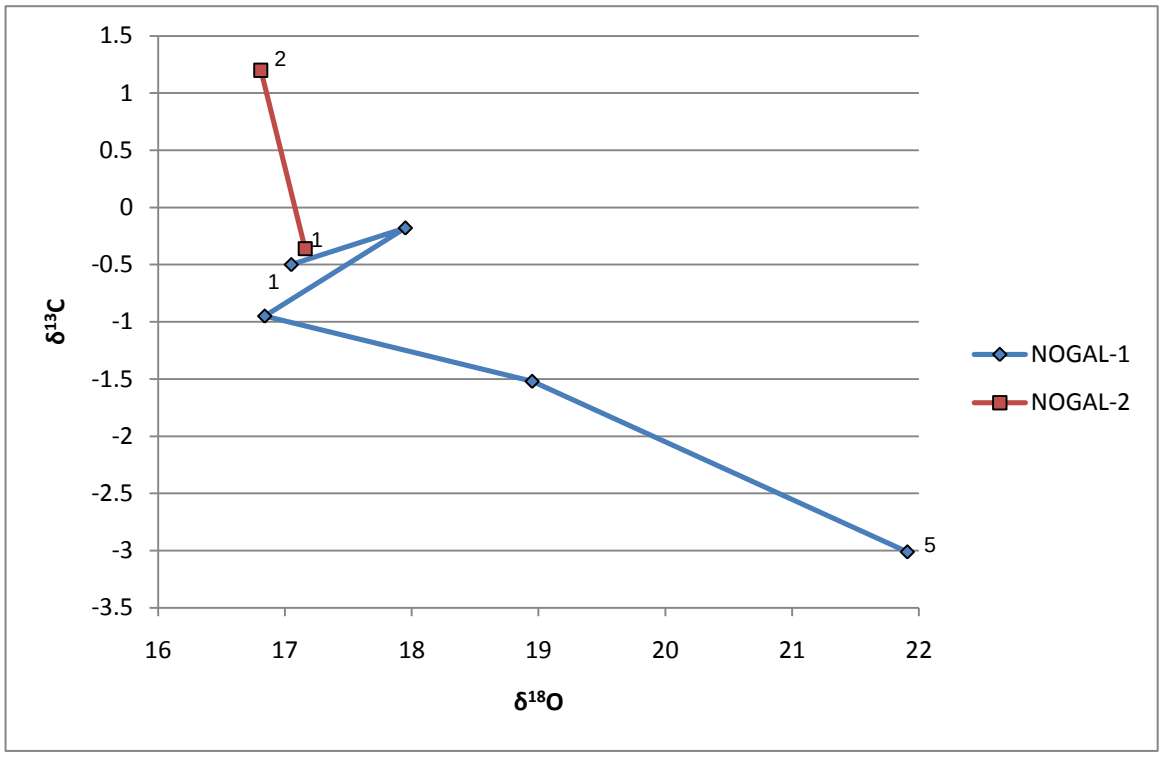

Figure 3-15: $\delta^{13}C$ vs. $\delta^{18}O$ of calcite from two rocks at Nogal Canyon.

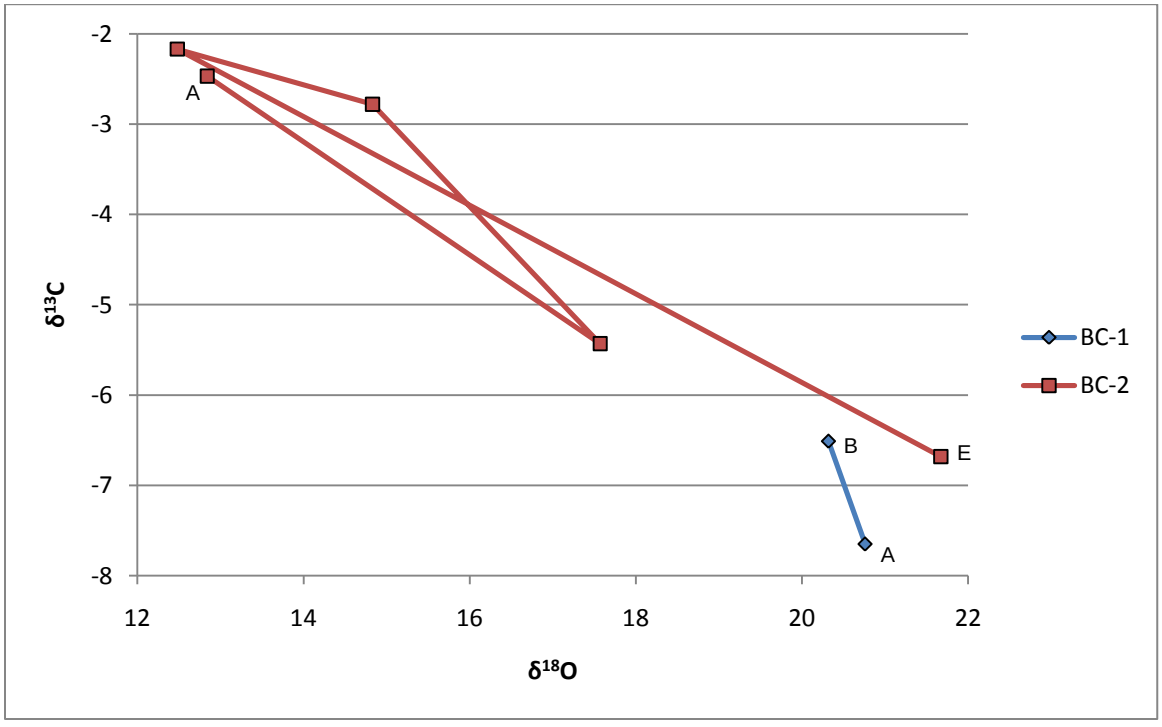

Figure 3-16: $\delta^{13}C$ vs. $\delta^{18}O$ of calcite of two rocks at the Black Canyon mine.

Figure 3-17 shows the carbon and oxygen values of calcite of individual rock samples at Water Canyon. This figure shows two major lines of variation where one is shifted from the other with a similar slope. There is great variability in the carbon and oxygen values among the different rock samples at Water Canyon. Some samples show a progression along the major linear trend (003304B and 003308), but other samples jump back and forth along the over-all trend (003301, 003304, and 003304A).

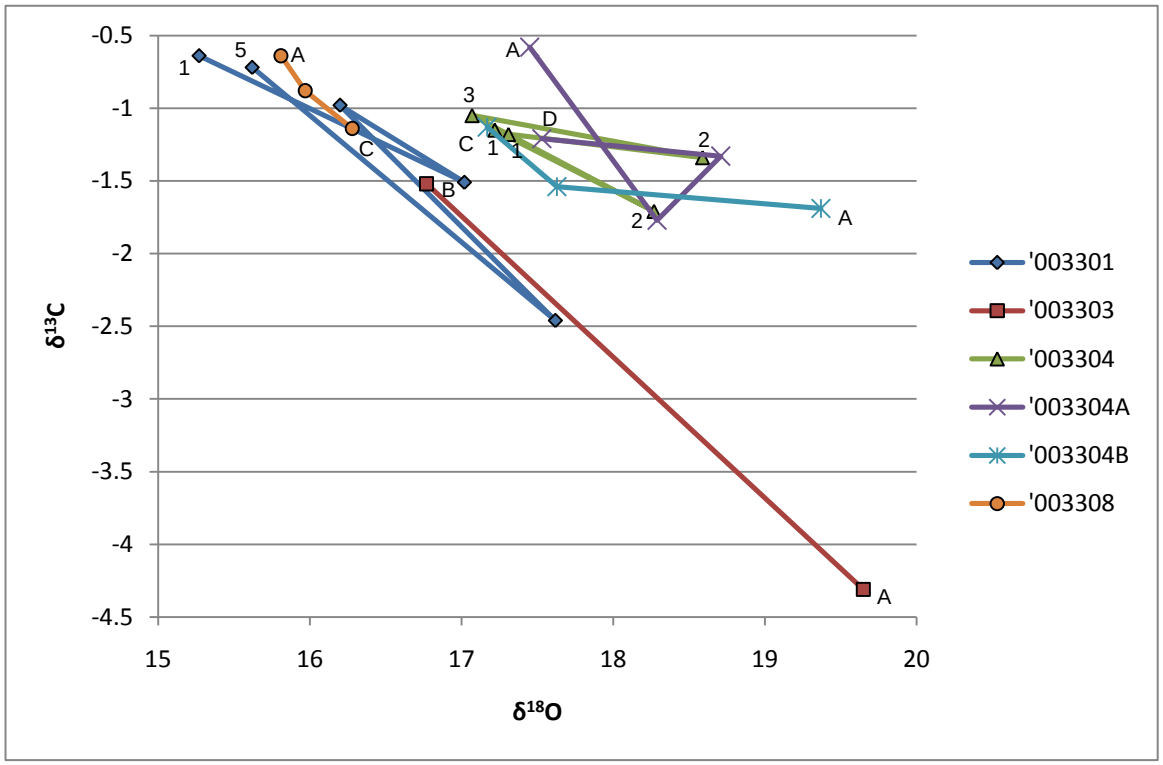

Figure 3-17: $\delta^{13}C$ vs. $\delta^{18}O$ of calcite of six rocks at Water Canyon.

3.3 $^{40}Ar/^{39}Ar$ Geochronology

As described above, intrusive rocks and manganese oxides from Santa Eulalia were analyzed using the $^{40}Ar/^{39}Ar$ dating method. All data tables, individual step-heating spectra, and isochrons are in Appendix E.

3.3.1 Intrusive Rocks

The four intrusive rock samples analyzed using the $^{40}Ar/^{39}Ar$ method in this study are from the Santa Eulalia drill hole Cp1813 (Figure 3-18). The samples include a felsite with unknown depth (Felsic Core), a quartz monzonite from 2070' (Cp1813 2070'), and two diabase sills with one from 92' (Cp1813 92'), known as the upper sill, and one from unknown depth (Core 1), known as the lower sill.

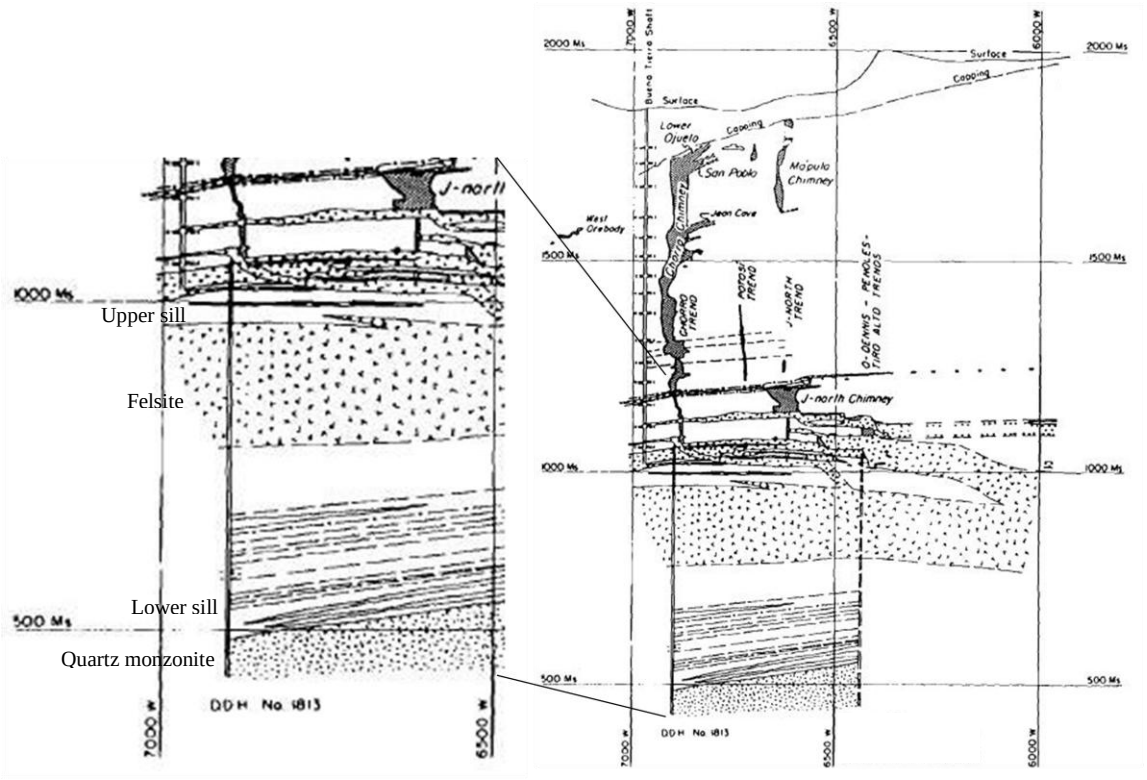

Figure 3-18: West-East cross-section of drill hole Cp1813, looking North. Approximate locations of the four rock units are shown. Modified from (Hewitt, 1968).

Plagioclase and groundmass step-heating results for Felsic Core are presented in figure 3-19. The age spectra for both separates are fairly flat. They also meet the plateau criteria with at least three contiguous steps with overlapping ages containing at least 50 % of the gas released. The plateaus contain approximately 70 % and 96 % of the gas for

groundmass and plagioclase, respectively. The individual steps for the groundmass separate are more precise than the steps for the plagioclase separate. The plagioclase plateau age is 34.3 ± 0.5 Ma. The groundmass plateau age is 33.06 ± 0.11 Ma. The plateau ages of the plagioclase and groundmass separates do not agree within 2σ error. The plagioclase separate has a lower $^{40}Ar^*$, reaching a maximum of about 40 %, than the groundmass separate, which reaches a maximum of about 90 %. The plagioclase Cl/K is higher, with an average around 0.003, than the groundmass Cl/K, which has an average around 0.00003. The plagioclase K/Ca averages around 0.1, compared to the groundmass K/Ca of about 4. The plagioclase and groundmass isochrons show $^{40}Ar/^{36}Ar$ intercepts similar to atmospheric argon (295.5) with isochron ages of 33.6 ± 1.3 Ma and 33.4 ± 0.6 Ma, respectively (Figures E-5 and E-6 in Appendix E).

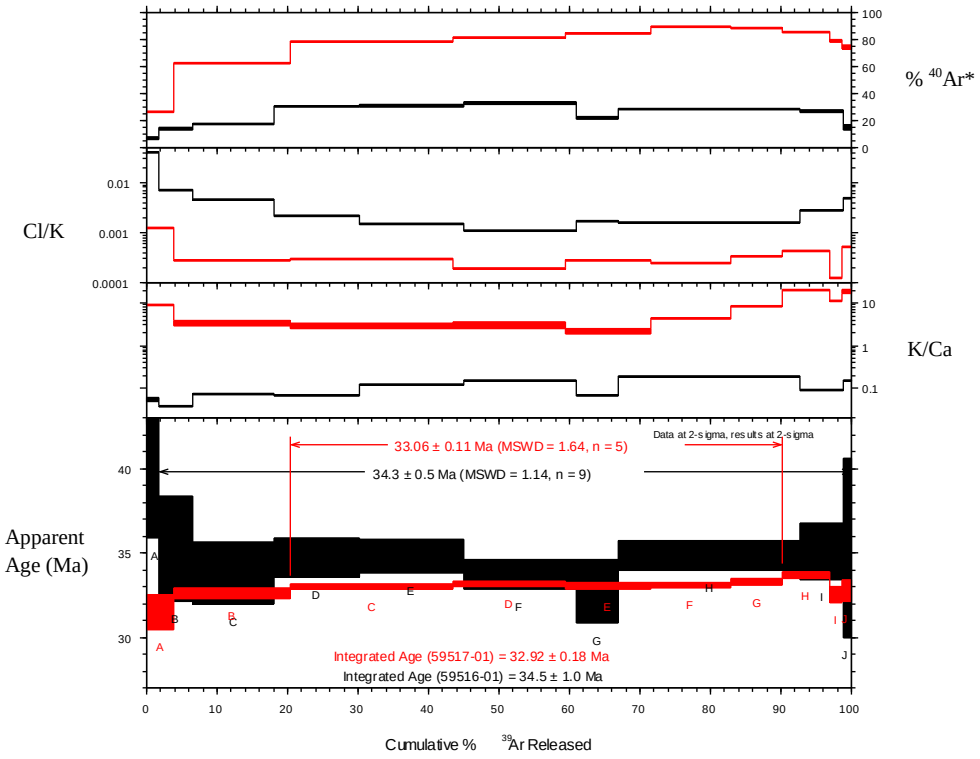

Figure 3-19: $^{40}Ar/^{39}Ar$ Step-Heating Spectra for Runs 59516-01, 59517-01 (Felsic Core). Plagioclase (black) and groundmass (red).

Plagioclase and K-feldspar step-heating results for Cp1813 2070' are shown in figure 3-20. The age spectra are discordant and do not meet the plateau criteria because it does not contain at least three contiguous steps containing at least 50 % of the gas released. The precision of individual analytical steps of the two separates are similar. For the plagioclase, a weighted-mean age was calculated for steps I through M and resulted in an age of 43.9 ± 0.9 Ma. For the K-feldspar, a weight-mean age was calculated for steps E through J and resulted in an age of 41.4 ± 0.8 Ma. The plagioclase and K-feldspar separates do not agree within 2σ error. The $^{40}Ar^*$ for both minerals start low at around 20 to 35 % and rise to around 70 %. The plagioclase Cl/K is higher, with an average around 0.006, than the K-feldspar Cl/K, which has an average around 0.003. The plagioclase

K/Ca is lower, at around 0.3, than the K-feldspar K/Ca, which has an average around 6. Figures 3-21 and 3-22 show $^{40}Ar/^{36}Ar$ intercepts greater than atmospheric argon (295.5), 360 ± 4 and 340 ± 20, respectively. The isochron ages are 38.7 ± 0.6 Ma for plagioclase and 38.3 ± 1.9 Ma for K-feldspar.

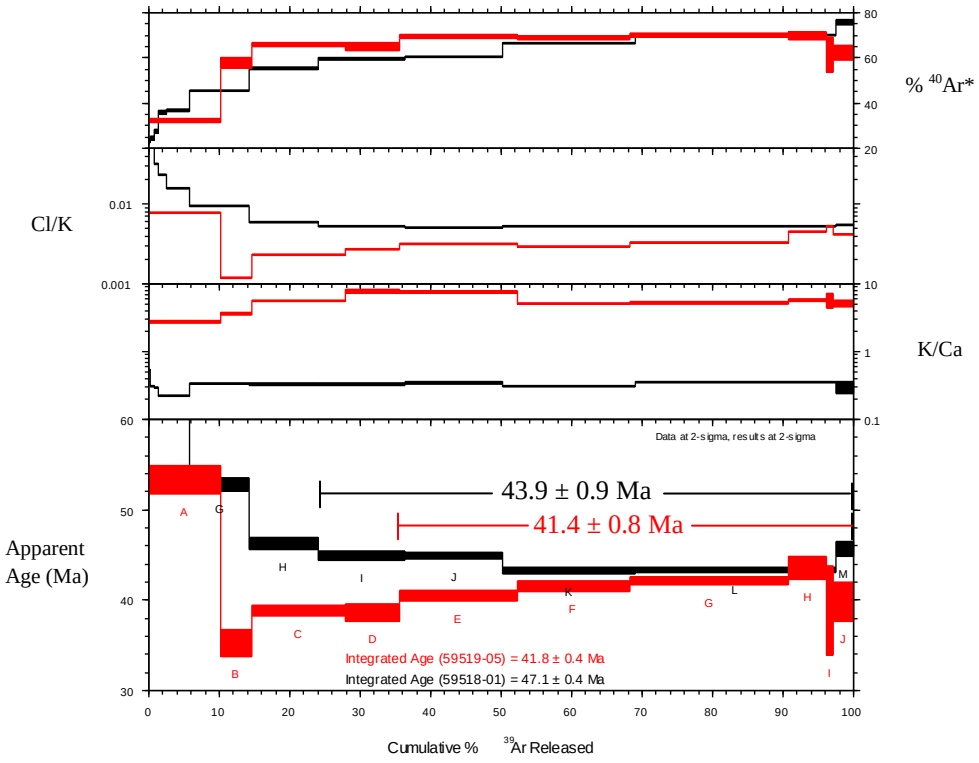

Figure 3-20: $^{40}Ar/^{39}Ar$ Step-Heating Spectra for Runs 59518-01, 59519-05 (Cp1813 2070'). Plagioclase (black) and K-feldspar (red).

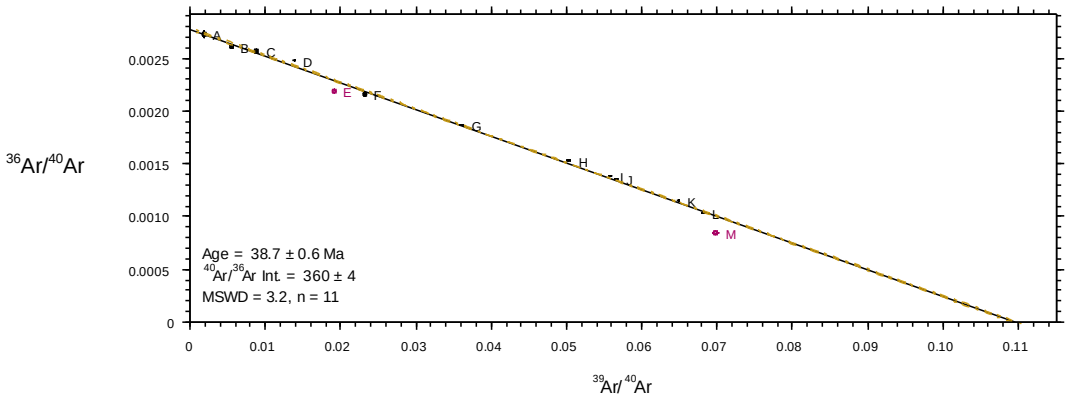

Figure 3-21: Inverse Isochron for Run 59518-01 (Cp 1813 2070', plagioclase)

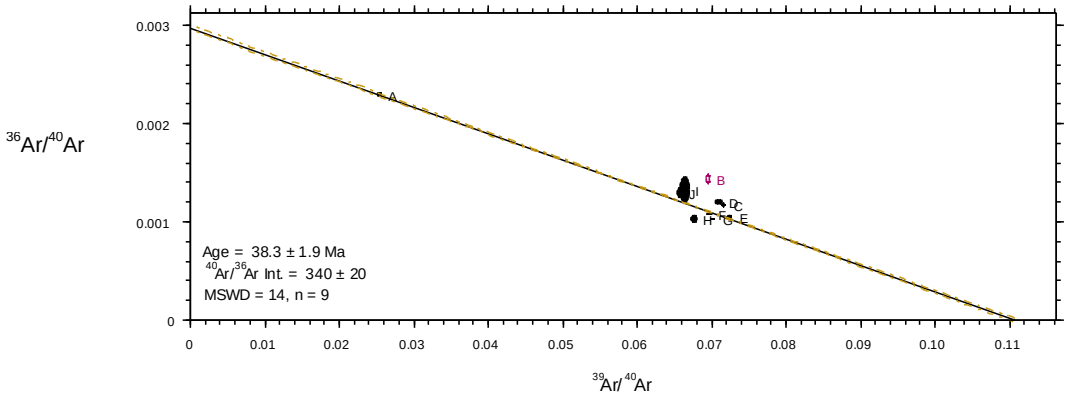

Figure 3-22: Inverse Isochron for Run 59519-05 (Cp 1813 2070', K-feldspar)

Cloudy plagioclase separates for three different rocks, Cp1813 92', Core 1, and Felsic Core, are presented in figure 3-23. The age spectra are flat and meet the plateau criteria described above. The plateaus for Cp1813 92', Core 1, and Felsic Core contain approximately 100 %, 96 %, and 98 % of the gas released, respectively. All three plateau ages have similar precision. The plateau ages for Cp1813 92', Core 1, and Felsic Core are 33.1 ± 0.5 Ma, 33.4 ± 0.5 Ma, and 34.3 ± 0.5 Ma, respectively. The plateau ages for Cp1813 92' and Felsic Core do not agree within 2σ error, although both overlap within 2σ error with the plateau age of Core 1. The $^{40}Ar^*$ for all three separates are around 30 %

or less. The Felsic Core separate has the highest $^{40}Ar^*$ with a maximum of about 34 %. The plagioclase separates for Cp1813 92' and Core 1 show similar Cl/K patterns and both have an average around 0.001. The Cl/K for Felsic Core has a similar shape as the other two separates, but it has higher Cl/K values ranging between 0.001 and 0.01. Cp1813 92' and Core 1 have similar K/Ca values with an average around 1 and Core 1 rising to 2. The Felsic Core plagioclase has a similar K/Ca pattern compared to the other two separates, but it has lower K/Ca with an average around 0.1. Figures E-5, E-9, and E-10 (Appendix E) show $^{40}Ar/^{36}Ar$ intercepts similar to atmospheric argon (295.5) and isochron ages of 33.6 ± 1.3 Ma for Felsic Core, 33.0 ± 0.9 Ma for Cp1813 92', and 33.4 ± 1.1 Ma for Core 1.

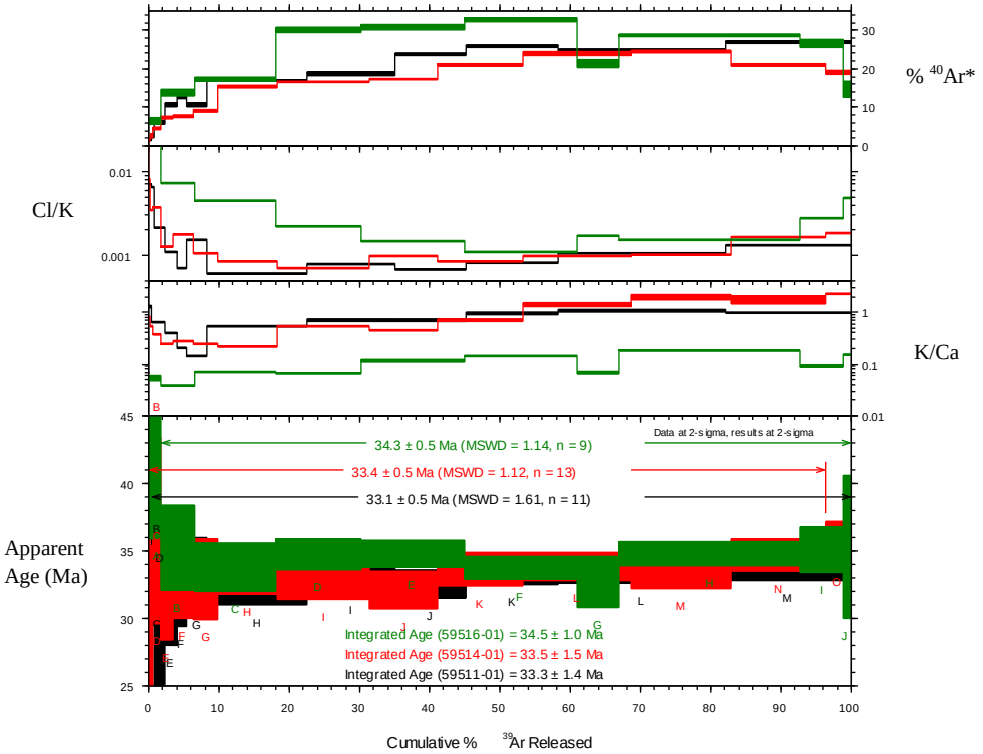

Figure 3-23: $^{40}Ar/^{39}Ar$ Step-Heating Spectra for Runs 59511-01, 59514-01, 59516-01 (Cp1813 92', Core 1, and Felsic Core). Cloudy plagioclase from Cp1813 92' (black), Core 1(red), and Felsic Core (green).

Step-heating results from Cp1813 92' and Core 1 for separates initially thought to be clear plagioclase are presented in figure 3-24. The age spectra are fairly flat and meet the plateau criteria with at least three contiguous steps containing at least 50 % of the gas released. The plateaus contain approximately 95 % and 100 % of the gas released for Cp1813 92' and Core 1, respectively. The steps for both separates are not precise and result in large errors. The plateau ages for Cp1813 92'and Core 1 are 45 ± 6 Ma and 59 ± 9 Ma, respectively. The ages agree within 2σ error. Both separates exhibit large $^{40}Ar^*$ errors. The $^{40}Ar^*$ for both separates is complex and ranges from about 5 to 40 %. The Cl/K of the first step of each separate is between 0.1 and 0.2, but the ratio immediately falls to lower values for the following steps of both separates. The Cl/K for Cp1813 92' is lower, ranging between 0.002 and 0.02, than the Cl/K for Core 1, which ranges between 0.007 and 0.03. The K/Ca for both separates is complex with the initial step starting relatively high, with values between 0.004 and 0.007. Overall, the K/Ca for Cp1813 92' is higher, with values that fall to about 0.002 and rises back to 0.009 before falling back to just above 0.001, than the K/Ca for Core 1, with values that fall to about 0.002 and levels off between 0.002 and 0.003 before rising back to about 0.004. Figure E-11 (Appendix E) shows a $^{40}Ar/^{36}Ar$ intercept similar to atmospheric argon (295.5) and an isochron age of 49 ± 10 Ma for Core 1, and figure E-12 shows a $^{40}Ar/^{36}Ar$ greater than atmospheric argon and an isochron age of 35 ± 8 Ma for Cp1813 92'.

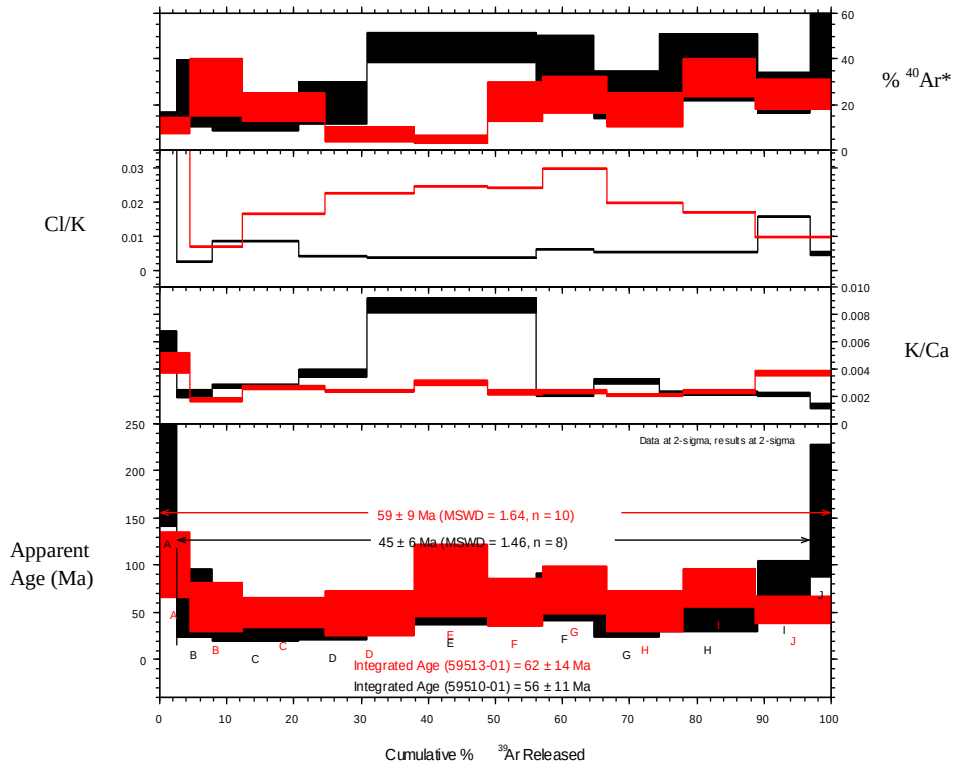

Figure 3-24: $^{40}Ar/^{39}Ar$ Step-Heating Spectra for Runs 59510-01, 59513-01 (Cp1813 92' and Core 1). Separates from Cp1813 92' (black) and Core 1 (red) were initially thought to be clear plagioclase, but in fact are calcite.

Step-heating results for biotite from Cp1813 92' and Core 1 are presented in figure 3-25. The age spectra are discordant and do not meet plateau criteria because they do not contain at least three contiguous steps containing at least 50 % of the gas released. The precision for individual analytical steps of the two separates is similar, but Cp1813 92' is a little more precise than Core 1. Weighted-mean ages calculated for Cp1813 92' and Core 1 are 73.0 ± 1.3 Ma for steps G through I and 72.3 ± 1.5 Ma for steps H through J, respectively. The weighted-mean ages agree within 2σ error. The $^{40}Ar^*$ for both separates start around 0 % and rise throughout the runs. The $^{40}Ar^*$ for Cp1813 92' is higher, rising to around 80 %, than for Core 1, rising to around 60 %. Both separates show similar Cl/K patterns with the steps starting relatively higher than the rest of the

steps. The Cl/K for Cp 1813 92' starts higher, with values starting around 0.02, than Core 1, with values starting around 0.01. Both separates have Cl/K values that fall below 0.01 with Cp1813 92' falling below the values for Core 1. Figures E-13 and E-14 (Appendix E) show $^{40}Ar/^{36}Ar$ intercepts less than atmospheric argon (295.5) and isochron ages of 75.3 ± 0.7 Ma for Cp1813 92' and 77 ± 3 Ma for Core 1.

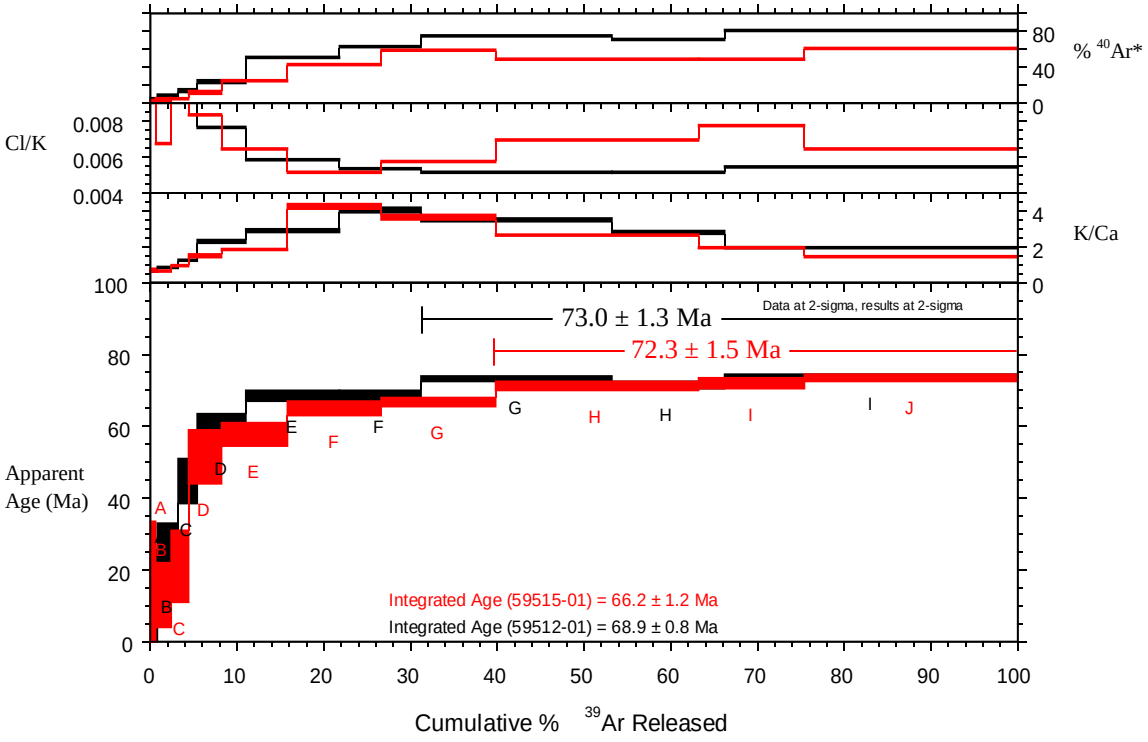

Figure 3-25: $^{40}Ar/^{39}Ar$ Step-Heating Spectra for Runs 59512-01, 59515-01 (Cp1813 92' and Core 1). Biotite from Cp1813 92' (black) and Core 1 (red).

3.3.2 Manganese Oxides

Six separates from three rock samples, SE-PKM-1, SE-bulk, and SE-PGE, were analyzed using the $^{40}Ar/^{39}Ar$ dating method. Too little sample was obtained from SE-PGD to perform any analyses.

Four cryptomelane separates from SE-PKM-1 are presented in figure 3-26. The age spectra for all four separates are mostly flat except in the beginning steps where they continue to step up. The ages of the individual analytical steps for the dendrite separates are more precise than those for the veins. All the separates meet plateau criteria. The plateaus for the veins contain approximately 85 % and 95 % and the plateaus for the dendrites contain approximately 82 % and 68 % of the gas released. The plateau ages for the dendrites are slightly younger (9.4 ± 0.5 Ma and 9.6 ± 0.4 Ma) than the plateau ages for the veins (10.31 ± 0.13 Ma and 10.37 ± 0.11 Ma). This relationship is also shown in the integrated ages. The plateau ages of the dendrites agree within 2σ error and the plateau ages of the veins agree within 2σ error, but the difference between the dendrite and vein ages is significant at 2σ error. All four separates start with a $^{40}Ar^*$ around 0 %. The dendrites have higher $^{40}Ar^*$ values, reaching around 70 % before falling back to 5 to 20 %, than the veins, with values that rise to around 20 % before falling back to 0 to 5 %. The Cl/K for all four separates start around 0.08 to 0.4, then fall to 0.01 to 0.02, with one separate falling to 0.003. The Cl/K for two of the samples levels off around 0.02 to 0.03 and the other two separates rise again to 0.05 and 0.2. The K/Ca for three of the separates starts around 2 before rising slightly and falling below 2. The K/Ca for the fourth separate stays around 1 through the analysis. Figures E-17, E-18, and E-19 (Appendix E) show $^{40}Ar/^{36}Ar$ intercepts similar to atmospheric argon (295.5) and E-20 shows a $^{40}Ar/^{36}Ar$ intercept just less than atmosphere, and the isochron ages are 10.2 ± 1.3 Ma and 10.8 ± 1.2 Ma for the veins and 10.4 ± 0.3 Ma and 10.6 ± 0.3 Ma for the dendrites.

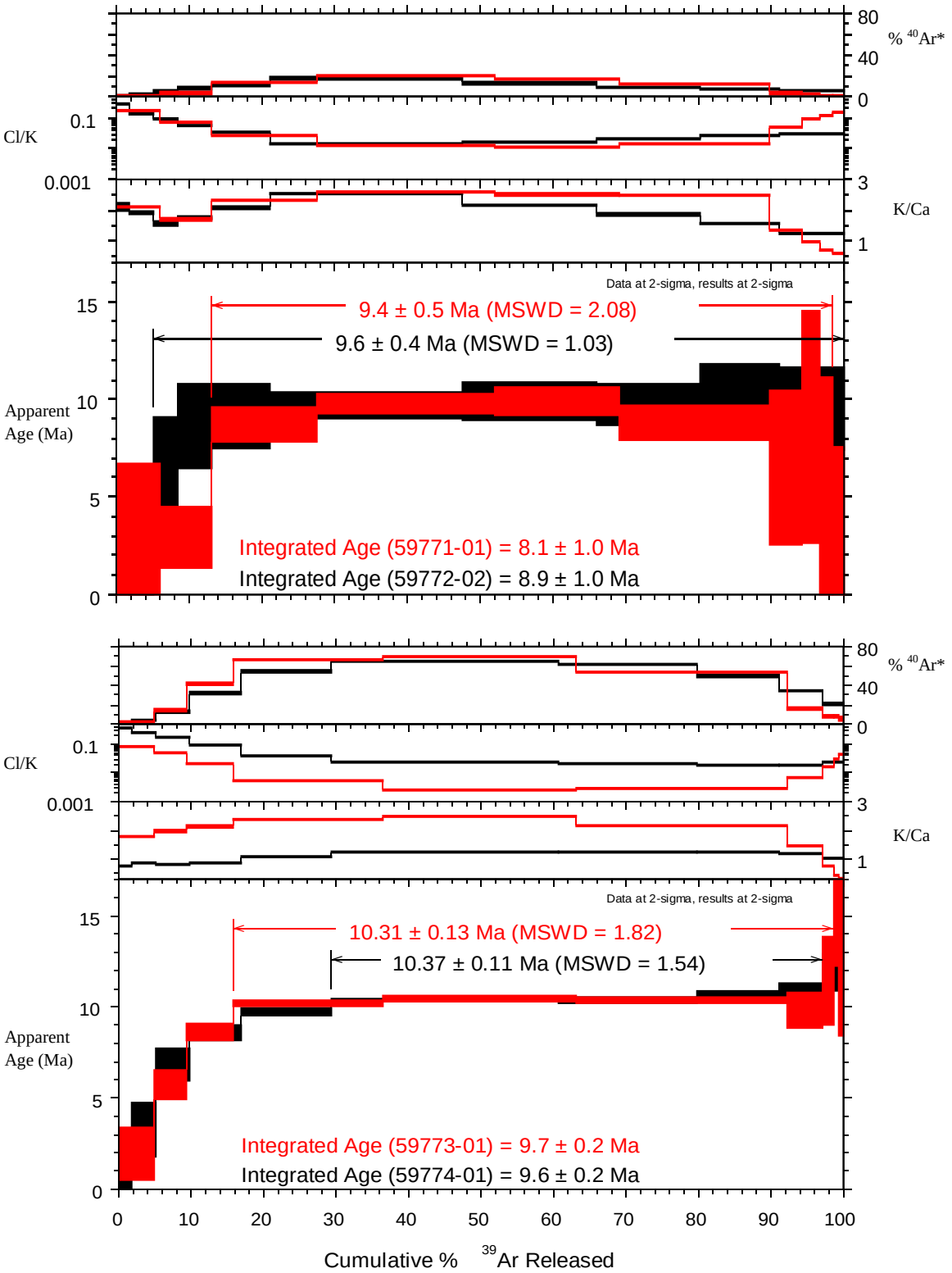

Figure 3-26: $^{40}Ar/^{39}Ar$ Step-Heating Spectra for SE-PKM-1: a) Runs 59771-01 and 59772-02 (veins); b) Runs 59773-01 and 59774-01 (dendrites).

Two todorokite separates from SE-bulk and SE-PGE are presented in figure 3-27. The age spectra are fairly flat and meet the plateau criteria with at least three contiguous steps containing at least 50 % of the gas released. The plateaus for SE-bulk and SE-PGE contain approximately 100 % and 89 % of the gas released, respectively. The steps for SE-bulk are more precise than the steps for SE-PGE. Both separates have low $^{40}Ar^*$ values that start around 0 % and slowly rise to almost 20 % before falling back down slightly. As the $\%^{39}Ar$ released increases, the errors in $^{40}Ar^*$ increase. The Cl/K for Se-bulk is lower, with values that slowly fall from 0.2 to 0.1 through the analysis, than SE-PGE, with values that stay around 0.4 through the analysis. The K/Ca for SE-bulk starts higher, with values around 0.25, than SE-PGE, which has values around 0.35. After the initial steps the K/Ca for SE-bulk, with values that fall to around 0.4 before rising to 0.08, falls below values for SE-PGE, with values that fall to about 0.1 and rise back to about 0.3. The plateau ages for SE-bulk and SE-PGE are 1.9 ± 0.4 Ma and 5.1 ± 1.7 Ma, respectively. The plateau ages are within 2σ error of the total gas ages for each of the separates. The plateau ages do not agree within 2σ error. Figures E-21 and E-22 (Appendix E) show $^{40}Ar/^{36}Ar$ intercepts similar to atmospheric argon (295.5) and isochron ages are 1.9 ± 0.5 Ma and 4.3 ± 1.5 Ma for SE-bulk and SE-PGE, respectively.

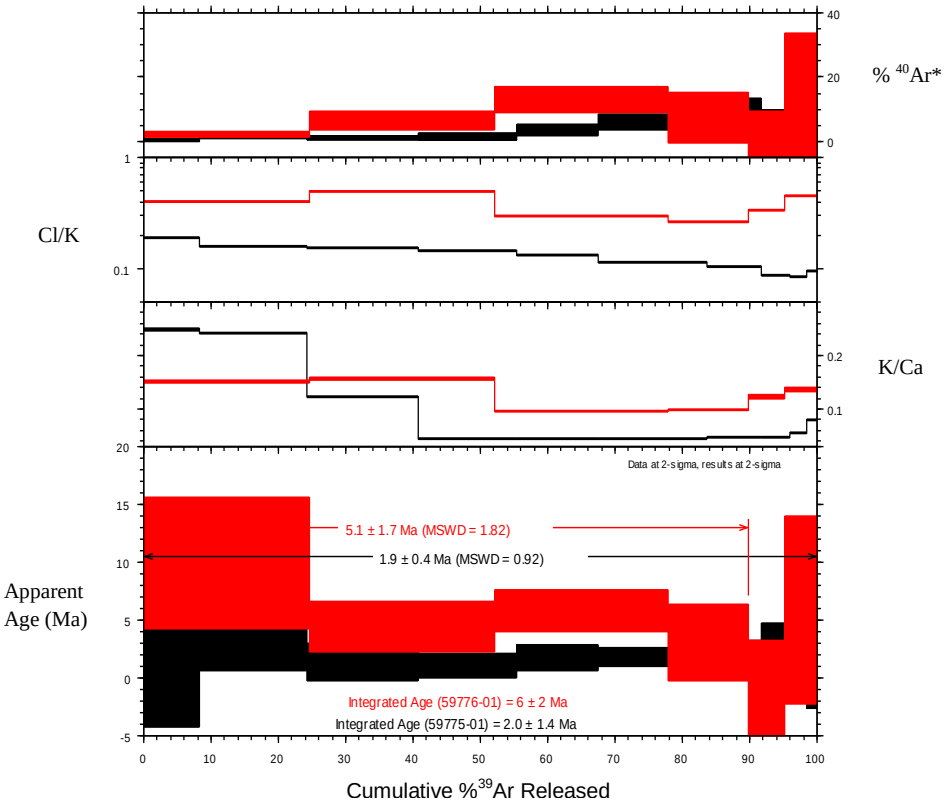

Figure 3-27: $^{40}Ar/^{39}Ar$ Step-Heating Spectra for Runs 59775-01, 59776-01 (SE-bulk and SE-PGE). Todorokite from SE-bulk (black) and SE-PGE (red).

4. DISCUSSION

4.1 Mineralogy and Geochronology of the Intrusive Rocks

Four intrusive rocks from drill hole Cp1813 (Figure 3-18) were analyzed using X-ray diffraction and the $^{40}Ar/^{39}Ar$ dating method. XRD was used to identify the minerals analyzed in the $^{40}Ar/^{39}Ar$ analyses. The dating was performed to better understand the timing of emplacement for the intrusive rocks and clear up a discrepancy between the K/Ar dates and field relationships.

4.1.1 Mineral Identification

X-ray diffraction was used to identify the minerals present in separates from the intrusive rocks prepared for $^{40}Ar/^{39}Ar$ analyses. The separates used for XRD analyses are not the same aliquots used for the dating analyses because the XRD was deemed necessary only after the step-heating spectra results. Most of the visual mineral identification performed during sample preparation for the dating process was correct, but two of the separates, thought to be a clear plagioclase, were incorrectly identified. Figure 3-24 shows the step-heating spectra for the "clear plagioclases' and both separates exhibit large $^{40}Ar^*$ and age errors. XRD results from these separates (Figures C-1 and C-2) show peaks for calcite. This means the minerals prepared for $^{40}Ar/^{39}Ar$ analyses were really calcite and not plagioclase and these samples will not be considered further.

The other mineral separates analyzed by XRD include cloudy plagioclase, K-feldspar, and biotite. The analyses of cloudy plagioclase (Figures C-3 though C-6) indicate the presence of albite and montmorillonite; albite, anorthoclase, and marialite; albite; and anorthoclase for Felsic core, Cp1813 2070', Cp1813 92', and Core 1, respectively. The K-feldspar for Cp1813 2070' (Figure C-7) was determined to be anorthoclase. Figures C-8 and C-9 are the biotite separates for Cp1813 92' and Core 1, respectively.

4.1.2 Geochronology

Felsite- The groundmass step-heating plateau age of 33.06 ± 0.11 Ma is more precise than the plagioclase step-heating plateau age of 34.3 ± 0.5 Ma at 2σ because the groundmass separate exhibits a higher radiogenic yield and greater K_2O% than the plagioclase. The age of 33.06 ± 0.11 Ma is considered the best age for the felsites (Figure 3-19). The previously determined K/Ar age of 26.6 Ma (Clark et al., 1979) is deemed inaccurate, and the age of 33.06 ± 0.11 Ma determined through $^{40}Ar/^{39}Ar$ dating is considered the most appropriate age for the felsite. This $^{40}Ar/^{39}Ar$ age confirms the geologic interpretation made by Megaw (1990) that the felsites are older than the 32.2 ± 0.4 Ma lamprophyres.

Quartz Monzonite- The plagioclase and K-feldspar mineral separates exhibit $^{40}Ar/^{36}Ar$ intercepts greater than atmosphere (Figure 3-21, 3-22), which may be interpreted as excess argon. Therefore, the isochron ages are considered the best ages for the mineral separates. The plagioclase $^{40}Ar/^{36}Ar$ intercept is more precise than the intercept for the K-feldspar, and the MSWD is better at 3.2 for eleven steps for the

plagioclase than the MSWD of 14 for nine steps for the K-feldspar. For these reasons the plagioclase isochron age of 38.7 ± 0.6 Ma is better constrained than the K-feldspar isochron age of 38.3 ± 1.9 Ma at 2σ error and is considered the best age for this rock.

Diabase Sills- The ages of all three of the minerals are consistent between the two diabase sill samples (Figures 3-23 through 3-25). Step-heating spectra from the "clear plagioclase," now known to be calcite, show large errors (Figure 3-24) and will not be considered in the age determinations for the rocks. The biotite step-heating spectra start young and increase in age as the amount of ^{37}Ar released increases, which suggests argon loss (Heizler et al., 1988). An artifact of this argon loss is the $^{40}Ar/^{36}Ar$ intercepts are less than atmosphere. The biotite separates approach minimum ages of 73.0 ± 1.3 Ma and 72.3 ± 1.5 Ma for Cp1813 92' and Core 1, respectively. The cloudy plagioclase separates for both rocks are interpreted to be re-set to a younger age, similar in age to the felsite, than the crystallization age of the rocks. It is interpreted that the felsite heated the diabase sills enough to re-set the cloudy plagioclase ages and only started to re-set the biotite ages for the two rocks. Therefore the best ages for the diabase sills are the minimum ages of the biotite separates with 73.0 ± 1.3 Ma for the upper sill and 72.3 ± 1.5 Ma for the lower sill.

Figure 4-1 shows the age distributions of the K/Ar and $^{40}Ar/^{39}Ar$ dates for the intrusive rocks. There are three different pulses of magmatism in the district with the diabase sills intruding at minimum ages of 73.0 ± 1.3 Ma and 72.3 ± 1.5 Ma, the quartz monzonite intruding at 38.7 ± 0.6 Ma, the felsites intruding at 33.06 ± 0.11 Ma, and finally the lamprophyres intruding at 32.2 ± 0.4 Ma. The K/Ar age of the felsite was found to be inaccurate and the new felsite age determined the felsite is older than the

lamprophyre. This more accurate age resolves an inconsistency in the K/Ar dates and is now consistent with cross-cutting relationship identified in the field by Megaw (1990).

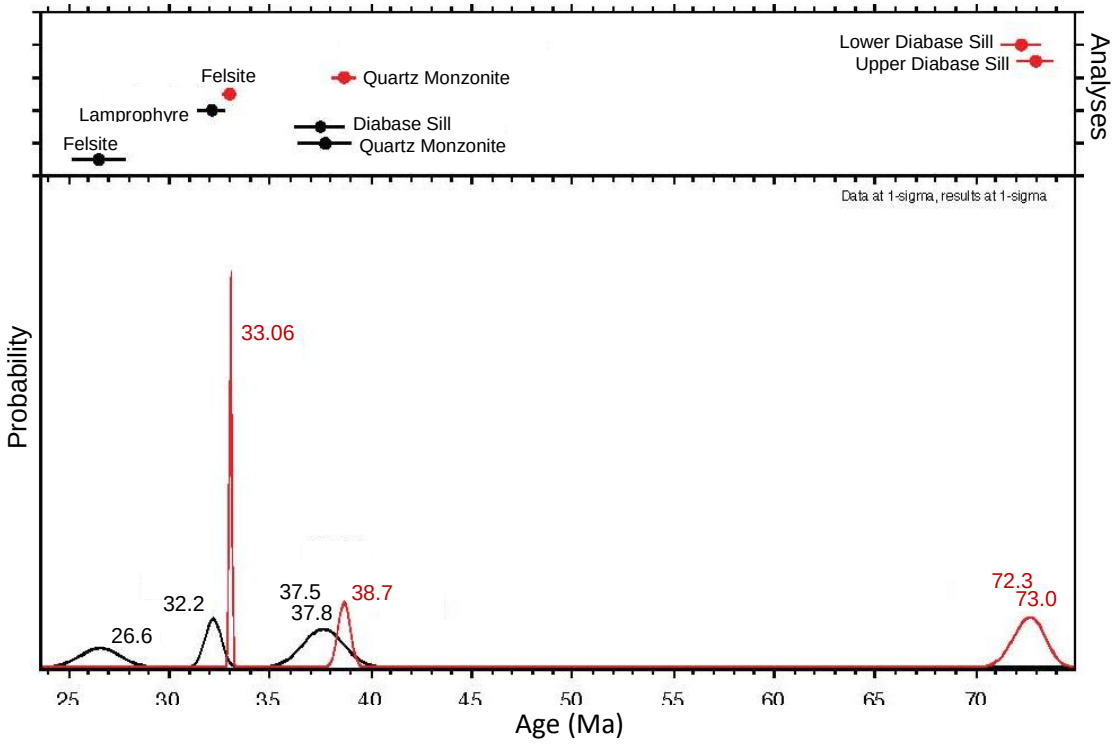

Figure 4-1: K/Ar (black) (Clark et al., 1979; Megaw, 1990) and $^{40}Ar/^{39}Ar$ (red) age distribution for the intrusive rocks. Ages on the diagram do not necessarily correspond to individual ages. The errors for the $^{40}Ar/^{39}Ar$ ages are at 1σ error. For convenience, the K/Ar errors are set at 1, except for the lamprophyre where it is set at 0.4.

4.2 Mineralogy and Geochronology of the AMOM

4.2.1 Mineral Identification

Previous attempts have been made to identify the manganese minerals of the Argentiferous Manganese Oxide Mineralization (AMOM) at Santa Eulalia (Prescott, 1916; Hewitt, 1968; Megaw, 1990). Megaw (1990) compiled a list of minerals identified in the carbonate-hosted surface alteration and AMOM including aragonite, argentojarosite, calcite, cryptomelane, dolomite, fluorite, galena, goethite, gypsum,

hematite, hollandite, “limonite”, plumbojarosite, proustite, pyrargyrite, pyrolusite, quartz, ramsdellite, native silver, and “wad.” This study indentified cryptomelane, coronadite, chalcophanite, birnessite, and todorokite as the manganese minerals and goethite, quartz, as well as clays including talc and illite in the carbonate-hosted AMOM (Table 3-2).

Although many minerals identified in this study have previously been noted at Santa Eulalia, this study shows a greater variety of AMOM minerals to be hosted in the carbonate than previous studies. The list of minerals identified in this study more closely matches the volcanic-hosted minerals than the carbonate-hosted list of minerals compiled by Megaw (1990) for Santa Eulalia. The manganese minerals identified in the AMOM at Santa Eulalia are not unique to the location. Many geothermal systems and ore deposits not associated with magmatic hydrothermal systems also exhibit similar mineralogies (Hewett and Radtke, 1967; Radtke et al., 1967; Chafetz et al., 2004).

4.2.2 Geochronology

Six manganese oxide separates from three rock samples were analyzed using the $^{40}Ar/^{39}Ar$ method. Four of these separates are cryptomelane from SE-PKM-1. Of these four separates, two are from veins and two are from manganese oxide dendrites. The step-heating spectra gives plateau ages of 10.31 ± 0.13 Ma and 10.37 ± 0.11 Ma for the veins and 9.4 ± 0.5 Ma and 9.6 ± 0.4 Ma for the dendrites (Figure 3-26). The difference in ages between the two textures (Figure 2-1) may indicate that manganese mineralization in this rock occurred over a period of 1 million years with the dendrites forming within the rock and then about 1 million years later the veins cut through the rock.

The other two separates analyzed, using the $^{40}Ar/^{39}Ar$ method, are todorokite from SE-bulk and SE-PGE. The step-heating spectra give plateau ages of 1.9 ± 0.4 Ma and 5.1 ± 1.7 Ma for SE-bulk and SE-PGE, respectively (Figure 3-27). All three rocks containing manganese oxide are of different ages indicating episodic mineralization events over a long duration of time. The manganese oxide rocks are younger than the felsites by 22.69 to 31.16 million years indicating the manganese oxide mineralization is not temporally related to the felsites. This also indicates that the AMOM we analyzed is not from the same mineralizing event at the sulfide mineralization. Some of the AMOM occurrences, especially those with Ag, may be part of the sulfide mineralization process, and some AMOM may be a supergene mineralization related to the sulfide ores. Without additional dating of the various AMOM occurrences and understanding the processes forming the AMOM, it is unclear whether the presence of AMOM as an exploration tool is applicable to finding additional sulfide ores.

4.3 Stable Isotopes of Santa Eulalia

The carbon and oxygen stable isotope values for Santa Eulalia are plotted in figure 3-9. Because most of the samples analyzed were limestone and may not have been in equilibrium with hydrothermal fluids, we are not able to calculate fluid compositions for this trend. The carbon and oxygen values get lighter approaching the sulfide veins or veins with no ore (Figures 3-10 and 3-11). The $\delta^{13}C$ values are above background levels, unaltered limestone values, except for the manganese altered limestone analyses taken close to the ore vein and the ore calcite for the Buena Tierra Mine and San Antonio Mine. The $\delta^{18}O$ values are all below background levels, unaltered limestone values, except for

two limestone samples from the Buena Tierra Mine. The Buena Tierra limestone $\delta^{18}O$ value at 230 m is depleted because the sample location is close to another vein (Megaw, 1990). Megaw (1990) found the carbon and oxygen isotope values are at background levels in the unaltered limestone and are depleted within the AMOM (Figure 4-2). It is apparent that AMOM is epigenetic.

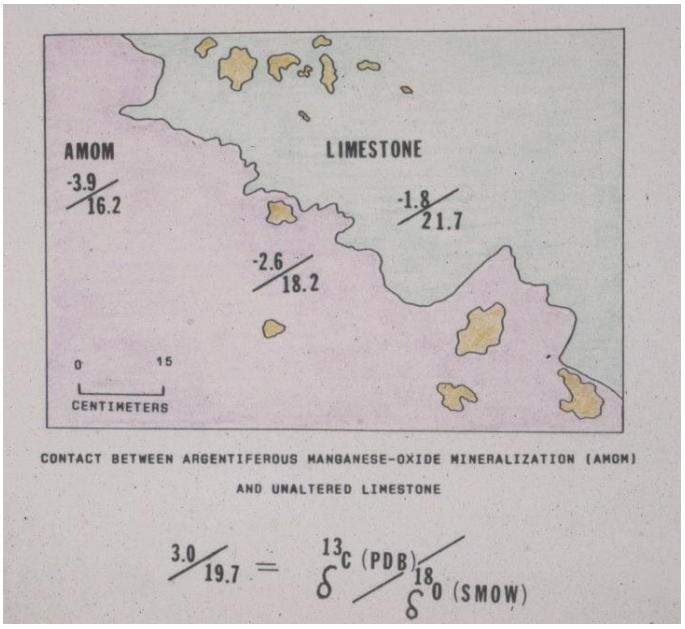

Figure 4-2: Relationship of carbon and oxygen isotope values within AMOM and unaltered limestone. Courtesy of Megaw (1990).

The carbon and oxygen isotope systematics for Santa Eulalia and Luis Lopez are very different. Santa Eulalia displays a direct correlation between the carbon and oxygen isotopes (Figures 3-10 and 3-11), but Luis Lopez exhibits an inverse relationship in the $\delta^{13}C$ and $\delta^{18}O$ values of calcite and in the $\delta^{13}C_{HCO3-}$ and $\delta^{18}O_{H2O}$ fluid values (Figures 3-12 and 3-13).

4.4 The Origin of AMOM

The ages for the three manganese oxide rocks, dated in this study using the $^{40}Ar/^{39}Ar$ method, indicate they formed around three distinct times of approximately 10 Ma, 5 Ma, and 2 Ma for SE-PKM, SE-PGE, and SE-bulk, respectively. These ages are more than 20 Ma younger than the felsites, of approximately 34 Ma, which are inferred to be the source of sulfide mineralization. Due to the difference in ages, the AMOM analyzed in this study was not formed during the main stage of sulfide mineralization.

The AMOM studied for this project at Santa Eulalia is episodic over 8 million years as seen by the three distinct ages of approximately 10 Ma, 5 Ma, and 2 Ma. In addition, Megaw (1990) noted the AMOM is found above, below, or next to the sulfide mineralization suggesting no clear stratigraphic control. No magmatic activity coincident with the ages determined for AMOM is apparent in the study area. A model representing the processes responsible for the AMOM needs to account for these important characteristics.

Two models, a weathering model and a hot spring model, may account for the characteristics observed and explain the processes that formed the AMOM at Santa Eulalia. These models will be discussed, but more evidence is needed to determine which model best accounts for the characteristics of the AMOM at Santa Eulalia.

4.4.1 Weathering Model for AMOM at Santa Eulalia

Manganese oxides may form due to weathering processes as suggested by Spurr (1911) (Figure 4-3). Fluids, usually with a meteoric origin, percolate down from the surface and weather the sulfides and dissolved constituents are precipitated in other

minerals such as manganese minerals. It may be difficult to differentiate between manganese oxides formed during weathering and manganese oxides formed due to hypogene processes. The ages of manganese oxides formed due to weathering should be younger than the sulfides they originate from. Due to the weathering fluids originating stratigraphically higher than the sulfides, the manganese oxides should be located either next to or below the sulfides. Because the AMOM is found above, next to, or below sulfide mineralization, and in the volcanic series, it seems the formation of the AMOM due to weathering is less likely unless there was a stratigraphically higher sulfide that has been weathered away.

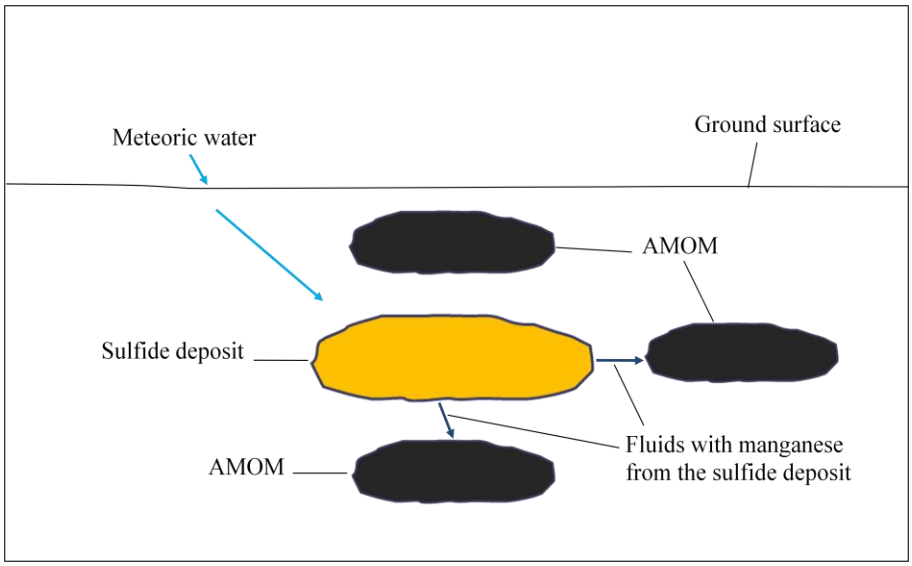

Figure 4-3: Schematic weathering model for the formation of AMOM based on Spurr (1911) and observations of Megaw (1990).

4.4.2 Hot Spring Model for AMOM at Santa Eulalia

Santa Eulalia is located near a major north-south trending fault (Figure 4-4) in Mexico that separates major tectono-stratigraphic terranes. Along this same fault are

other mineral deposits of similar age which are not associated with magmatism. Peña Blanca, a uranium deposit approximately 50 km north of Chihuahua, Mexico (Figure 4-4) is located west of the major north-south trending fault. It is associated with deep seated upwelling of thermal waters similar to many hot springs along the Rio Grande Rift (Lueth et al., 2005). Interestingly the hydrothermal jarosite at Peña Blanca was determined to be 9.42 ± 0.11 Ma (Lueth et al., 2005), which is similar to the AMOM ages determined for the veins in SE-PKM at Santa Eulalia.

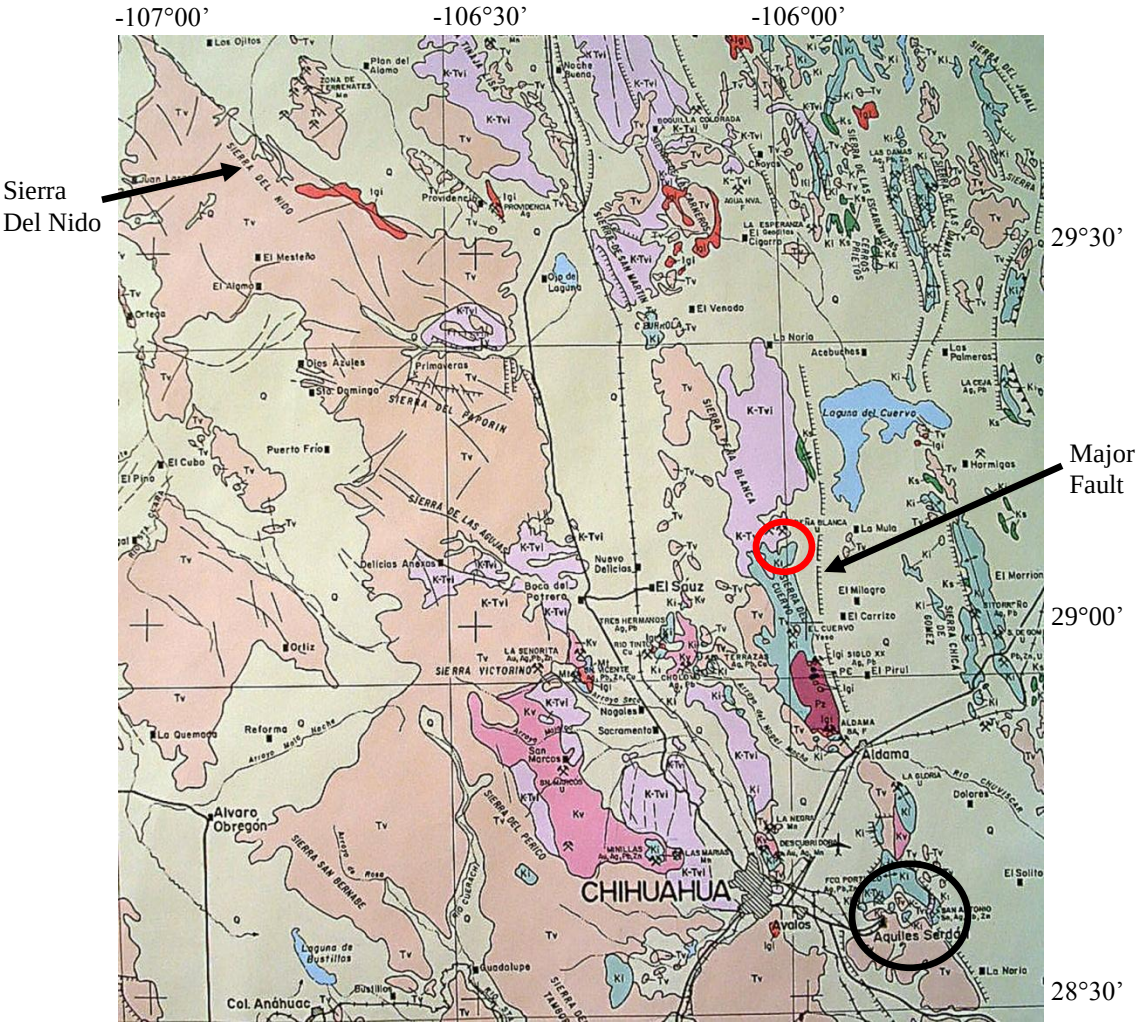

Figure 4-4: Location of Santa Eulalia, outlined in black, and Peña Blanca, outlined in red, near Chihuahua, Mexico (Mexicana, 1985).

Other galena-barite-fluorite ore deposits along the Rio Grande Rift (RGR-type of McLemore, et al. 1998) in the Southern Basin and Range in Mexico have hydrothermal jarosite ages that illustrate episodic mineralization events occurring over 10 million years of time (Lueth et al., 2005). A good example of their work is the Hansonburg mining district in New Mexico with a wide range of hypogene jarosite mineralization ages at 3.79 ± 0.16 Ma, several ages around 6 Ma, and 7.97 ± 0.44 Ma. Lueth et al. (2005) proposed the jarosite at Peña Blanca and other areas of galena-barite-fluorite deposits along the Rio Grande Rift were formed by deep circulation of saline brines within Rio Grande Rift and basin and range style faults that rupture and move periodically creating a conduit for the fluids (Figure 4-5). Their model is based heavily on geological information from Clemons (1996) and hydrologic modeling of Mailloux et al. (1999).

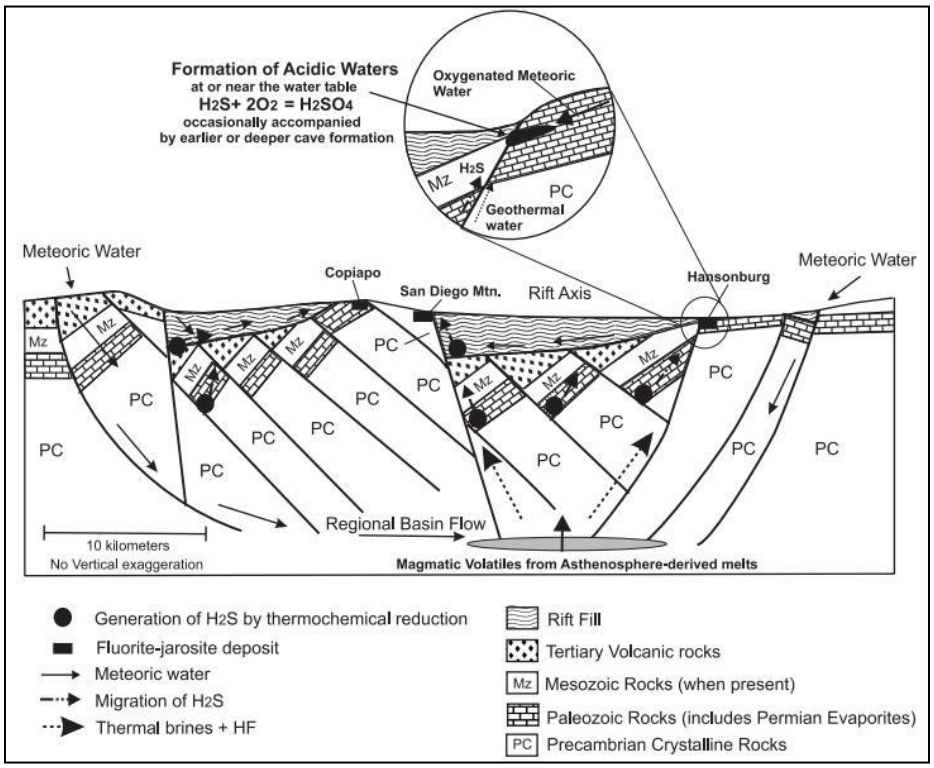

Figure 4-5: Model for deep fluid circulation and precipitation of hydrothermal minerals in faults (Lueth et al., 2005).

RGR deposits and manganese oxides may occur in similar hydrothermal environments and are spatially found together in some areas such as a hot spring area at San Diego Mountain near Hatch, New Mexico (Seager et al., 1971; Lueth et al., 2005) in which jarosite and manganese oxides are spatially related. Figure 4-6 shows a schematic cross-section of the possible relationships between jarosite and manganese mineralization and the hot spring deposits that formation at the surface. The close association of galena-barite-fluorite (RGR) deposits and manganese mineralization has been noted by others (McLemore et al., 1998; Witcher, 1998). The close association of hot springs and manganese mineralization was noted long ago by Wells (1918) when describing the manganese oxides forming in a hot spring environment at the Ellis deposit near Truth or Consequences, New Mexico when he said;

> "At the southeast end of the manganiferous beds, hot springs from which the town is named issue from the limestone underlying the sandstone. In view of the structure of the ore and the presence of springs at one extremity of the mineralized section, it seems highly probable that these deposits have been due to manganese-bearing solutions rising upward through pipes and conduits and entering an oxidizing environment which caused the deposition of manganese in an oxide form."

Areas along the Rio Grande Rift with manganese deposits also have active geothermal waters. Manganese oxide deposits, believed to have been formed in a hot spring environment, at Tortuga Mountain near Las Cruces, New Mexico (King and Kelley, 1980) are located in close proximity to the Las Cruces Geothermal Field (Lueth et al., 2002). Lueth et al. (2005) also found the fluids responsible for the precipitation of jarosite at Peña Blanca and other RGR deposits have a similar isotopic composition as geothermal waters in the area today.

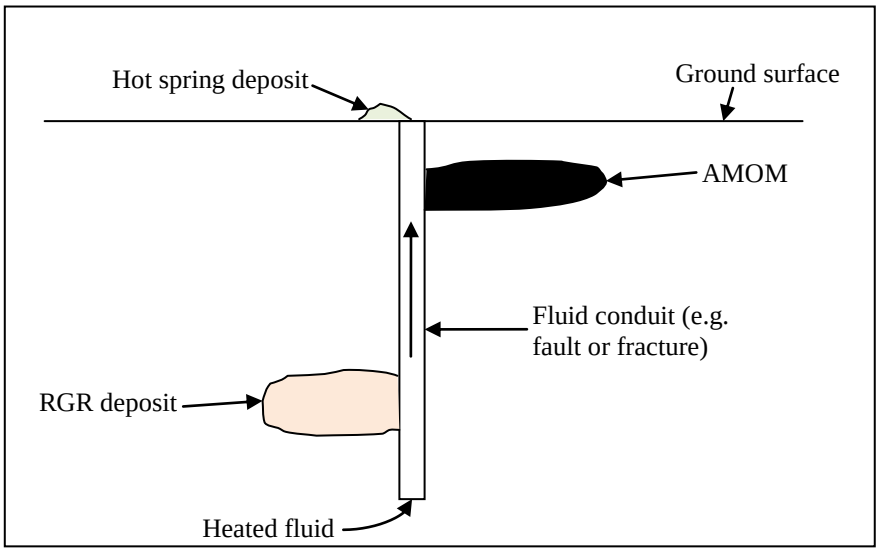

Figure 4-6: Schematic cross-section of possible relationships between RGR, manganese, and hot spring mineralization. AMOM mineralization is not necessarily associated with RGR deposits.

The model proposed by Lueth et al. (2005) for the formation of RGR deposits is adapted for the formation of the AMOM at Santa Eulalia and is presented in figure 4-7. The Calera-del Nido tectonic block, containing Sierra del Nido (Figure 4-4), formed from basin and range tectonics in Chihuahua, Mexico, has been uplifted (Mauger, 1981) and may have created a regional groundwater flow from west to east similar to the model presented by Mailloux et al. (1999). Due to the possible regional ground water flow from west to east, in this model meteoric water flows down faults in the west, circulates deep, and flows back up through eastern faults. Alternatively, fluids may be derived from the basins of the Chihuahua Trough and may move from east to west. As the fluids move up the faults and reach the right conditions, it precipitates the manganese oxide minerals. This model may better represent the processes that formed the AMOM at Santa Eulalia.

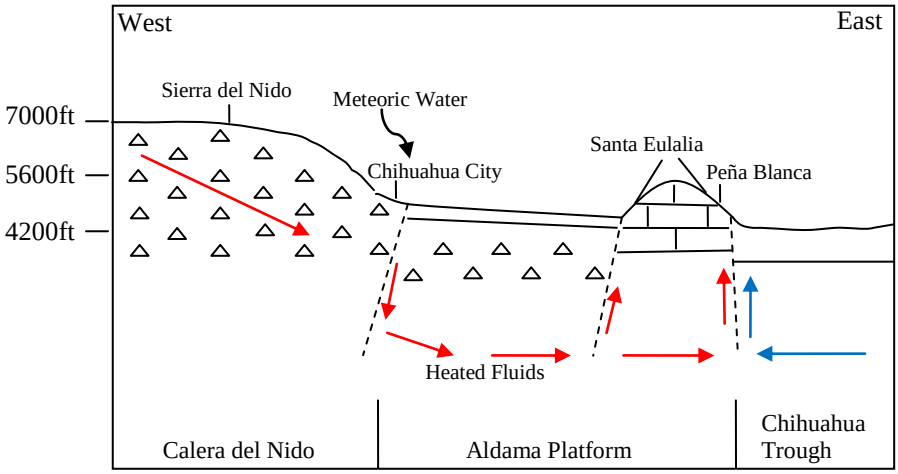

Figure 4-7: Schematic model for the precipitation of AMOM at Santa Eulalia with fluid movement based on Mailloux et al. (1999) (red) and fluid movement based on basin dewatering-MVT type from the east (blue). The cross-section is based on Mauger (1983a), Mauger (1983b), and Pingitore Jr., et al. (1983).

4.5 Stable Isotopes of Luis Lopez

The initial hypothesis that AMOM is related to the sulfide mineralization warranted the stable isotope study of Luis Lopez and comparison to Santa Eulalia. The variation in carbon and oxygen isotope values for Luis Lopez and Santa Eulalia are very different. Luis Lopez exhibits an inverse relationship in the $\delta^{13}C$ and $\delta^{18}O$ values of calcite and in the calculated $\delta^{13}C_{HCO3-}$ and $\delta^{18}O_{H2O}$ fluid values (Figures 3-12 and 3-13), whereas Santa Eulalia has more of a coupled relationship between the carbon and oxygen isotopes (Figures 3-10 and 3-11). Because the stable isotope data at the two locations are so different, the Luis Lopez Manganese District will be treated and presented separate from Santa Eulalia.

One interpretation of the relationship of the $\delta^{13}C_{HCO3-}$ and $\delta^{18}O_{H2O}$ fluid values at Luis Lopez (Figure 3-13) is mixing of two fluids. Both fluid end members exhibit oxygen isotope values that are considered heavy. The end member fluid with the heavy carbon,

about 2.0 ‰ $\delta^{13}C_{HCO3-}$, and oxygen of about 9.5 ‰ $\delta^{18}O_{H2O}$, values may be similar to fluids from a playa lake environment, where organic fractionation makes the carbon isotope heavier, but there is a meteoric component for the oxygen that had undergone Rayleigh fractionation. Playa lakes are known in the local geologic record (Chapin and Lindley, 1986) and have been hypothesized to have been responsible for K-metasomatism and enrichment in $\delta^{18}O$ of rocks. The other end member has very heavy oxygen, about 24.7 ‰ $\delta^{18}O_{H2O}$, with light carbon, about -6.4 ‰ $\delta^{13}C_{HCO3-}$. It is more difficult to understand the fluid end member this may represent.

A second interpretation of the variation in carbon and oxygen calcite values is temperature variation with a constant $\delta^{13}C_{HCO3-}$ and $\delta^{18}O_{H2O}$ fluid value. Using end member mineralization temperatures determined by Norman et al. (1983) by fluid inclsion analyses for different Luis Lopez mine areas and equations from Deines et al. (1974) and Kim and O'Neil (1997) the carbon and oxygen isotopes of calcite were calculated, respectively. Using an average and constant fluid value of -2.0 ‰ $\delta^{13}C_{HCO3-}$ and 17.3 ‰ $\delta^{18}O_{H2O}$ for the MCA mine with temperatures of 175 and 375 °C the values of -3.4 and -3.1 ‰ for $\delta^{13}C$ and 25.1 and 12.7 ‰ for $\delta^{18}O$ were calculated, respectively. These calculations result in a potential variation of 0.3 ‰ in $\delta^{13}C$ and 12.4 ‰ in $\delta^{18}O$. These effects of temperature on fractionation may account for the range in mineral oxygen values seen at Luis Lopez, but it does not explain the range in composition of the carbon.

The fluid source and controls for the calcite isotopic composition at Luis Lopez is still unclear. Although the trend looks like it may represent a mixing line, only one end member fluid is easy to understand and the source of fluid for the second end member is

still unidentified. The extremely heavy oxygen isotopic composition of this end member is decidedly unusual. The individual calcite bands of rocks at Luis Lopez and Water Canyon mostly vary along linear trends indicating mixing as one of the controls on the formation of the calcite bands (Figures 3-14 through 3-17). Although several samples show variation along the linear trend, the direction of movement, toward the upper or lower end member, is not consistent. What ever caused the variation seems to have varied in a cyclic, not monotonic, fashion. The oxygen isotopes of the calcite may represent a range in temperatures, but the carbon cannot be explained by changes in temperature and what may cause the changes in temperature is unclear. Although only two possible controls on the formation of the calcite bands are presented here, there may be other processes such as boiling or effervescence that were not considered in detail.

5. CONCLUSIONS

$^{40}Ar/^{39}Ar$ dating analyses determined the ages of the felsite, quartz monzonite, upper diabase sill, and lower diabase sill at Santa Eulalia as 33.06 ± 0.11 Ma, 38.7 ± 0.6 Ma, 73.0 ± 1.3 Ma, and 72.3 ± 1.5 Ma, respectively. The new ages of the felsite and diabase sills resolve the incompatibility of the K/Ar between ages of the felsite, diabase sills, and lamprophyres. The new ages put the felsite and diabase sills as older than the lamprophyres, and the ages are now compatible with field relationships. The diabase sills show evidence of resetting by the hydrothermal system associated with the felsites.

The mineralogy of the AMOM determined through electron microprobe and X-ray diffraction analyses include cryptomelane, coronadite, birnessite, and todorokite as the manganese oxides, as well as calcite, quartz, goethite, and clays including illite and talc. The ages of the AMOM are approximately 10 Ma, 5 Ma, and 2 Ma and indicate the AMOM analyzed in this study did not form during the main stage of sulfide mineralization caused by the felsite.

The formation of the AMOM analyzed in this study may be explained by two different models. The weathering model and the hot spring model may account for the characteristics observed at Santa Eulalia. The weathering model would require a stratigraphically higher sulfide deposit that has been weathered away. The hot spring model depends on the circulation of deep basinal fluids that rise up through faults and deposit the manganese minerals. More AMOM samples need to be examined to

determine if there is more than one kind of AMOM present at Santa Eulalia and the appropriateness of each model to represent the processes that formed the specific AMOM observed.

There is a direct relationship between carbon and oxygen stable isotope values at Santa Eulalia. Both the carbon and oxygen are depleted close to veins and are near background levels further from veins.

The carbon and oxygen isotopes at Luis Lopez and Water Canyon exhibit an inverse relationship, and the individual bands of calcite in different rocks mostly vary along linear trends. There are three possible explanations for the isotope values at Luis Lopez: 1) Mixing of two fluids, with one end member a playa lake fluid with a meteoric influence. The other end member is more difficult to explain; 2) Changes in temperature can account for the range in oxygen values, but the changes in the carbon values due to temperature are too small to account for the changes seen; or 3) There may be other processes, such as boiling and effervescence, which were not fully examined here.

APPENDIX A. SAMPLE PHOTOS

Santa Eulalia AMOM

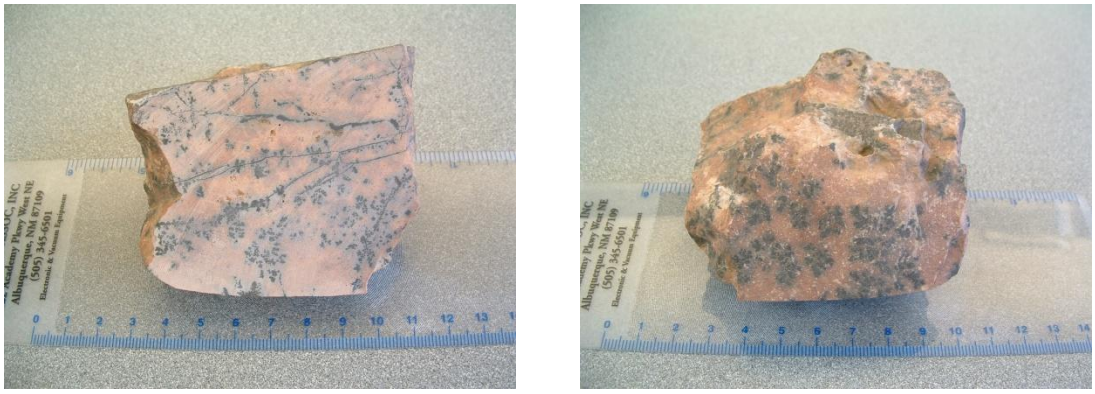

Figure A-1: SEPKM rock sample.

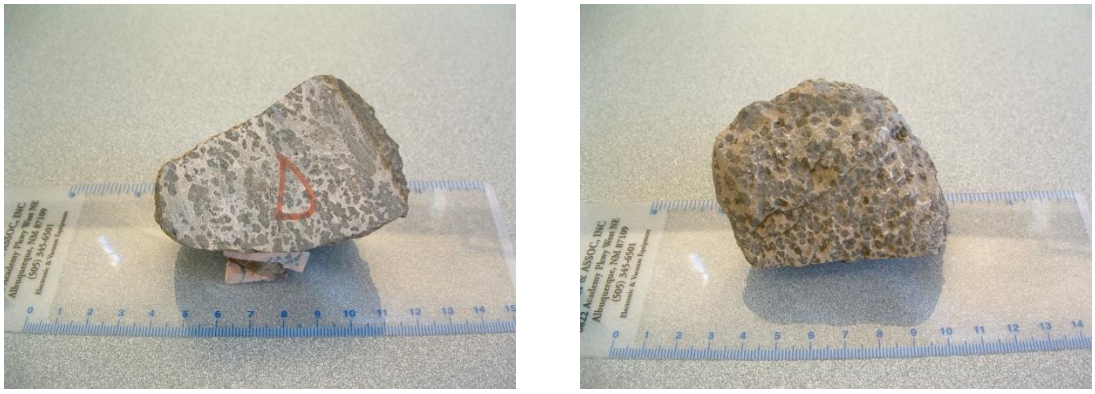

Figure A-2: SEPGD rock sample.

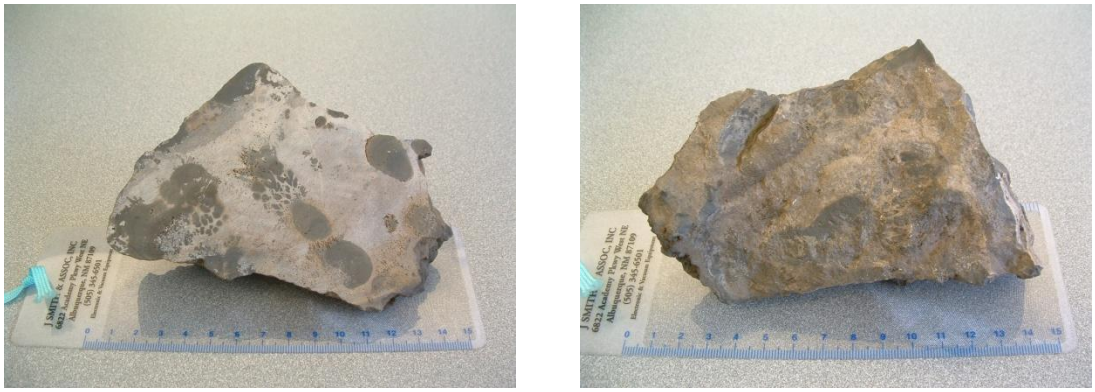

Figure A-3: SEPGE rock sample.

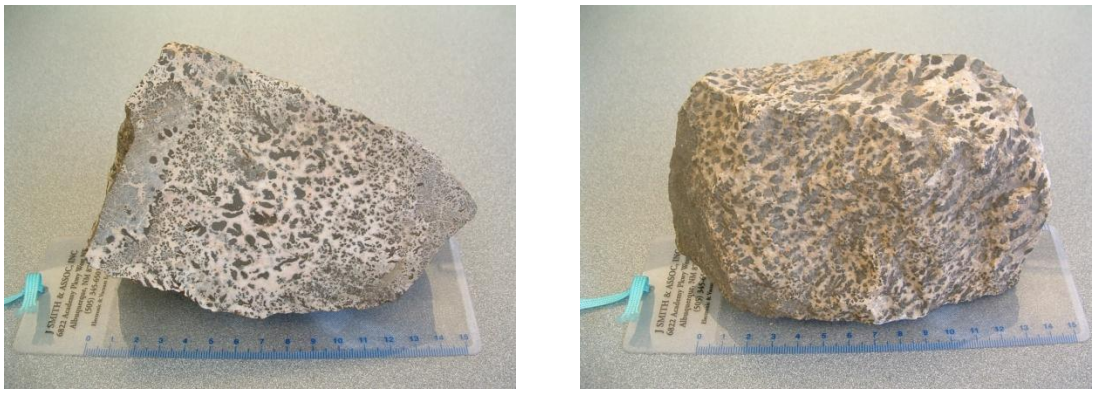

Figure A-4: SE-bulk rock sample.

Luis Lopez

Figure A-5: MCA-1 rock sample.

Figure A-6: MCA-2 rock sample.

Figure A-7: MCA-3 rock sample.

Figure A-8: MCA-4 rock sample.

Figure A-9: MCA-5 rock sample.

Figure A-10: MCA-6 rock sample.

Figure A-11: MCA-7 rock sample.

Figure A-12: Nogal-1 rock sample.

Figure A-13: Nogal-2 rock sample.

Figure A-14: PG-1 rock sample.

Figure A-15: PG-2 rock sample.

Figure A-16: BC-1 rock sample.

Figure A-17: BC-2 rock sample.

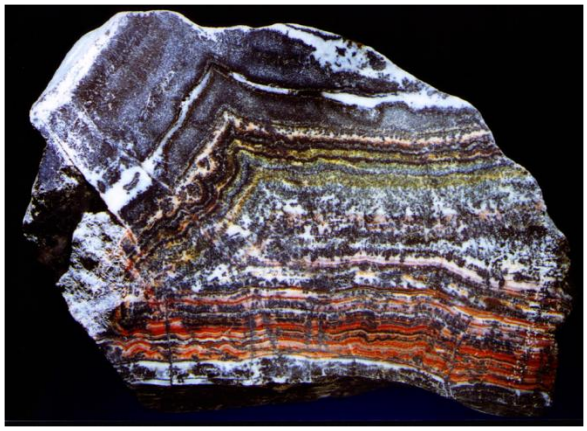

Figure A-18: Nancy #9189 rock sample, 15.5cm (6 in) across.

Water Canyon

Figure A-19: 003301 rock sample.

Figure A-20: 003303 rock sample.

Figure A-21: 003304 rock sample.

Figure A-22: 003304A rock sample.

Figure A-23: 003304B rock sample.

Figure A-24: 003308 rock sample.

APPENDIX B. ELECTRON MICROPROBE ANALYSES

Table B-1: Microprobe data for SE-PKM-1, SE-PGD, SE-PGE-1, SE-PGE-2, SE-bulk-1, SE-bulk-2, and SE-bulk-3.

Comment	SiO2	SO2	MgO	CaO	MnO	FeO	ZnO	BaO	PbO	Na2O	K2O	Ag2O	Total	Mineral
sepkm-01	2.12	0.00	0.00	0.46	2.04	77.70	0.64	0.00	1.26	0.03	0.01	0.00	84.26	Fe phase
sepkm-02	3.55	0.03	0.00	0.50	1.70	73.74	0.43	0.00	1.00	0.03	0.01	0.00	80.99	Fe phase
sepkm-03	3.35	0.00	0.00	0.43	1.67	78.81	0.53	0.00	0.94	0.05	0.00	0.03	85.81	Fe phase
sepkm-04	2.49	0.01	0.00	0.47	2.24	77.53	0.55	0.08	1.47	0.04	0.02	0.00	84.91	Fe phase
sepkm-05	0.15	0.09	0.14	2.72	70.03	0.66	0.50	0.06	0.03	1.20	3.32	0.00	78.90	cryptomelane
sepkm-06	0.00	0.03	0.28	2.81	71.31	1.32	0.58	0.06	0.09	1.16	2.23	0.00	79.87	low K cryptomelane
sepkm-07	0.00	0.06	0.87	3.84	64.70	1.00	1.28	0.02	0.48	0.92	0.62	0.00	73.80	birnessite
sepkm-08	0.00	0.03	0.72	3.21	65.48	0.55	0.85	0.02	0.02	0.78	1.16	0.00	72.82	birnessite
sepkm-09	0.00	0.03	0.09	2.35	75.70	0.67	0.44	0.01	0.00	1.02	4.30	0.00	84.61	cryptomelane
sepkm-010	0.00	0.05	0.34	2.67	71.27	0.95	0.62	0.03	0.31	1.10	2.68	0.00	80.01	low K cryptomelane
sepkm-011	0.00	0.01	1.31	3.36	65.12	1.09	1.29	0.05	0.02	1.05	0.58	0.00	73.87	birnessite
sepkm-012	0.00	0.03	0.84	3.34	68.50	0.90	0.91	0.04	0.14	1.02	1.02	0.00	76.72	birnessite
sepkm-013	0.00	0.05	0.26	3.24	69.46	0.57	0.70	0.16	0.00	1.12	2.01	0.00	77.56	cryptomelane
sepkm-014	0.00	0.02	1.28	3.28	67.11	1.34	1.33	0.04	0.20	1.10	0.54	0.00	76.24	birnessite
sepkm-015	0.00	0.01	0.67	3.58	67.56	0.93	0.92	0.12	0.24	1.02	1.07	0.00	76.10	birnessite
sepkm-016	0.00	0.00	0.02	1.79	72.38	2.46	0.17	0.09	0.19	0.88	4.85	0.00	82.83	cryptomelane
sepkm-017	0.00	0.03	0.03	2.22	70.69	1.78	0.30	0.08	0.16	0.82	4.84	0.00	80.96	cryptomelane
sepkm-018	0.00	0.03	0.64	3.98	69.20	0.97	0.84	0.06	0.11	1.09	1.24	0.00	78.15	birnessite
sepkm-019	1.84	0.02	0.00	0.48	3.92	74.65	0.77	0.01	2.06	0.04	0.01	0.00	83.80	Fe phase
sepkm-020	1.88	0.01	0.00	0.48	3.57	76.46	0.53	0.13	1.84	0.04	0.01	0.00	84.95	Fe phase
sepkm-021	3.30	0.00	0.00	0.50	3.07	76.26	0.47	0.00	1.39	0.06	0.02	0.00	85.06	Fe phase
sepkm-022	0.12	0.00	0.02	0.08	79.46	0.12	0.51	0.03	0.07	0.01	0.00	0.00	80.42	birnessite
sepkm-023	0.16	0.01	0.00	0.01	76.13	0.16	0.77	0.00	0.00	0.00	0.00	0.00	77.23	birnessite
sepkm-024	0.04	0.01	0.00	0.05	94.50	0.20	1.06	0.00	0.00	0.03	0.00	0.00	95.90	high Mn phase
sepkm-025	0.07	0.00	0.00	0.41	53.70	0.84	0.26	0.02	29.81	0.00	0.00	0.00	85.12	coronadite
sepkm-026	0.09	0.01	0.00	0.17	52.54	1.30	0.85	0.02	31.12	0.02	0.03	0.00	86.14	coronadite
sepkm-027	2.17	0.00	0.00	0.58	4.38	75.37	0.77	0.00	1.85	0.04	0.01	0.00	85.17	Fe phase
sepkm-028	1.66	0.00	0.00	0.49	3.78	76.31	0.58	0.05	1.57	0.05	0.03	0.00	84.51	Fe phase
sepkm-029	3.62	0.00	0.00	0.56	3.35	73.63	0.63	0.03	0.96	0.03	0.04	0.00	82.84	Fe phase
sepkm-030	3.00	0.02	0.00	0.80	3.29	73.28	0.61	0.12	0.91	0.04	0.02	0.00	82.07	Fe phase
sepkm-031	0.15	0.02	0.02	0.24	75.75	0.80	0.71	0.02	0.04	0.07	0.00	0.00	77.80	birnessite
sepkm-032	0.00	0.02	0.00	0.13	76.56	1.05	0.75	0.08	0.09	0.02	0.00	0.00	78.71	birnessite
sepkm-033	0.11	0.00	0.00	0.61	53.39	0.17	0.53	0.02	28.42	0.00	0.00	0.00	83.25	coronadite
sepkm-034	0.00	0.00	0.00	0.16	69.92	1.87	0.49	0.03	35.90	0.02	0.00	0.00	108.39	coronadite, mixed phase
sepkm-035	2.30	0.00	0.00	0.47	3.27	77.11	0.65	0.03	1.52	0.02	0.02	0.00	85.40	Fe phase
sepkm-036	2.04	0.01	0.00	0.49	3.62	76.46	0.68	0.04	1.51	0.06	0.03	0.00	84.92	Fe phase
sepkm-037	3.55	0.00	0.00	0.53	3.11	74.83	0.58	0.00	1.04	0.04	0.03	0.00	83.71	Fe phase

sepkm-038	3.96	0.03	0.00	0.41	3.34	72.61	0.71	0.01	1.00	0.06	0.04	0.00	82.16	Fe phase
sepkm-039	0.00	0.01	0.07	2.98	67.76	1.06	0.45	0.00	0.70	1.15	1.72	0.00	75.90	birnessite
sepkm-040	0.18	0.01	0.00	1.31	69.91	1.85	0.55	0.07	0.51	0.74	3.94	0.00	79.08	cryptomelane
sepkm-041	0.00	0.04	0.84	4.36	67.08	0.51	1.10	0.06	0.04	1.02	0.79	0.00	75.85	birnessite
sepkm-042	0.00	0.02	0.94	4.11	65.75	0.58	1.24	0.00	0.10	0.94	0.65	0.00	74.31	birnessite
sepkm-043	0.00	0.05	0.67	4.12	64.96	0.51	1.01	0.00	0.09	0.94	0.81	0.00	73.16	birnessite
sepgd-01	1.67	0.01	0.00	0.90	1.33	77.58	0.69	0.08	0.88	0.01	0.02	0.00	83.16	Fe phase
sepgd-02	0.10	0.13	0.94	7.04	58.74	1.39	0.01	0.00	0.18	0.14	0.70	0.00	69.36	todorokite
sepgd-03	0.01	0.02	1.06	5.57	65.88	0.64	0.02	0.01	0.05	0.08	0.70	0.00	74.03	todorokite
sepgd-04	0.00	0.02	1.01	5.76	64.18	0.60	0.02	0.04	0.05	0.07	0.71	0.00	72.45	todorokite
sepgd-05	0.20	0.04	0.90	5.57	61.19	6.10	0.12	0.00	0.20	0.06	0.54	0.00	74.92	todorokite
sepgd-06	0.00	0.04	1.14	6.05	64.21	0.27	0.05	0.04	0.23	0.10	0.57	0.00	72.70	todorokite
sepgd-07	0.01	0.06	1.01	5.79	64.67	1.35	0.00	0.06	0.12	0.06	0.59	0.00	73.72	todorokite
sepgd-08	0.38	0.06	1.14	6.26	66.89	0.17	0.03	0.00	0.06	0.12	0.63	0.00	75.72	todorokite
sepgd-09	0.00	0.03	1.09	5.89	64.69	0.84	0.00	0.00	0.09	0.09	0.52	0.00	73.23	todorokite
sepgd-010	0.00	0.14	1.07	6.28	62.50	0.61	0.03	0.04	0.09	0.55	0.57	0.00	71.88	todorokite
sepgd-011	0.12	0.02	1.23	5.71	66.54	0.27	0.02	0.00	0.08	0.12	0.74	0.00	74.84	todorokite
sepgd-012	0.00	0.02	1.09	5.74	64.10	0.32	0.03	0.00	0.07	0.09	0.71	0.00	72.17	todorokite
sepgd-013	0.03	0.06	0.99	5.26	66.02	0.41	0.02	0.00	0.00	0.15	0.62	0.00	73.56	todorokite
sepgd-014	0.26	0.03	0.90	5.67	64.26	0.38	0.05	0.01	0.00	0.13	0.62	0.00	72.29	todorokite
sepgd-015	1.93	0.01	0.00	1.38	1.90	75.26	0.82	0.00	0.92	0.04	0.02	0.00	82.27	Fe phase
sepge-1-01	1.63	0.07	0.00	0.76	3.52	67.72	0.80	0.02	1.23	0.04	0.03	0.00	75.82	Fe phase
sepge-1-02	1.82	0.04	0.00	1.04	5.64	70.05	0.79	0.00	1.31	0.02	0.02	0.00	80.73	Fe phase
sepge-1-03	0.00	0.01	0.83	5.86	65.98	0.21	0.22	0.00	0.22	0.17	0.59	0.00	74.09	todorokite
sepge-1-04	0.21	0.04	0.85	5.36	66.30	0.17	0.36	0.01	0.23	0.14	0.57	0.00	74.22	todorokite
sepge-1-05	0.00	0.05	0.63	5.67	63.71	0.29	0.12	0.00	0.15	0.13	0.61	0.00	71.35	todorokite
sepge-1-06	0.00	0.05	0.71	5.24	67.18	0.35	0.17	0.12	0.03	0.12	0.58	0.00	74.54	todorokite
sepge-1-07	1.28	0.01	0.00	0.68	3.69	69.77	0.70	0.00	1.42	0.05	0.03	0.01	77.63	Fe phase
sepge-1-08	0.00	0.06	0.89	5.02	65.79	0.40	0.32	0.00	0.08	0.09	0.58	0.00	73.23	todorokite
sepge-1-09	0.00	0.03	0.80	5.08	61.43	0.62	0.20	0.00	0.14	0.12	0.60	0.00	69.01	todorokite
sepge-1-010	0.00	0.02	0.79	4.90	64.72	0.17	0.23	0.06	0.07	0.11	0.58	0.00	71.64	todorokite
sepge-1-011	1.17	0.03	0.00	0.72	5.60	65.41	0.80	0.00	1.22	0.07	0.06	0.00	75.09	Fe phase
sepge-1-012	0.06	0.07	0.85	4.57	64.19	2.74	0.13	0.00	0.21	0.12	0.68	0.00	73.61	todorokite
sepge-1-013	0.00	0.04	0.82	4.84	60.54	0.91	0.22	0.00	0.28	0.09	0.60	0.00	68.34	todorokite
sepge-1-014	0.00	0.01	0.80	4.60	62.19	0.25	0.17	0.04	0.15	0.08	0.71	0.00	68.99	todorokite
sepge-1-015	0.00	0.03	0.77	4.93	62.92	0.21	0.16	0.00	0.00	0.13	0.65	0.00	69.80	todorokite
sepge-1-016	1.20	0.02	0.00	2.04	9.03	59.91	0.99	0.11	1.98	0.08	0.07	0.00	75.44	Fe phase, mixed phase
sepge-1-017	0.08	0.01	0.81	6.18	62.99	0.16	0.26	0.13	0.29	0.13	0.59	0.00	71.61	todorokite
sepge-1-018	0.00	0.02	0.83	5.68	63.63	0.17	0.39	0.06	0.04	0.10	0.57	0.00	71.48	todorokite
sepge-1-019	1.52	0.03	0.00	1.41	1.42	73.18	1.01	0.01	1.81	0.07	0.03	0.00	80.48	Fe phase
sepge-1-020	0.07	0.04	1.24	7.61	65.20	0.11	0.11	0.00	0.02	0.16	0.61	0.00	75.17	todorokite
sepge-1-021	0.00	0.02	0.87	7.09	65.02	0.17	0.19	0.05	0.08	0.15	0.64	0.00	74.28	todorokite

sepge-1-022	0.00	0.05	1.19	5.61	69.03	0.57	0.14	0.00	0.02	0.09	1.13	0.00	77.83	todorokite
sepge-1-023	0.00	0.07	1.07	6.23	68.44	0.72	0.15	0.06	0.05	0.11	1.20	0.00	78.09	todorokite
sepge-2-01	0.01	0.02	1.19	6.19	69.66	1.19	0.11	0.04	0.04	0.14	0.72	0.00	79.29	todorokite
sepge-2-02	0.19	0.02	1.03	5.74	61.37	5.10	0.16	0.00	0.08	0.17	0.64	0.00	74.49	todorokite
sepge-2-03	2.36	0.02	0.00	1.33	1.69	73.40	1.21	0.00	2.07	0.00	0.02	0.00	82.11	Fe phase
sepge-2-04	0.00	0.03	0.73	6.71	64.65	0.17	0.21	0.08	0.00	0.19	0.51	0.00	73.28	todorokite
sepge-2-05	0.00	0.00	0.66	6.16	64.48	0.86	0.13	0.03	0.00	0.11	0.47	0.00	72.90	todorokite
sepge-2-06	2.06	0.02	0.00	0.98	2.55	73.37	0.73	0.00	1.12	0.04	0.03	0.00	80.90	Fe phase
sepge-2-07	2.45	0.02	0.00	1.03	3.19	74.16	0.38	0.00	0.80	0.01	0.01	0.00	82.04	Fe phase
sepge-2-08	1.40	0.03	0.00	0.74	4.66	72.26	1.20	0.04	1.82	0.06	0.12	0.00	82.34	Fe phase
sepge-2-09	1.44	0.06	0.00	0.78	4.56	72.65	1.32	0.07	2.02	0.06	0.14	0.00	83.10	Fe phase
sepge-2-010	0.20	0.07	0.43	1.58	70.80	0.40	0.93	0.00	0.05	0.57	3.96	0.00	78.99	cryptomelane
sepge-2-011	0.00	0.04	0.18	1.84	73.09	0.33	0.40	0.01	0.13	0.57	4.25	0.00	80.82	cryptomelane
sepge-2-012	0.06	0.07	0.46	2.22	70.54	0.82	0.76	0.00	0.24	0.51	3.52	0.00	79.22	cryptomelane
sepge-2-013	0.01	0.06	0.97	1.87	72.06	0.58	1.44	0.00	0.07	0.48	3.62	0.00	81.15	cryptomelane
sepge-2-014	0.00	0.07	0.73	2.43	64.90	2.36	1.13	0.00	0.23	0.41	2.99	0.00	75.25	cryptomelane
sepge-2-015	0.00	0.07	0.12	2.04	73.66	0.32	0.21	0.11	0.00	0.58	4.16	0.00	81.29	cryptomelane
sepge-2-016	0.00	0.07	0.12	2.31	70.87	0.19	0.21	0.07	0.03	0.56	4.19	0.00	78.61	cryptomelane
sepge-2-017	0.36	0.07	0.19	1.88	67.12	0.65	0.21	0.05	0.14	0.45	3.78	0.00	74.92	cryptomelane
sepge-2-018	0.07	0.04	0.14	1.90	64.23	0.41	0.16	0.02	0.04	0.47	3.90	0.00	71.39	cryptomelane
sepge-2-019	0.00	0.11	1.03	6.38	68.03	0.31	0.08	0.02	0.09	0.24	0.71	0.00	77.01	todorokite
sepge-2-020	0.00	0.03	1.00	6.15	63.08	0.21	0.22	0.01	0.00	0.21	0.62	0.00	71.53	todorokite
sepge-2-021	0.03	0.12	0.29	1.84	70.97	0.42	0.20	0.04	0.00	0.55	4.19	0.00	78.63	cryptomelane
sepge-2-022	0.00	0.06	0.24	2.94	69.63	0.10	0.17	0.00	0.06	0.60	3.33	0.00	77.14	cryptomelane
sepge-2-023	0.00	0.12	0.18	1.90	70.41	0.32	0.26	0.11	0.00	0.60	4.00	0.00	77.90	cryptomelane
sebulk-1-01	0.56	0.00	0.01	1.15	44.24	10.47	1.04	0.14	24.22	0.06	0.04	0.00	81.92	coronadite
sebulk-1-02	0.24	0.00	0.05	1.04	50.93	3.97	1.31	0.00	25.81	0.08	0.03	0.00	83.44	coronadite
sebulk-1-03	3.87	0.03	0.07	0.76	0.12	70.16	0.88	0.11	0.72	0.06	0.01	0.00	76.77	Fe phase
sebulk-1-04	3.93	0.04	0.07	0.52	0.00	73.87	0.82	0.02	0.66	0.04	0.03	0.00	80.00	Fe phase
sebulk-1-05	4.15	0.00	0.09	0.47	0.00	78.01	0.97	0.00	0.79	0.03	0.01	0.01	84.54	Fe phase
sebulk-1-06	4.35	0.01	0.08	0.50	0.03	76.21	0.79	0.02	0.81	0.02	0.01	0.05	82.86	Fe phase
sebulk-1-07	2.57	0.06	0.00	0.79	0.11	81.83	0.30	0.05	0.11	0.07	0.03	0.00	85.92	Fe phase
sebulk-1-08	4.29	0.06	0.10	0.57	0.04	72.81	0.90	0.00	0.75	0.08	0.23	0.03	79.85	Fe phase
sebulk-1-09	3.11	0.06	0.02	0.49	0.00	75.32	1.29	0.01	0.38	0.02	0.00	0.00	80.70	Fe phase
sebulk-1-010	2.99	0.05	0.05	0.53	0.06	73.54	1.26	0.00	0.14	0.04	0.00	0.01	78.65	Fe phase
sebulk-1-011	0.16	0.00	0.04	1.17	48.52	2.34	1.71	0.00	28.56	0.10	0.07	0.00	82.65	coronadite
sebulk-1-012	3.49	0.02	0.00	0.78	0.09	78.07	0.66	0.00	0.33	0.02	0.00	0.00	83.47	Fe phase
sebulk-1-013	2.12	0.03	0.00	0.80	0.05	81.92	0.26	0.07	0.08	0.04	0.00	0.01	85.38	Fe phase
sebulk-1-014	4.52	0.00	0.09	0.39	0.01	73.62	1.25	0.03	0.78	0.05	0.00	0.03	80.77	Fe phase
sebulk-1-015	1.80	0.45	0.29	1.88	0.33	80.08	0.79	0.02	0.00	0.33	0.02	0.00	85.97	Fe phase
sebulk-1-016	0.00	0.00	2.24	3.10	67.32	0.20	0.73	0.00	0.02	0.63	0.84	0.00	75.09	todorokite
sebulk-1-017	0.01	0.02	2.17	3.74	67.25	0.21	0.77	0.00	0.00	0.70	0.82	0.00	75.67	todorokite

sebulk-1-018	0.02	0.04	2.25	3.32	69.01	0.29	0.68	0.13	0.00	0.65	0.82	0.00	77.21	todorokite
sebulk-1-019	0.04	0.04	2.32	3.25	64.81	0.38	0.70	0.04	0.06	0.69	0.85	0.00	73.18	todorokite
sebulk-1-020	0.00	0.04	2.33	3.10	64.67	0.39	0.64	0.02	0.02	0.69	0.82	0.00	72.72	todorokite
sebulk-1-021	0.00	0.02	2.23	3.70	63.85	0.28	0.80	0.04	0.02	0.71	0.84	0.00	72.48	todorokite
sebulk-1-022	3.82	0.04	0.09	0.43	0.02	72.37	1.70	0.14	0.14	0.05	0.00	0.01	78.80	Fe phase
sebulk-1-023	3.52	0.03	0.00	0.73	0.07	79.43	0.37	0.00	0.79	0.03	0.02	0.00	85.00	Fe phase
sebulk-1-024	3.67	0.02	0.04	0.46	0.02	74.49	1.07	0.05	0.48	0.03	0.02	0.00	80.35	Fe phase
sebulk-1-025	2.68	0.06	0.00	0.53	0.00	72.79	1.99	0.00	0.69	0.04	0.00	0.03	78.82	Fe phase
sebulk-1-026	0.00	0.02	2.27	2.98	65.93	0.22	0.70	0.07	0.00	0.59	0.88	0.00	73.65	todorokite
sebulk-1-027	0.00	0.02	2.26	3.23	65.08	0.30	0.79	0.00	0.00	0.63	0.82	0.00	73.13	todorokite
sebulk-1-028	0.00	0.06	2.24	3.28	65.20	0.38	0.77	0.03	0.00	0.61	0.82	0.00	73.39	todorokite
sebulk-1-029	0.00	0.00	2.28	3.17	64.40	0.54	0.70	0.06	0.01	0.63	0.83	0.00	72.61	todorokite
sebulk-1-030	0.01	0.01	2.26	2.99	65.84	0.42	0.76	0.00	0.09	0.58	0.82	0.00	73.79	todorokite
sebulk-1-031	2.34	0.00	0.02	0.80	54.45	0.42	0.61	0.00	25.21	0.04	0.01	0.00	83.89	coronadite
sebulk-1-032	4.06	0.02	0.33	1.19	3.86	67.31	0.66	0.02	0.03	0.06	0.07	0.00	77.61	Fe phase
sebulk-1-033	0.15	0.02	0.00	85.08	0.75	0.04	0.07	0.00	0.00	0.01	0.01	0.04	86.16	calcite
sebulk-1-034	0.00	0.02	2.22	3.70	65.82	1.53	0.77	0.08	0.02	0.82	0.87	0.00	75.84	todorokite
sebulk-1-035	0.00	0.00	2.21	3.44	65.75	0.73	0.81	0.00	0.05	0.89	0.86	0.00	74.74	todorokite
sebulk-1-036	0.00	0.03	2.35	3.34	66.85	0.31	0.98	0.07	0.00	0.81	0.81	0.00	75.54	todorokite
sebulk-1-037	0.00	0.01	2.31	4.13	66.96	0.57	0.91	0.00	0.07	0.93	0.96	0.00	76.85	todorokite
sebulk-2-01	0.00	0.00	0.01	0.47	61.66	0.93	0.36	0.04	20.23	0.14	0.45	0.00	84.30	coronadite
sebulk-2-02	0.22	0.00	0.12	1.03	51.01	3.56	0.74	0.00	24.79	0.07	0.09	0.00	81.62	coronadite
sebulk-2-03	0.08	0.01	2.16	2.97	63.22	3.52	0.66	0.02	0.90	0.57	0.79	0.00	74.89	todorokite
sebulk-2-04	0.00	0.01	2.12	3.13	64.31	0.54	0.78	0.00	1.11	0.58	0.86	0.00	73.43	todorokite
sebulk-2-05	0.02	0.05	2.68	3.38	63.85	0.38	0.65	0.05	0.47	2.66	0.91	0.00	75.11	todorokite
sebulk-2-06	0.00	0.03	1.39	3.51	59.44	1.30	0.59	0.02	2.94	0.42	0.73	0.00	70.37	todorokite
sebulk-2-07	1.47	0.03	0.04	0.99	33.48	25.45	0.87	0.01	15.72	0.03	0.00	0.00	78.09	mixed phase
sebulk-2-08	0.05	0.01	0.36	1.50	56.32	2.27	0.66	0.05	17.52	0.13	0.59	0.00	79.46	coronadite
sebulk-2-09	0.00	0.01	2.34	3.25	65.35	0.74	0.78	0.00	0.35	0.62	0.85	0.00	74.27	todorokite
sebulk-2-010	0.24	0.02	1.95	3.23	58.22	3.57	0.70	0.04	0.53	0.50	0.77	0.00	69.77	todorokite
sebulk-2-011	0.03	0.01	2.19	3.22	64.73	2.12	0.81	0.00	1.04	0.56	0.85	0.00	75.54	todorokite
sebulk-2-012	0.00	0.02	2.26	3.53	67.80	0.85	0.86	0.13	0.52	0.59	0.89	0.00	77.44	todorokite
sebulk-2-013	0.00	0.01	2.47	3.43	64.99	0.33	0.68	0.07	0.20	0.60	0.85	0.00	73.62	todorokite
sebulk-2-014	0.19	0.01	0.03	0.84	50.86	3.60	0.60	0.00	26.11	0.08	0.03	0.00	82.35	coronadite
sebulk-2-015	0.14	0.00	0.07	0.93	54.89	3.52	0.62	0.12	23.56	0.09	0.08	0.00	84.02	coronadite
sebulk-2-016	0.30	0.00	0.03	0.91	48.99	4.86	0.59	0.04	26.92	0.06	0.01	0.00	82.70	coronadite
sebulk-2-017	0.00	0.00	2.25	3.03	67.32	0.26	0.66	0.03	0.31	0.71	0.88	0.00	75.44	todorokite
sebulk-2-018	0.00	0.02	2.14	3.31	62.18	0.79	0.76	0.07	0.89	0.64	0.83	0.00	71.62	todorokite
sebulk-2-019	0.00	0.00	2.45	2.95	67.24	0.33	0.62	0.00	0.28	0.75	0.87	0.00	75.48	todorokite
sebulk-2-020	0.48	0.00	0.63	2.30	48.01	4.66	0.49	0.00	9.28	0.26	0.42	0.00	66.52	coronadite, mixed phase
sebulk-2-021	1.99	0.06	0.05	0.53	0.00	80.68	0.27	0.00	0.86	0.03	0.00	0.00	84.46	Fe phase
sebulk-2-022	3.81	0.02	0.00	0.66	0.04	80.78	0.15	0.01	0.43	0.02	0.00	0.05	85.97	Fe phase

sebulk-2-023	4.57	0.02	0.17	0.35	0.00	72.62	0.72	0.04	0.43	0.02	0.01	0.00	78.96	Fe phase
sebulk-2-024	2.13	0.02	0.32	0.28	0.05	77.85	0.19	0.02	0.01	0.00	0.00	0.13	80.99	Fe phase
sebulk-2-025	3.87	0.07	0.05	0.63	0.00	71.28	1.30	0.10	0.41	0.07	0.00	0.00	77.78	Fe phase
sebulk-2-026	1.50	0.03	0.40	0.30	0.00	79.62	0.13	0.00	0.00	0.01	0.00	0.09	82.08	Fe phase
sebulk-2-027	2.49	0.02	0.40	0.16	0.00	77.17	0.13	0.07	0.20	0.03	0.00	0.01	80.68	Fe phase
sebulk-2-028	3.80	0.00	0.16	1.06	0.07	71.73	1.14	0.01	0.17	0.04	0.00	0.07	78.23	Fe phase
sebulk-2-029	0.05	0.01	2.39	3.01	67.42	0.40	0.70	0.03	0.09	0.63	0.93	0.00	75.66	todorokite
sebulk-2-030	0.11	0.03	2.10	3.54	64.21	1.73	0.71	0.05	0.14	0.65	0.85	0.00	74.11	todorokite
sebulk-2-031	0.00	0.00	2.43	2.96	65.48	0.38	0.70	0.00	0.03	0.62	0.83	0.00	73.42	todorokite
sebulk-2-032	0.00	0.06	1.62	4.18	62.05	2.13	0.75	0.00	0.50	0.49	0.73	0.00	72.51	todorokite
sebulk-2-033	0.00	0.02	2.29	3.19	66.96	0.38	0.71	0.00	0.52	0.57	0.86	0.00	75.51	todorokite
sebulk-2-034	0.00	0.02	2.37	3.04	63.95	0.23	0.82	0.00	0.18	0.61	0.83	0.00	72.04	todorokite
sebulk-2-035	0.00	0.03	1.84	3.76	65.23	1.97	0.69	0.02	0.24	0.51	0.80	0.00	75.10	todorokite
sebulk-2-036	0.00	0.02	2.30	3.23	64.86	0.33	0.70	0.02	0.20	0.66	0.90	0.00	73.21	todorokite
sebulk-3-01	0.43	0.01	0.27	1.51	54.79	3.56	0.71	0.23	20.75	0.14	0.20	0.00	82.60	coronadite
sebulk-3-02	0.27	0.00	0.04	0.46	60.05	0.54	0.52	0.11	24.08	0.10	0.35	0.00	86.51	coronadite
sebulk-3-03	0.03	0.00	0.08	1.28	57.51	1.82	0.55	0.00	19.36	0.15	0.27	0.00	81.04	coronadite
sebulk-3-04	0.00	0.05	0.31	2.62	57.34	3.82	0.66	0.02	13.00	0.25	0.44	0.00	78.50	coronadite
sebulk-3-05	0.00	0.02	1.01	1.67	60.68	0.39	10.71	0.00	0.45	0.38	0.24	0.00	75.56	chalcophanite
sebulk-3-06	0.00	0.06	1.86	3.31	64.93	2.22	0.67	0.04	1.32	0.51	0.77	0.00	75.67	todorokite
sebulk-3-07	0.00	0.03	2.12	3.07	63.56	0.92	0.67	0.02	1.04	0.52	0.82	0.00	72.76	todorokite
sebulk-3-08	0.00	0.02	2.21	3.38	66.04	0.82	0.67	0.05	0.49	0.63	0.82	0.00	75.13	todorokite
sebulk-3-09	0.00	0.03	2.18	3.33	63.32	1.28	0.73	0.00	0.50	0.62	0.85	0.00	72.84	todorokite
sebulk-3-010	1.03	0.10	1.02	2.54	48.48	20.13	0.49	0.03	1.18	0.36	0.42	0.00	75.76	mixed phase
sebulk-3-011	0.22	0.04	2.30	3.33	64.07	0.26	0.67	0.00	0.62	0.57	0.82	0.00	72.90	todorokite
sebulk-3-012	0.00	0.03	2.31	3.16	67.44	0.33	0.69	0.00	0.54	0.65	0.84	0.00	75.99	todorokite
sebulk-3-013	0.15	0.00	0.02	1.14	56.13	1.26	0.49	0.00	22.50	0.03	0.25	0.00	81.97	coronadite
sebulk-3-014	0.00	0.03	2.30	3.02	66.31	0.28	0.66	0.00	0.62	0.65	0.89	0.00	74.76	todorokite
sebulk-3-015	0.00	0.02	2.31	3.24	63.19	0.36	0.69	0.00	0.44	0.66	0.85	0.00	71.76	todorokite
sebulk-3-016	0.00	0.11	1.69	3.97	63.44	1.62	0.62	0.00	1.00	0.59	0.75	0.00	73.79	todorokite
sebulk-3-017	0.00	0.04	2.23	3.11	63.15	0.63	0.62	0.09	0.71	0.62	0.83	0.00	72.03	todorokite
sebulk-3-018	0.17	0.04	2.16	3.02	64.59	0.28	0.71	0.08	0.82	0.56	0.81	0.00	73.25	todorokite
sebulk-3-019	0.00	0.08	1.84	4.40	65.08	1.62	0.67	0.03	0.84	0.67	0.82	0.00	76.06	todorokite
sebulk-3-020	0.03	0.19	1.58	4.09	65.29	4.68	0.56	0.01	0.94	0.59	0.71	0.00	78.67	todorokite
sebulk-3-021	0.00	0.03	2.45	3.35	65.53	0.37	0.66	0.04	0.62	0.68	0.84	0.00	74.58	todorokite
sebulk-3-022	0.00	0.02	2.26	3.25	67.09	0.35	0.64	0.00	0.40	0.70	0.83	0.00	75.53	todorokite
sebulk-3-023	0.00	0.04	2.19	3.26	65.61	0.66	0.87	0.02	0.97	0.74	0.91	0.00	75.26	todorokite
sebulk-3-024	0.03	0.05	1.79	2.31	64.50	0.68	3.24	0.00	0.43	0.56	0.51	0.00	74.08	todorokite
sebulk-3-025	0.00	0.06	2.39	3.36	64.05	0.42	0.66	0.09	0.04	0.76	0.87	0.00	72.69	todorokite
sebulk-3-026	0.00	0.02	2.24	3.22	66.39	0.71	0.74	0.05	0.08	0.68	0.86	0.00	74.99	todorokite
sebulk-3-027	0.00	0.02	2.29	3.17	65.04	0.48	0.71	0.00	0.06	0.71	0.86	0.00	73.34	todorokite
sebulk-3-028	0.00	0.02	2.13	3.07	64.43	0.72	0.77	0.11	1.18	0.77	0.85	0.00	74.04	todorokite

sebulk-3-029	0.00	0.16	2.37	3.36	63.04	0.59	0.82	0.00	0.32	0.78	0.84	0.00	72.26	todorokite
sebulk-3-030	1.36	0.13	2.16	3.50	64.55	1.42	0.73	0.12	0.26	1.01	0.83	0.00	76.08	todorokite
sebulk-3-031	0.06	0.11	2.27	2.99	63.99	0.43	0.77	0.06	0.13	0.83	0.86	0.00	72.49	todorokite
sebulk-3-032	0.00	0.07	2.34	3.28	65.31	0.31	0.65	0.08	0.11	0.92	0.87	0.00	73.94	todorokite
sebulk-3-033	0.00	0.08	2.21	3.18	63.93	0.46	0.81	0.00	0.22	0.78	0.86	0.00	72.52	todorokite
sebulk-3-034	0.22	0.07	1.90	3.06	60.28	5.57	0.73	0.05	0.45	0.71	0.74	0.00	73.79	todorokite
sebulk-3-035	0.00	0.01	2.38	3.08	64.51	0.39	0.75	0.00	0.00	0.68	0.91	0.00	72.70	todorokite
sebulk-3-036	0.00	0.01	2.34	2.95	66.93	0.38	0.68	0.03	0.03	0.63	0.83	0.00	74.80	todorokite
sebulk-3-037	0.00	0.05	2.17	3.36	62.70	1.03	0.73	0.00	0.08	0.67	0.82	0.00	71.59	todorokite
sebulk-3-038	0.43	0.11	0.06	0.74	59.32	1.32	0.54	0.00	22.70	0.10	0.29	0.00	85.60	coronadite
sebulk-3-039	0.17	0.01	0.00	0.57	54.29	0.41	0.48	0.04	25.50	0.05	0.13	0.00	81.64	coronadite
sebulk-3-040	0.17	0.02	0.03	0.51	58.60	0.72	0.29	0.07	24.09	0.07	0.16	0.00	84.71	coronadite
sebulk-3-041	0.14	0.00	0.05	0.55	55.08	0.43	0.41	0.01	23.66	0.06	0.23	0.00	80.62	coronadite
sebulk-3-042	0.14	0.02	0.01	1.08	52.08	0.85	0.34	0.14	17.47	0.10	0.63	0.00	72.86	coronadite
sebulk-3-043	0.02	0.03	2.35	3.19	66.35	0.33	0.82	0.00	0.66	0.72	0.81	0.00	75.27	todorokite
sebulk-3-044	0.00	0.02	2.20	2.76	64.18	0.59	0.60	0.00	0.96	0.77	0.78	0.00	72.86	todorokite
sebulk-3-045	0.08	0.05	2.30	3.14	65.67	0.36	0.68	0.05	1.00	0.77	0.85	0.00	74.94	todorokite
sebulk-3-046	0.00	0.03	2.39	3.00	66.35	0.73	0.74	0.12	0.11	1.00	0.97	0.00	75.43	todorokite
sebulk-3-047	0.06	0.03	2.39	3.09	64.29	0.80	0.66	0.00	0.00	0.97	0.95	0.00	73.23	todorokite
sebulk-3-048	0.04	0.05	2.28	3.21	67.20	0.60	0.63	0.00	0.12	0.97	0.95	0.00	76.05	todorokite
sebulk-3-049	0.00	0.01	2.53	2.33	61.01	0.59	1.57	0.02	0.15	0.88	0.69	0.00	69.78	todorokite
sebulk-3-050	0.00	0.03	2.35	2.96	66.51	0.40	0.65	0.02	0.03	0.93	1.00	0.00	74.88	todorokite

Highlighted totals are greater than two standard deviations for the specified mineral.

APPENDIX C. X-RAY DIFFRACTION

C.1 Intrusive Rocks

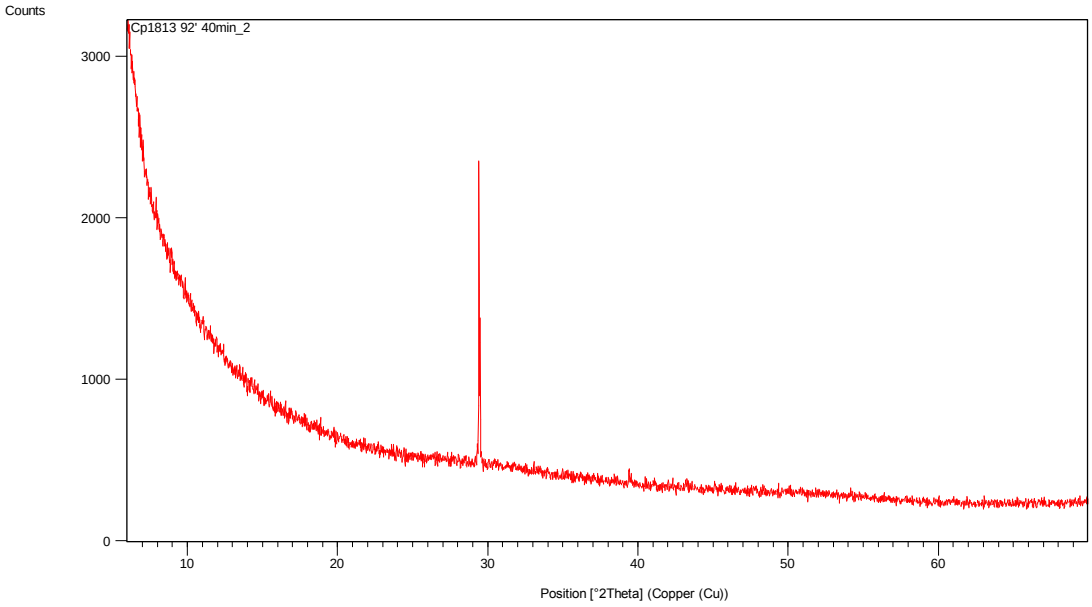

Pos. [°2Th.]	Height [cts]	FWHM Left [°2Th.]	d-spacing [Å]	Rel. Int. [%]	Tip Width	Matched by
29.437080	677.415200	0.122400	3.03183	100.00	0.1469	01-072-1652; 01-075-6049

Visible	Ref. Code	Score	Compound Name	Displacement [°2Th.]	Scale Factor	Chemical Formula
*	01-072-1652	12	Calcium Carbonate	0.000	0.172	Ca C O3
*	01-075-6049	22	Calcium Carbonate	0.000	0.598	Ca (C O3)

Figure C-1: “Clear plagioclase” from Cp1813 92’

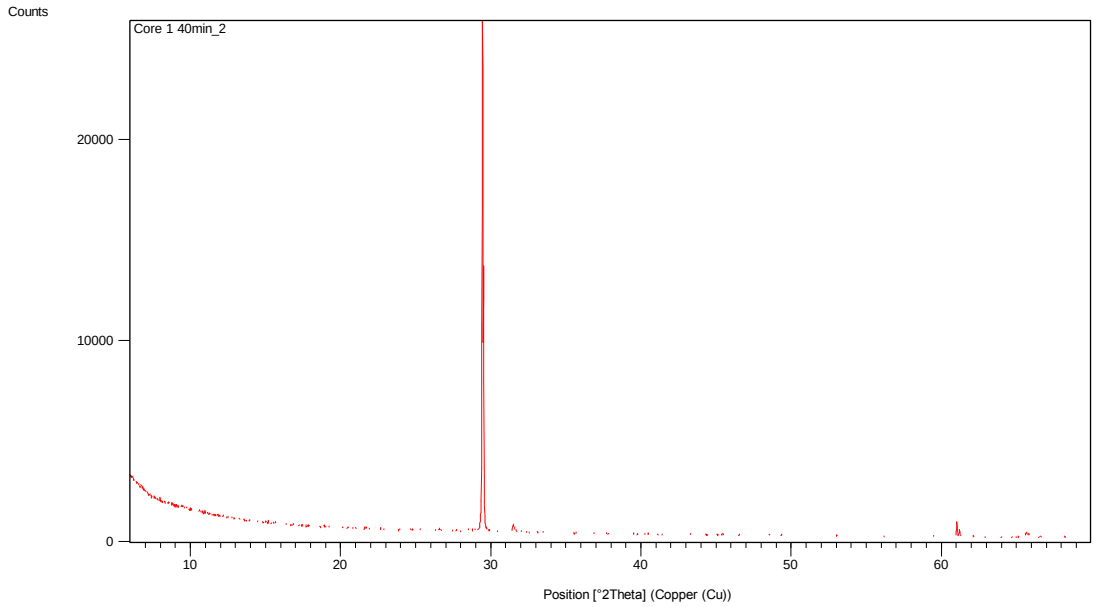

Pos. [°2Th.]	Height [cts]	FWHM Left [°2Th.]	d-spacing [Å]	Rel. Int. [%]	Tip Width	Matched by
29.443960	12854.270000	0.133824	3.03113	100.00	0.1606	01-075-6049
31.475930	206.861500	0.133824	2.83993	1.61	0.1606	01-075-6049
60.980440	403.988400	0.100368	1.51816	3.14	0.1204	01-075-6049
65.590650	132.923500	0.100368	1.42216	1.03	0.1204	01-075-6049

Visible	Ref. Code	Score	Compound Name	Displacement [°2Th.]	Scale Factor	Chemical Formula
*	01-072-7652	No Matching Lines	Carbon Nitrogen	0.000	0.000	C3 N4
*	01-075-6049	26	Calcium Carbonate	0.000	0.239	Ca (C O3)

Figure C-2: “Clear plagioclase” from Core 1

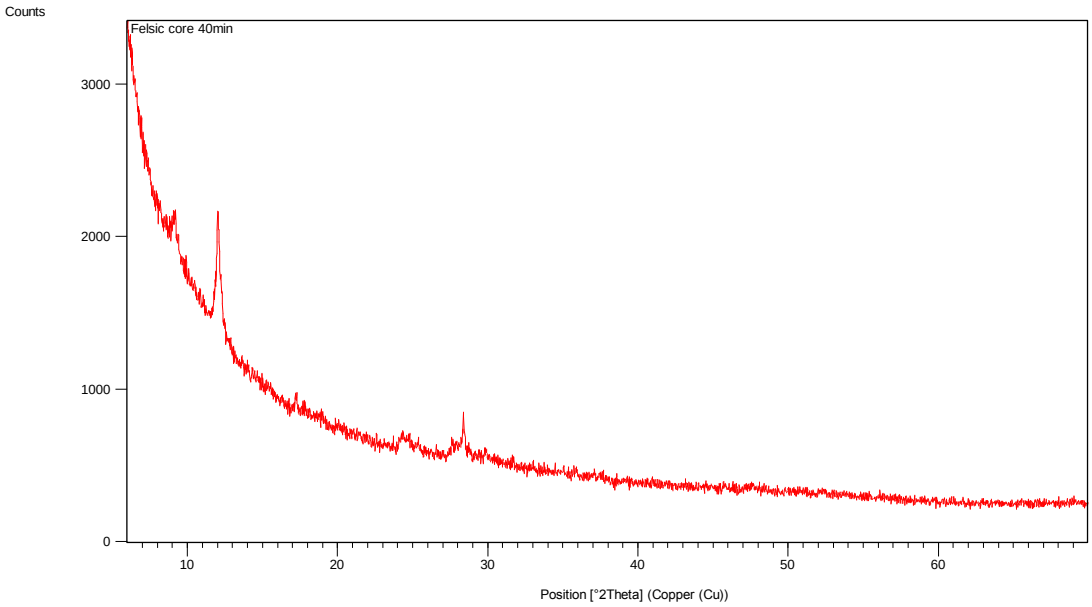

Pos. [°2Th.]	Height [cts]	FWHM Left [°2Th.]	d-spacing [Å]	Rel. Int. [%]	Tip Width	Matched by
9.143161	109.784000	0.401472	9.66444	21.70	0.4818	00-007-0051
12.011290	505.853800	0.100368	7.36237	100.00	0.1204	00-007-0051
24.339600	55.829350	0.669120	3.65400	11.04	0.8029	01-073-9850
28.372040	153.852800	0.100368	3.14317	30.41	0.1204	01-073-9850; 00-058-2010

Visible	Ref. Code	Score	Compound Name	Displacement [°2Th.]	Scale Factor	Chemical Formula
*	01-073-9850	Unmatched Strong	Sodium Aluminum Silicate	0.000	0.271	Na (Al Si3 O8)
*	00-003-0009	No Matching Lines	Iron Magnesium Aluminum Silicate	0.000	0.000	Si3.74 Al2.03 Fe0.03 Mg0.20 O11
*	00-007-0051	2	Sodium Calcium Aluminum Magnesium Silicon Hydroxide Hydrate	0.000	2.933	(Na , Ca)0.3 (Al , Mg)2 Si2 O10 (O H)2 ·n H2 O
*	00-012-0204	No	Sodium	0.000	0.000	Nax (Al ,

		Matching Lines	Magnesium Aluminum Silicate Hydroxide Hydrate			Mg)2 Si4 O10 (O H)2 ·z H2 O
*	00-058-2010	No Matching Lines	Sodium Aluminum Magnesium Silicate Hydroxide Hydrate	0.000	0.000	Na0.3 (Al , Mg)2 Si4 O10 (O H)2 ·x H2 O

Figure C-3: “Cloudy plagioclase” from Felsic core

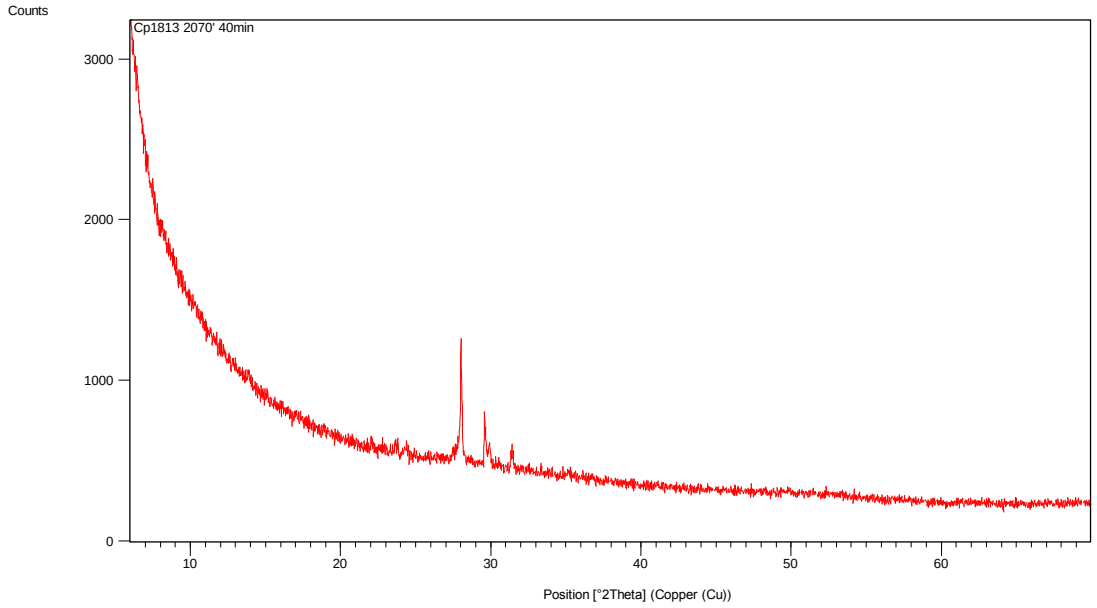

Pos. [°2Th.]	Height [cts]	FWHM Left [°2Th.]	d-spacing [Å]	Rel. Int. [%]	Tip Width	Matched by
28.012240	478.953000	0.133824	3.18272	100.00	0.1606	01-073-9850
29.586670	164.476400	0.100368	3.01684	34.34	0.1204	01-071-0924
31.412050	85.402380	0.167280	2.84556	17.83	0.2007	01-076-0803; 01-073-9850; 01-071-0924

Visible	Ref. Code	Score	Compound Name	Displacement [°2Th.]	Scale Factor	Chemical Formula
*	01-076-0803	Unmatched Strong	Sodium Potassium Aluminum Silicate	0.000	0.129	(Na0.7 K0.3) (Al1.02 Si2.98 O8)
*	01-073-9850	Unmatched Strong	Sodium Aluminum Silicate	0.000	0.218	Na (Al Si3 O8)
*	01-071-0924	Unmatched Strong	Sodium Calcium Aluminum Silicate Chloride	0.000	1.198	Na6.32 Ca1.52 Al7.37 Si16.75 O48 Cl1.90

Figure C-4: “Cloudy plagioclase” from Cp1813 2070’

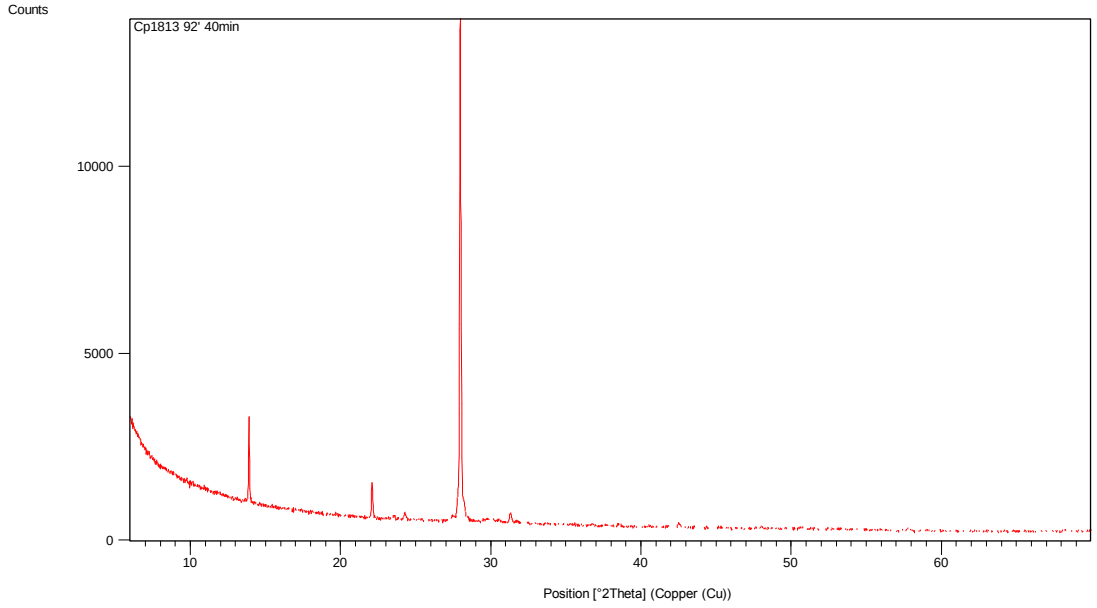

Pos. [°2Th.]	Height [cts]	FWHM Left [°2Th.]	d-spacing [Å]	Rel. Int. [%]	Tip Width	Matched by
13.893430	1326.324000	0.100368	6.36894	16.35	0.1204	01-073-9850
22.086690	577.166800	0.100368	4.02137	7.11	0.1204	01-073-9850
24.253380	111.799000	0.117096	3.66680	1.38	0.1405	01-073-9850
27.956870	8112.089000	0.100368	3.18889	100.00	0.1204	01-073-9850
31.242020	161.182600	0.117096	2.86066	1.99	0.1405	01-073-

						9850
38.537600	31.048770	0.401472	2.33424	0.38	0.4818	01-073-9850
42.452440	69.184430	0.133824	2.12760	0.85	0.1606	01-073-9850
57.758010	33.056810	0.200736	1.59495	0.41	0.2409	01-073-9850

Visible	Ref. Code	Score	Compound Name	Displacement [°2Th.]	Scale Factor	Chemical Formula
*	01-073-9850	17	Sodium Aluminum Silicate	0.000	0.227	Na (Al Si3 O8)

Figure C-5: “Cloudy plagioclase” from Cp1813 92’

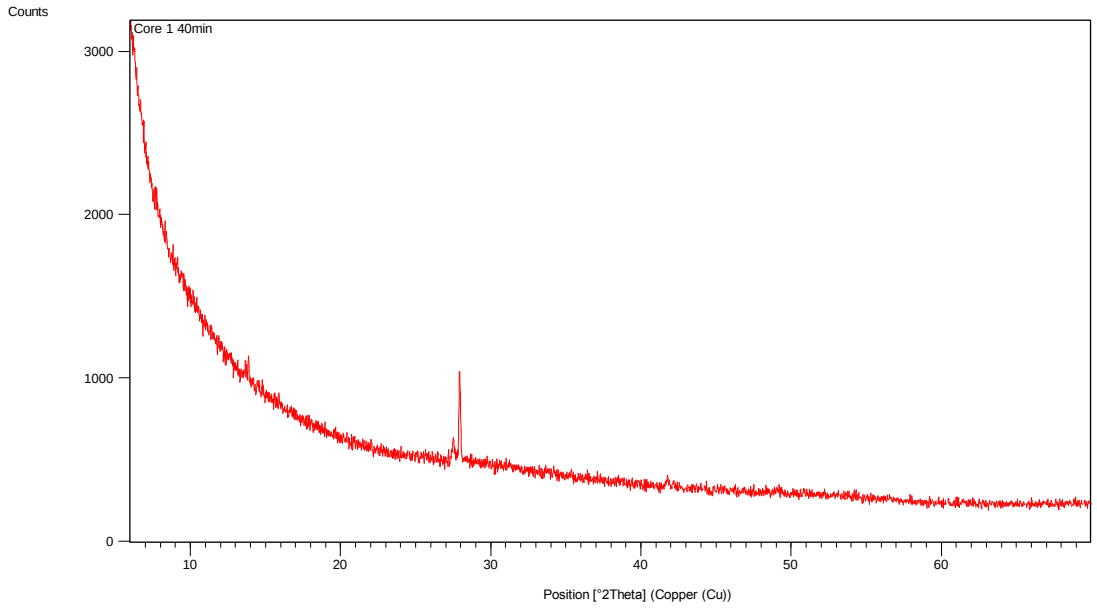

Pos. [°2Th.]	Height [cts]	FWHM Left [°2Th.]	d-spacing [Å]	Rel. Int. [%]	Tip Width	Matched by
6.069730	92.758630	0.401472	14.54942	25.23	0.4818	
27.895250	367.658400	0.117096	3.19580	100.00	0.1405	01-076-0803

Visible	Ref. Code	Score	Compound Name	Displacement [°2Th.]	Scale Factor	Chemical Formula
*	01-076-0803	10	Sodium	0.000	0.272	(Na0.7 K0.3

	Potassium Aluminum Silicate	) (Al1.02 Si2.98 O8)

Figure C-6: “Cloudy plagioclase” from Core 1

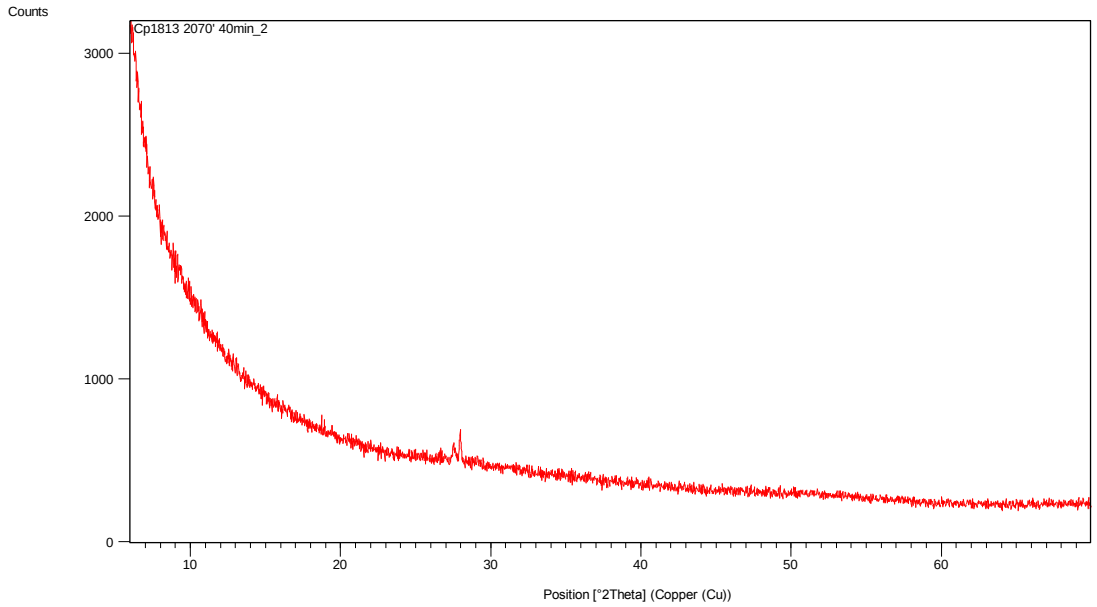

Pos. [°2Th.]	Height [cts]	FWHM Left [°2Th.]	d-spacing [Å]	Rel. Int. [%]	Tip Width	Matched by
6.094523	110.477200	0.401472	14.49029	100.00	0.4818	
27.518010	63.184960	0.200736	3.23875	57.19	0.2409	01-076-0803
27.940900	105.834700	0.133824	3.19068	95.80	0.1606	01-076-0803

Visible	Ref. Code	Score	Compound Name	Displacement [°2Th.]	Scale Factor	Chemical Formula
*	01-076-0803	Unmatched Strong	Sodium Potassium Aluminum Silicate	0.000	0.664	(Na0.7 K0.3) (Al1.02 Si2.98 O8)

Figure C-7: “K-feldspar”from Cp1813 2070’

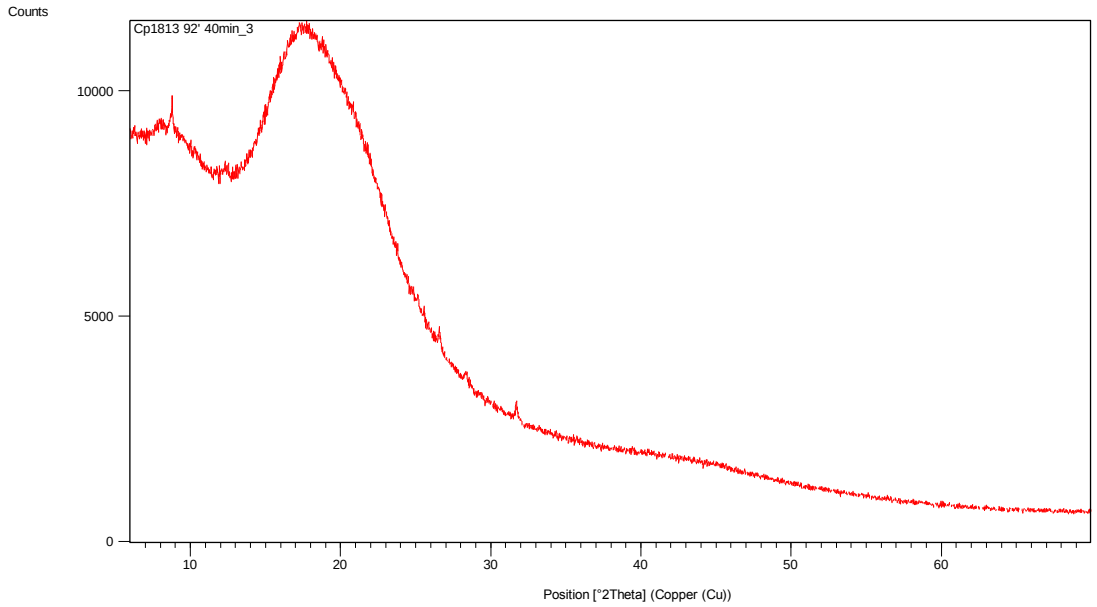

Pos. [°2Th.]	Height [cts]	FWHM Left [°2Th.]	d-spacing [Å]	Rel. Int. [%]	Tip Width	Matched by
8.718917	548.934900	0.401472	10.13371	52.70	0.4818	01-080-1106
17.530200	1041.609000	2.944128	5.05499	100.00	3.5330	01-080-1106
19.259860	827.275400	1.605888	4.60474	79.42	1.9271	01-080-1106
21.485140	165.007800	2.408832	4.13258	15.84	2.8906	01-080-1106
44.109700	41.820560	5.888256	2.05143	4.01	7.0659	01-080-1106

Visible	Ref. Code	Score	Compound Name	Displacement [°2Th.]	Scale Factor	Chemical Formula
*	01-080-1106	3	Potassium Iron Magnesium Aluminum Silicate Hydroxide	0.000	0.978	K Fe Mg2 (Al Si3 O10) (O H)2

Figure C-8: Biotite from Cp1813 92’

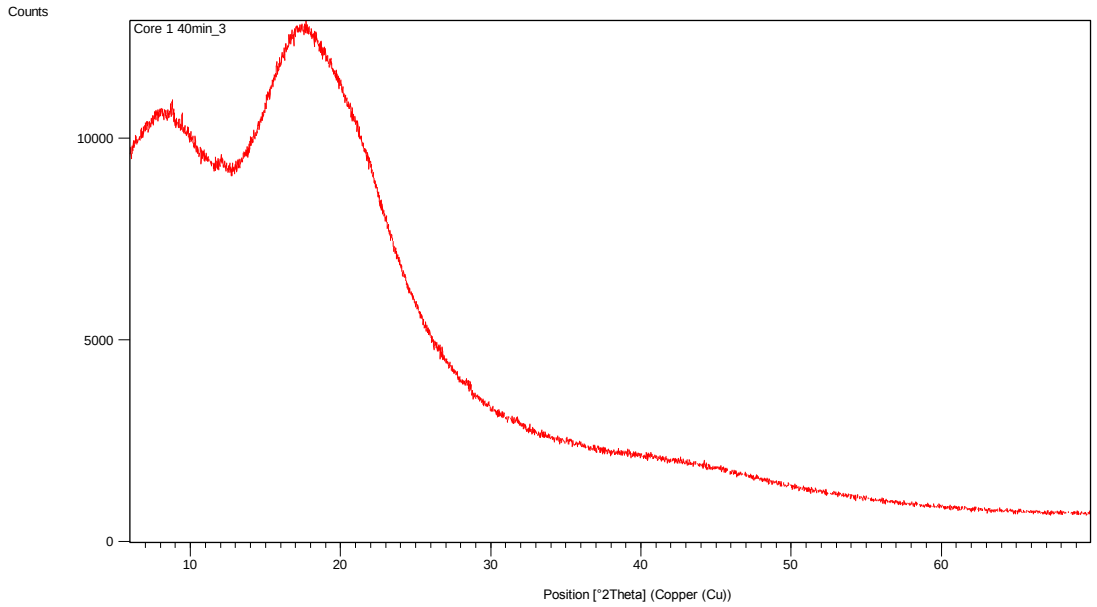

Pos. [°2Th.]	Height [cts]	FWHM Left [°2Th.]	d-spacing [Å]	Rel. Int. [%]	Tip Width	Matched by
8.287720	409.330100	3.264000	10.65996	37.41	3.9168	01-080-1106
17.454420	1094.213000	4.569600	5.07677	100.00	5.4835	01-080-1106
20.986200	260.291000	3.590400	4.22969	23.79	4.3085	01-080-1106
44.267860	40.709230	7.833600	2.04447	3.72	9.4003	01-080-1106

Visible	Ref. Code	Score	Compound Name	Displacement [°2Th.]	Scale Factor	Chemical Formula
*	01-080-1106	No Matching Lines	Potassium Iron Magnesium Aluminum Silicate Hydroxide	0.000	0.000	K Fe Mg2 (Al Si3 O10) (O H)2

Figure C-9: Biotite from Core 1

C.2 Manganese Oxides

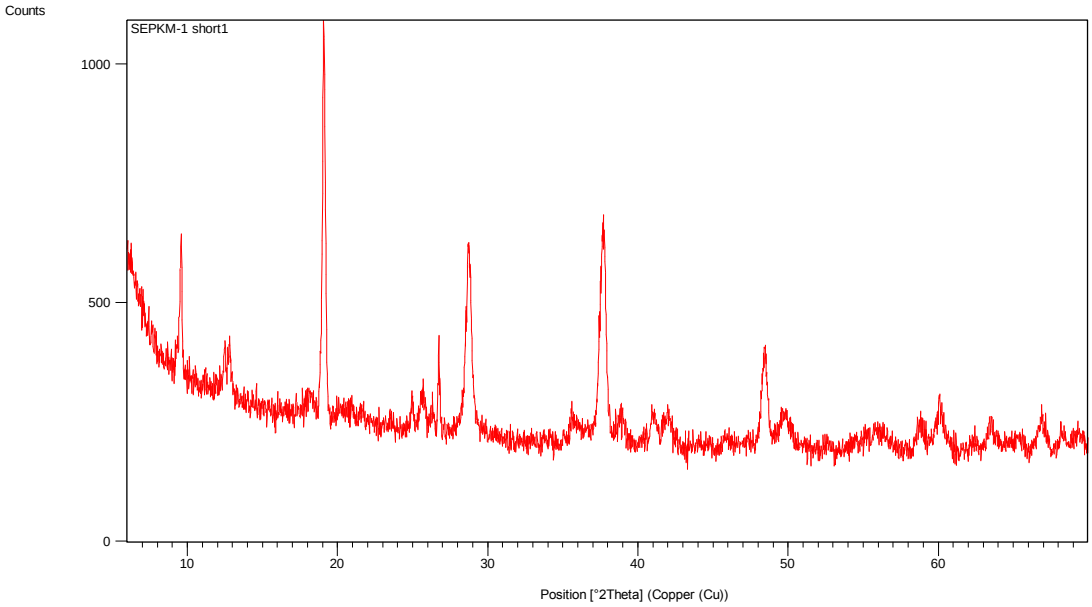

Pos. [°2Th.]	Height [cts]	FWHM Left [°2Th.]	d-spacing [Å]	Rel. Int. [%]	Tip Width	Matched by
9.577715	178.676100	0.133824	9.22690	32.85	0.1606	00-003-0881
12.667150	44.240380	0.535296	6.98261	8.13	0.6424	00-044-1386; 01-084-2049; 00-043-1456
19.073140	543.958300	0.200736	4.64940	100.00	0.2409	00-003-0881
25.597640	40.521720	0.267648	3.47720	7.45	0.3212	00-044-1386; 01-084-2049
26.717310	109.122900	0.133824	3.33397	20.06	0.1606	
28.678910	258.884800	0.167280	3.11023	47.59	0.2007	00-044-1386; 01-084-2049; 00-003-0881
35.712730	17.639100	0.802944	2.51213	3.24	0.9635	00-044-1386; 00-043-1456; 00-003-0881
37.754330	256.685600	0.301104	2.38084	47.19	0.3613	00-044-1386; 01-084-2049

38.870380	27.366060	0.401472	2.31501	5.03	0.4818	00-044-1386; 01-084-2049; 00-043-1456
41.014310	29.844830	0.401472	2.19882	5.49	0.4818	00-044-1386; 01-084-2049; 00-003-0881
41.915040	30.329170	0.401472	2.15362	5.58	0.4818	00-044-1386; 01-084-2049; 00-043-1456
48.409410	120.684700	0.401472	1.87879	22.19	0.4818	00-043-1456; 00-003-0881
49.672250	33.299720	0.669120	1.83394	6.12	0.8029	00-044-1386; 01-084-2049; 00-043-1456
58.709990	28.759790	0.535296	1.57134	5.29	0.6424	00-044-1386; 01-084-2049; 00-043-1456
60.051100	49.182420	0.535296	1.53941	9.04	0.6424	00-044-1386; 01-084-2049; 00-043-1456; 00-003-0881
63.427040	31.674090	0.535296	1.46536	5.82	0.6424	00-003-0881
66.844830	39.647180	0.535296	1.39849	7.29	0.6424	00-044-1386; 01-084-2049; 00-043-1456; 00-003-0881

Visible	Ref. Code	Score	Compound Name	Displacement [°2Th.]	Scale Factor	Chemical Formula
*	00-044-1386	22	Potassium Manganese Oxide	0.000	0.339	K2-x Mn8 O16
*	01-084-2049	29	Lead Manganese Oxide	0.000	0.335	Pb1.34 Mn8 O16
*	00-043-1456	0	Sodium Manganese	0.000	6.684	Na0.55 Mn2 O4 ·1.5 H2

*	00-003-0881	Unmatched Strong	Oxide Hydrate Magnesium Silicate Hydroxide	0.000	0.432	O Mg3 Si4 O10 (O H)2

Figure C-10: SE-PKM-1, vein A

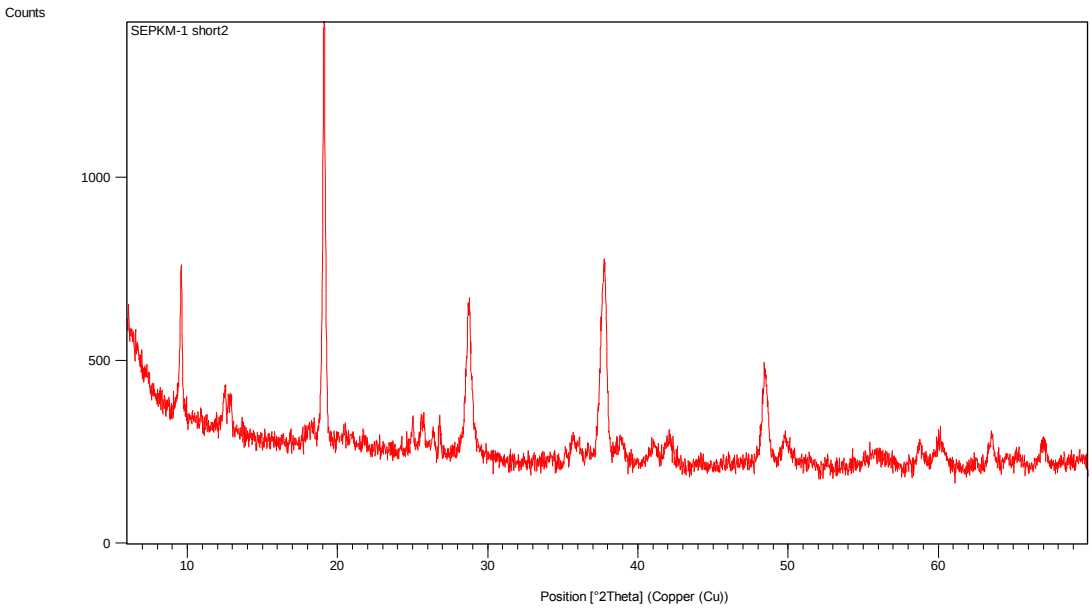

Pos. [°2Th.]	Height [cts]	FWHM Left [°2Th.]	d-spacing [Å]	Rel. Int. [%]	Tip Width	Matched by
9.589890	273.259600	0.117096	9.21521	36.49	0.1405	00-003-0881
12.651480	37.949020	0.535296	6.99122	5.07	0.6424	00-044-1386; 01-084-2049; 00-043-1456
19.087600	748.840300	0.133824	4.64591	100.00	0.1606	00-003-0881
24.970730	43.997170	0.200736	3.56306	5.88	0.2409	00-043-1456
25.634230	40.397810	0.267648	3.47232	5.39	0.3212	00-044-1386; 01-084-2049; 00-002-0056
26.765510	62.930540	0.133824	3.32807	8.40	0.1606	01-074-1811; 00-

28.755580	263.066500	0.200736	3.10211	35.13	0.2409	002-0056 00-044-1386; 01-084-2049; 00-003-0881
35.792140	26.127360	0.535296	2.50674	3.49	0.6424	00-044-1386; 00-043-1456; 00-003-0881; 00-002-0056
37.794080	313.697400	0.434928	2.37843	41.89	0.5219	00-044-1386; 00-002-0056
38.855550	29.756720	0.401472	2.31586	3.97	0.4818	00-044-1386; 01-084-2049; 00-043-1456
40.989650	24.126870	0.401472	2.20008	3.22	0.4818	00-044-1386; 01-084-2049; 00-002-0056
42.014250	39.962370	0.401472	2.14877	5.34	0.4818	00-044-1386; 01-084-2049; 00-043-1456; 01-074-1811
48.410800	163.911200	0.301104	1.87874	21.89	0.3613	00-043-1456; 00-003-0881
49.768730	41.795450	0.401472	1.83061	5.58	0.4818	00-044-1386; 01-084-2049; 00-043-1456; 01-074-1811
58.724430	32.093650	0.401472	1.57098	4.29	0.4818	00-044-1386; 01-084-2049; 00-043-1456
60.074520	39.812460	0.535296	1.53886	5.32	0.6424	00-044-1386; 01-084-2049; 00-043-1456; 00-003-0881
63.507820	47.418360	0.267648	1.46369	6.33	0.3212	00-003-0881; 01-074-1811

66.959930	35.737070	0.401472	1.39637	4.77	0.4818	00-044-1386; 01-084-2049; 00-043-1456; 00-003-0881; 01-074-1811

Visible	Ref. Code	Score	Compound Name	Displacement [°2Th.]	Scale Factor	Chemical Formula
*	00-044-1386	19	Potassium Manganese Oxide	0.000	0.269	K2-x Mn8 O16
*	01-084-2049	28	Lead Manganese Oxide	0.000	0.224	Pb1.34 Mn8 O16
*	00-043-1456	0	Sodium Manganese Oxide Hydrate	0.000	7.277	Na0.55 Mn2 O4 ·1.5 H2 O
*	00-003-0881	Unmatched Strong	Magnesium Silicate Hydroxide	0.000	0.308	Mg3 Si4 O10 (O H)2
*	01-074-1811	0	Silicon Oxide	0.000	5.596	Si O2
*	00-002-0056	Unmatched Strong	Potassium Aluminum Silicate Hydroxide	0.000	0.664	K Al2 Si3 Al O10 (O H)2

Figure C-11: SE-PKM-1, vein A hard

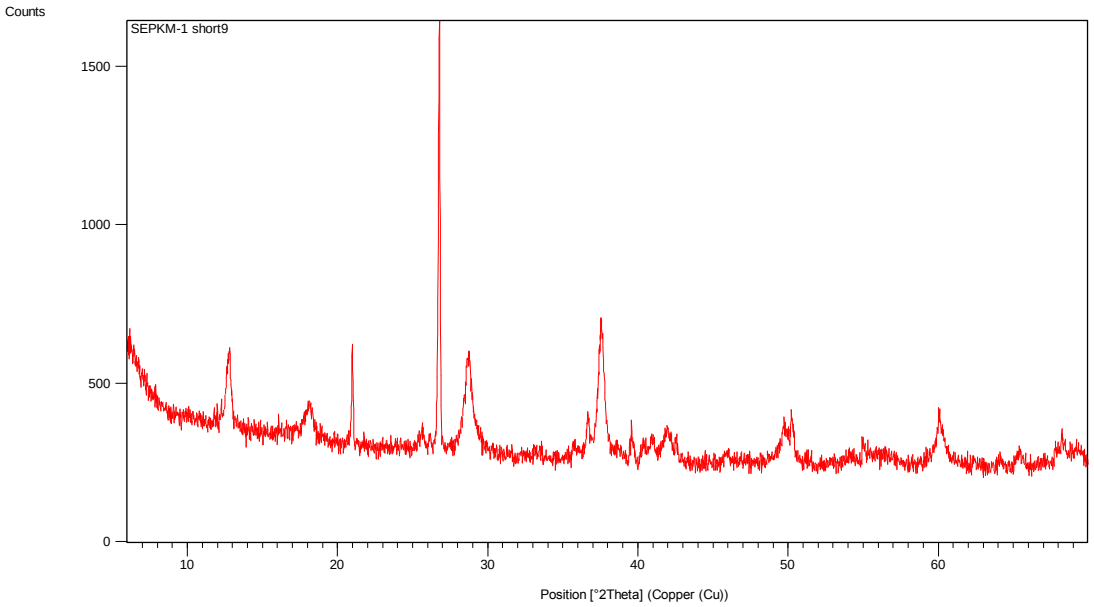

Pos. [°2Th.]	Height [cts]	FWHM Left [°2Th.]	d-spacing [Å]	Rel. Int. [%]	Tip Width	Matched by
6.216909	25.495160	0.802944	14.20530	2.80	0.9635	
12.755100	141.539600	0.267648	6.93466	15.55	0.3212	00-044-1386; 01-084-2049
18.168390	62.308090	0.401472	4.87884	6.84	0.4818	00-044-1386; 01-084-2049; 00-029-0713
20.976010	172.370400	0.100368	4.23172	18.93	0.1204	01-070-7344; 00-029-0713
26.754040	910.382200	0.117096	3.32947	100.00	0.1405	01-070-7344
28.694600	182.096300	0.401472	3.10856	20.00	0.4818	00-044-1386; 01-084-2049
36.642380	68.419510	0.200736	2.45050	7.52	0.2409	00-044-1386; 01-084-2049; 01-070-7344; 00-029-0713
37.557320	248.430200	0.301104	2.39288	27.29	0.3613	00-044-1386; 01-084-2049
39.565190	56.077840	0.267648	2.27595	6.16	0.3212	01-070-7344

41.884860	49.799400	0.468384	2.15511	5.47	0.5621	00-044-1386; 01-084-2049
50.199790	71.408040	0.401472	1.81590	7.84	0.4818	00-044-1386; 01-070-7344
60.007740	96.654170	0.267648	1.54042	10.62	0.3212	00-044-1386; 01-084-2049; 01-070-7344
65.317230	24.259600	0.535296	1.42745	2.66	0.6424	00-044-1386; 01-084-2049; 00-029-0713
68.179520	43.455300	0.535296	1.37433	4.77	0.6424	00-044-1386; 01-084-2049; 01-070-7344; 00-029-0713

Visible	Ref. Code	Score	Compound Name	Displacement [°2Th.]	Scale Factor	Chemical Formula
*	00-044-1386	30	Potassium Manganese Oxide	0.000	0.280	K2-x Mn8 O16
*	01-084-2049	25	Lead Manganese Oxide	0.000	0.160	Pb1.34 Mn8 O16
*	01-070-7344	15	Silicon Oxide	0.000	0.208	Si O2
*	00-029-0713	1	Iron Oxide Hydroxide	0.000	0.183	Fe +3 O (O H)

Figure C-12: SE-PKM-1, cluster D

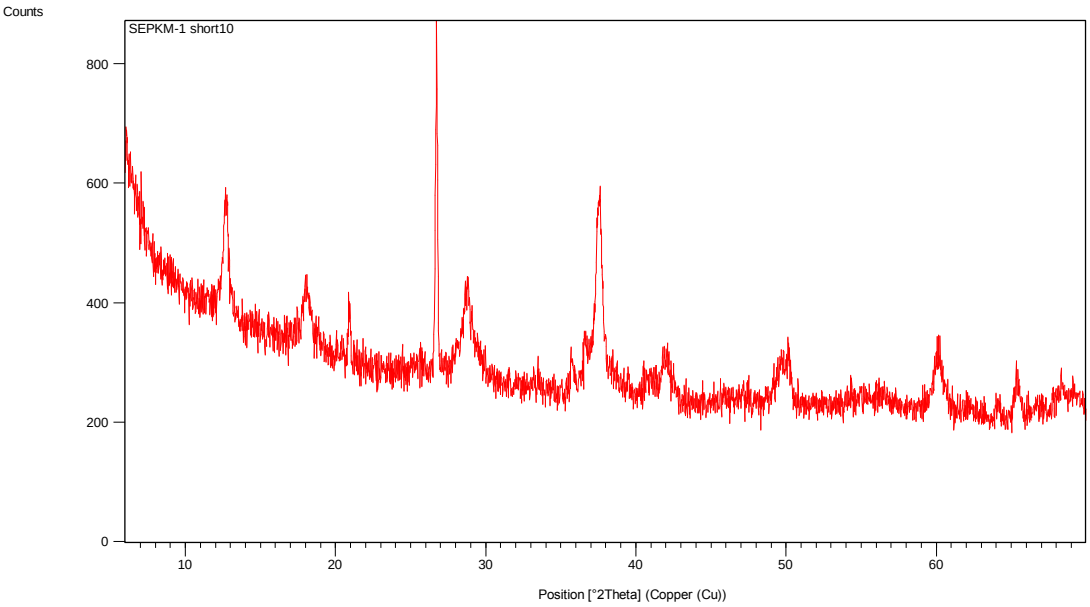

Pos. [°2Th.]	Height [cts]	FWHM Left [°2Th.]	d-spacing [Å]	Rel. Int. [%]	Tip Width	Matched by
6.245989	32.562010	0.802944	14.13923	9.20	0.9635	
12.711220	124.580100	0.334560	6.95850	35.18	0.4015	00-044-1386; 01-084-2048; 00-043-1456
18.076310	51.423460	0.401472	4.90349	14.52	0.4818	00-044-1386; 01-084-2048
20.894050	50.080020	0.200736	4.24814	14.14	0.2409	01-070-7344
26.705670	354.113000	0.133824	3.33539	100.00	0.1606	01-070-7344
28.745930	90.181320	0.401472	3.10313	25.47	0.4818	00-044-1386; 01-084-2048
37.512580	192.015600	0.334560	2.39563	54.22	0.4015	00-044-1386; 01-084-2048
41.921740	44.702680	0.535296	2.15330	12.62	0.6424	00-044-1386; 01-084-2048; 00-043-1456
50.122270	50.236050	0.401472	1.81852	14.19	0.4818	00-044-1386; 01-084-2048; 00-043-

60.062790	55.310430	0.535296	1.53914	15.62	0.6424	1456; 01-070-7344
65.342480	39.723610	0.401472	1.42696	11.22	0.4818	00-044-1386; 01-084-2048; 00-043-1456; 01-070-7344

Visible	Ref. Code	Score	Compound Name	Displacement [°2Th.]	Scale Factor	Chemical Formula
*	00-044-1386	24	Potassium Manganese Oxide	0.000	0.481	K2-x Mn8 O16
*	01-084-2048	9	Lead Manganese Oxide	0.000	0.240	Pb1.07 Mn8 O16
*	00-043-1456	No Matching Lines	Sodium Manganese Oxide Hydrate	0.000	0.000	Na0.55 Mn2 O4 ·1.5 H2 O
*	01-070-7344	21	Silicon Oxide	0.000	0.499	Si O2

Figure C-13: SE-PKM-1, dendrite E

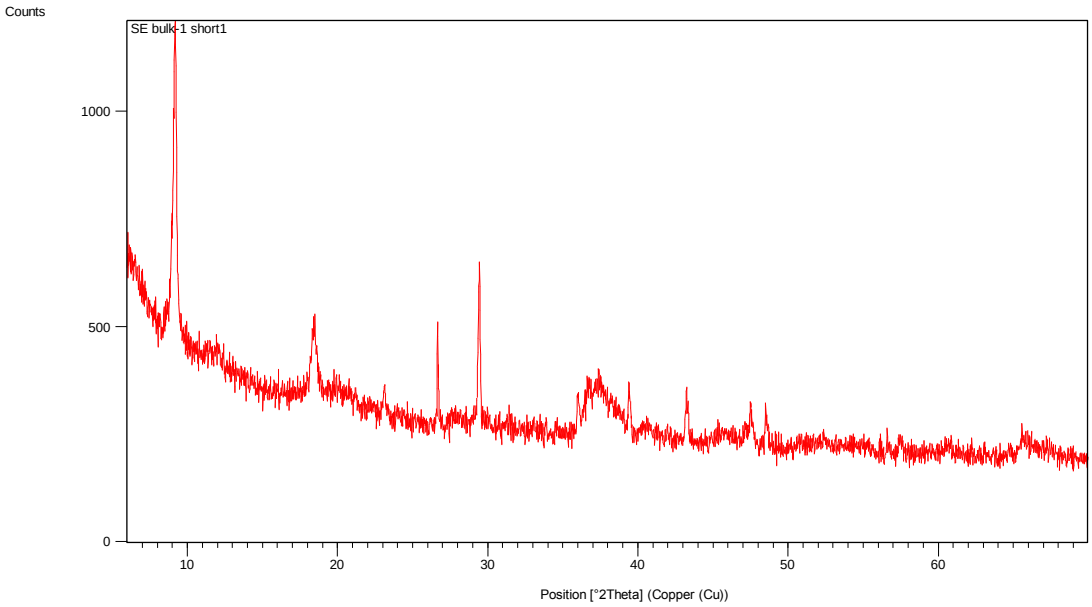

Pos. [°2Th.]	Height [cts]	FWHM Left [°2Th.]	d-spacing [Å]	Rel. Int. [%]	Tip Width	Matched by
6.345348	28.261470	0.802944	13.91805	6.31	0.9635	
9.203472	448.218000	0.184008	9.60124	100.00	0.2208	00-038-0475
18.413490	97.219540	0.334560	4.81445	21.69	0.4015	00-038-0475
26.657480	125.122000	0.100368	3.34131	27.92	0.1204	01-070-7344
29.427570	247.680800	0.117096	3.03278	55.26	0.1405	00-005-0586; 00-038-0475
35.997390	47.355570	0.200736	2.49291	10.57	0.2409	00-005-0586
39.388980	64.456220	0.167280	2.28572	14.38	0.2007	00-005-0586; 01-070-7344; 00-038-0475
43.168350	61.856370	0.200736	2.09396	13.80	0.2409	00-005-0586; 00-038-0475
47.495680	53.469180	0.200736	1.91278	11.93	0.2409	00-005-0586; 00-038-0475
48.522970	48.875020	0.200736	1.87466	10.90	0.2409	00-005-0586; 00-038-0475
65.780510	15.011180	0.802944	1.41852	3.35	0.9635	00-005-0586; 01-

						070-7344; 00-038-0475

Visible	Ref. Code	Score	Compound Name	Displacement [°2Th.]	Scale Factor	Chemical Formula
*	00-005-0586	38	Calcium Carbonate	0.000	0.594	Ca C O3
*	01-070-7344	10	Silicon Oxide	0.000	0.148	Si O2
*	00-038-0475	10	Sodium Manganese Oxide Hydrate	0.000	0.810	Na Mn6 O12 ·3 H2 O

Figure C-14: SE-bulk-1, dendrite A

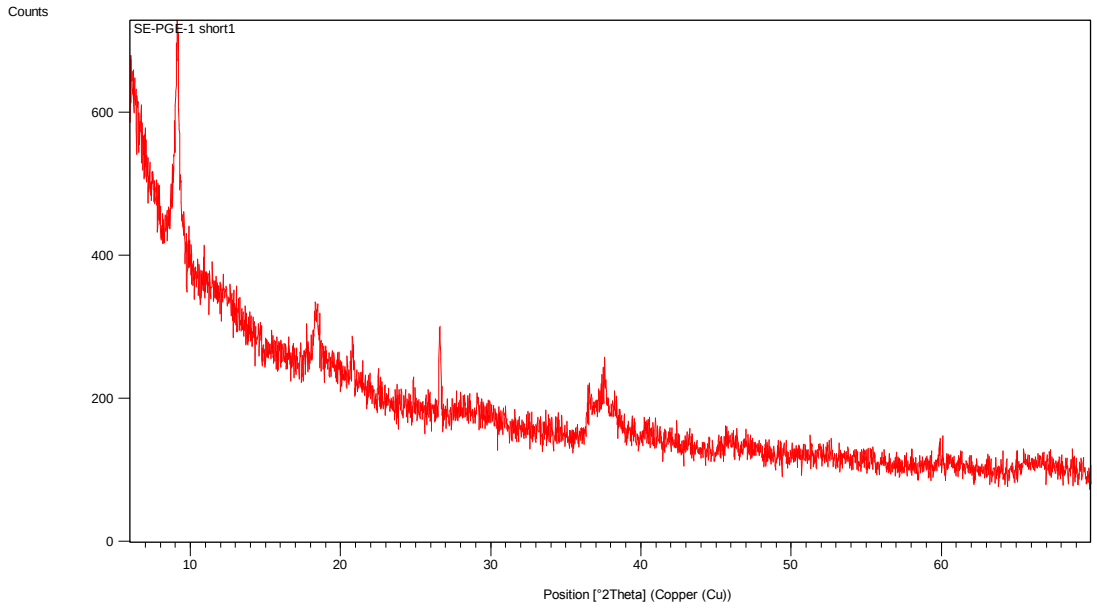

Pos. [°2Th.]	Height [cts]	FWHM Left [°2Th.]	d-spacing [Å]	Rel. Int. [%]	Tip Width	Matched by
6.210003	44.335000	0.401472	14.22108	20.72	0.4818	
9.146000	213.960100	0.133824	9.66144	100.00	0.1606	00-038-0475
18.357690	49.316480	0.267648	4.82896	23.05	0.3212	00-038-0475
26.591760	81.751460	0.133824	3.34942	38.21	0.1606	01-070-7344

Visible	Ref. Code	Score	Compound Name	Displacement [°2Th.]	Scale Factor	Chemical Formula
*	01-070-7344	13	Silicon Oxide	0.000	0.319	Si O2
*	00-038-0475	9	Sodium Manganese Oxide Hydrate	0.000	0.426	Na Mn6 O12 ·3 H2 O
*	00-029-0713	No Matching Lines	Iron Oxide Hydroxide	0.000	0.000	Fe +3 O (O H)
*	00-002-0056	Unmatched Strong	Potassium Aluminum Silicate Hydroxide	0.000	0.206	K Al2 Si3 Al O10 (O H)2

Figure C-15: SE-PGE-1, dendrite A

APPENDIX D. STABLE ISOTOPES

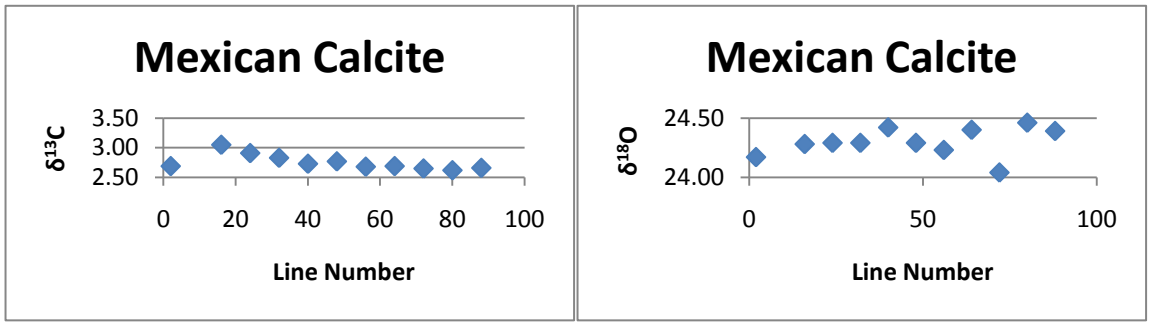

Figure D-1: Mexican calcite plotted with a) $\delta^{13}C$ and b) $\delta^{18}O$.

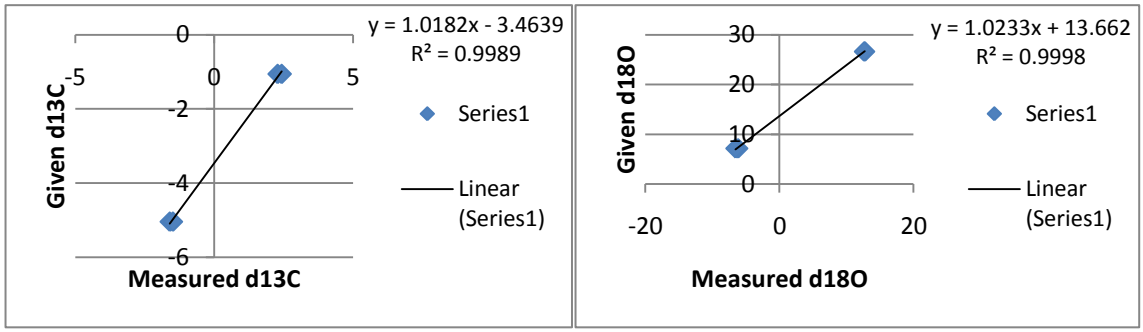

Figure D-2: Correction curves for data a) $\delta^{13}C$, b) $\delta^{18}O$.

Table D-1: Isotope standards

	d13C Measured	PDB Given	d18O Measured	PDB Given	SMOW Given
IAEA-CO-9	-43.0316	-47.3	1.7632	-15.4	15.03
IAEA-CO-9	-43.7058	-47.3	1.3714	-15.4	15.03
Solenhofen	2.2857	-1.06	12.7483	-4.14	26.64
Solenhofen	2.4317	-1.06	12.6127	-4.14	26.64
NBS-18 Carbonatite	-1.6026	-5.04	-6.1572	-23.05	7.16
NBS-18 Carbonatite	-1.4889	-5.04	-6.5451	-23.05	7.16

Table D-2: All Luis Lopez and Santa Eulalia data.

Sample	Mineral	$\delta^{13}C$ Measured	$\delta^{18}O$ Measured	$\delta^{13}C_{HCO3-}$ Calculated	$\delta^{18}O_{H2O}$ Calculated	T (°C)	$\delta^{13}C$ Calculated	$\delta^{18}O$ Calculated	T (°C)	$\delta^{13}C$ Calculated	$\delta^{18}O$ Calculated
Luis Lopez											
MCA location: Zone 13S, 0319045N, 3758491E, elevation: 5322 ± 35 ft											
MCA-1-A	Calcite	-4.7	23.8	-3.5	21.8	175	-4.8	29.6	375	-4.6	17.2
MCA-1-B	Calcite	-5.5	23.1	-4.3	21.0	175	-5.7	28.9	375	-5.4	16.4
MCA-1-C	Calcite	-5.6	24.5	-4.3	22.4	175	-5.7	30.2	375	-5.4	17.8
MCA-1-D	Calcite	-4.0	24.4	-2.7	22.4	175	-4.1	30.2	375	-3.8	17.8
MCA-1-E	Calcite	-5.4	24.6	-4.2	22.5	175	-5.5	30.3	375	-5.3	17.9
MCA-2-A	Calcite	-0.6	13.5	0.7	11.5	175	-0.7	19.3	375	-0.5	6.9
MCA-2-B	Calcite	0.7	12.5	1.9	10.5	175	0.6	18.3	375	0.8	5.9
MCA-2-C	Calcite	0.2	13.2	1.5	11.1	175	0.1	19.0	375	0.4	6.5
MCA-2-D	Calcite	0.6	12.4	1.9	10.4	175	0.5	18.2	375	0.8	5.8

MCA-3-A	Calcite	-2.0	18.1	-0.8	16.1	175	-2.1	23.9	375	-1.9	11.5
MCA-3-B	Calcite	-2.5	18.3	-1.2	16.3	175	-2.6	24.1	375	-2.3	11.7
MCA-3-C	Calcite	-2.0	17.3	-0.7	15.3	175	-2.1	23.1	375	-1.8	10.7
MCA-3-D	Calcite	-4.6	23.5	-3.4	21.4	175	-4.7	29.2	375	-4.5	16.8
MCA-4-A	Calcite	-0.2	12.7	1.1	10.6	175	-0.3	18.5	375	0.0	6.0
MCA-4-B	Calcite	-0.4	12.6	0.9	10.6	175	-0.5	18.4	375	-0.2	6.0
MCA-4-C	Calcite	-0.1	19.2	1.1	17.2	175	-0.2	25.0	375	0.0	12.6
MCA-4-D	Calcite	-2.2	17.8	-0.9	15.8	175	-2.3	23.6	375	-2.0	11.2
MCA-5	Calcite	-0.4	11.6	0.8	9.5	175	-0.6	17.3	375	-0.3	4.9
MCA-6-A	Calcite	-2.7	19.9	-1.5	17.8	175	-2.9	25.6	375	-2.6	13.2
MCA-6-B	Calcite	-3.1	19.8	-1.9	17.7	175	-3.2	25.6	375	-3.0	13.1
MCA-6-C	Calcite	-3.5	19.4	-2.2	17.3	175	-3.6	25.2	375	-3.3	12.7
MCA-6-D	Calcite	-3.2	19.3	-2.0	17.3	175	-3.4	25.1	375	-3.1	12.7
MCA-6-E	Calcite	-0.9	17.3	0.3	15.3	175	-1.0	23.1	375	-0.8	10.7
MCA-6-F	Calcite	-0.7	16.0	0.5	14.0	175	-0.9	21.8	375	-0.6	9.4
MCA-6-G	Calcite	0.2	14.3	1.5	12.3	175	0.1	20.1	375	0.3	7.7
MCA-6-H	Calcite	0.2	14.1	1.4	12.0	175	0.0	19.9	375	0.3	7.4
MCA-7-A	Calcite	0.0	12.6	1.2	10.5	175	-0.2	18.3	375	0.1	5.9
MCA-7-B	Calcite	0.0	12.3	1.2	10.2	175	-0.1	18.1	375	0.1	5.6
MCA-7-C	Calcite	-0.6	13.6	0.7	11.6	175	-0.7	19.4	375	-0.5	7.0
Nogal Canyon location: Zone 13S, 0320428N, 3754041E, elevation: 5013 ± 35 ft											
NOGAL-1-A	Calcite	-3.0	21.9								
NOGAL-1-B	Calcite	-1.5	19.0								
NOGAL-1-C	Calcite	-1.0	16.8								
NOGAL-1-D	Calcite	-0.2	18.0								
NOGAL-1-E	Calcite	-0.5	17.1								
NOGAL-2-A	Calcite	1.2	16.8								
NOGAL-2-B	Calcite	-0.4	17.2								
Pretty Girl location: Zone 13S, 0316546N, 3758751E, elevation: 5703 ± 21 ft											
PG-1	Calcite	-3.4	19.9								
PG-2	Calcite	-5.3	22.1								
BC-1-A	Calcite	-7.7	20.8	-6.4	18.7	175	-7.8	26.5	300	-7.6	17.8
BC-1-B	Calcite	-6.5	20.3	-5.3	18.3	175	-6.6	26.1	300	-6.5	17.3
BC-2-A	Calcite	-2.5	12.8	-1.2	10.8	175	-2.6	18.6	300	-2.4	9.8
BC-2-B	Calcite	-5.4	17.6	-4.2	15.5	175	-5.6	23.3	300	-5.4	14.6
BC-2-C	Calcite	-2.8	14.8	-1.5	12.8	175	-2.9	20.6	300	-2.7	11.8
BC-2-D	Calcite	-2.2	12.5	-0.9	10.4	175	-2.3	18.3	300	-2.1	9.5
BC-2-E	Calcite	-6.7	21.7	-5.4	19.6	175	-6.8	27.4	300	-6.6	18.7
NANCY-A	Calcite	0.0	12.8	1.3	12.3	225	0.0	16.1	300	0.1	11.4
NANCY-B	Calcite	-0.2	13.2	1.0	12.7	225	-0.3	16.5	300	-0.2	11.8
Water Canyon											
003301-A	Calcite	-0.7	15.6								
003301-B	Calcite	-2.5	17.6								
003301-C	Calcite	-1.0	16.2								
003301-D	Calcite	-1.5	17.0								
003301-E	Calcite	-0.6	15.3								
003303-A	Calcite	-4.3	19.7								
003303-B	Calcite	-1.5	16.8								
003304-A	Calcite	-1.2	17.3								
003304-B	Calcite	-1.3	18.6								
003304-C	Calcite	-1.1	17.1								
003304-D	Calcite	-1.7	18.3								
003304-E	Calcite	-1.2	17.2								
003304A-A	Calcite	-0.6	17.5								
003304A-B	Calcite	-1.8	18.3								
003304A-C	Calcite	-1.3	18.7								
003304A-D	Calcite	-1.2	17.5								
003304B-A	Calcite	-1.7	19.4								
003304B-B	Calcite	-1.5	17.6								
003304B-C	Calcite	-1.1	17.2								
003308-A	Calcite	-0.6	15.8								
003308-B	Calcite	-0.9	16.0								
003308-C	Calcite	-1.1	16.3								
Data from Campbell											
Luis Lopez											
TM1-1	Calcite	-5.3	21.9	-4.2	24.2	150	-5.6	34.4	400	-5.3	18.5
TM1-2	Calcite	-5.3	22.1	-4.2	24.3	150	-5.6	34.6	400	-5.3	18.7
TM1-3	Calcite	-5.0	19.6	-3.8	21.9	150	-5.2	32.1	400	-4.9	16.2
TM2-1	Calcite	-6.2	21.8	-5.0	24.1	150	-6.5	34.3	400	-6.1	18.4
TM2-2	Calcite	-5.3	21.8	-4.2	24.1	150	-5.6	34.3	400	-5.3	18.4
TM2-2 (Dup)	Calcite	-5.3	21.6	-4.2	23.8	150	-5.6	34.0	400	-5.3	18.2
TM2-3	Calcite	-5.1	21.5	-4.0	23.8	150	-5.4	34.0	400	-5.1	18.2
TM2-4	Calcite	-6.3	22.4	-5.1	24.7	150	-6.5	34.9	400	-6.2	19.1
MCA-1	Calcite	-2.7	20.7	-1.4	18.7	125	-2.9	31.6	375	-2.6	14.1

MCA2-1	Calcite	-3.0	22.3	-1.7	20.2	125	-3.2	33.1	375	-2.9	15.6
MCA-4	Calcite	-4.3	21.8	-3.1	19.8	125	-4.6	32.7	375	-4.2	15.2
MCA-4 (Dup)	Calcite	-4.3	21.9	-3.0	19.8	125	-4.5	32.7	375	-4.2	15.2
MCA-6	Calcite	0.6	13.2	1.9	11.2	125	0.4	24.1	375	0.8	6.6
MCA-7	Calcite	-2.4	22.0	-1.1	19.9	125	-2.6	32.8	375	-2.3	15.3
MCA-ED WHITECC	Calcite	-0.2	11.8	1.1	9.7	125	-0.4	22.6	375	-0.1	5.2
MCA-ED BLACKCC	Calcite	0.5	12.1	1.8	10.1	125	0.3	22.9	375	0.6	5.5
G-4	Calcite	-6.1	20.9	-4.8	20.4	160	-6.3	29.6	360	-6.0	16.5
G-4 (Dup)	Calcite	-6.1	20.8	-4.8	20.3	160	-6.3	29.5	360	-6.0	16.4
G-1	Calcite	-6.8	21.8	-5.5	21.3	160	-7.0	30.5	360	-6.7	17.4
G-2	Calcite	-2.2	12.1	-1.0	11.6	160	-2.4	20.8	360	-2.2	7.7
G-3	Calcite	-6.1	20.8	-4.9	20.3	160	-6.3	29.5	360	-6.0	16.3

Santa Eulalia

28°37'23.82"N, 105°52'26.55"W, elevation: 1942 m
28°37'29.65"N, 105°52'30.79"W, elevation: 1963 m

SE-PKM-1	Limestone	-4.2	16.6
SE-PGD-1	Limestone	-2.9	23.3
SE-PGE-1	Limestone	-2.2	23.6
SE-BULK-1	Limestone	-7.6	19.5

Data from Megaw (1990)

unaltered Finlay LS	Limestone	-0.8	21.8

Perpendicular to Chorro fissure 18th level Buena Tierra Mine

In ore	Calcite	-1.6	15.42
At contact	Limestone	1.33	14.27
	Limestone	1.2	14.1
0.5m from ore	Limestone	2.96	18.74
1m from ore	Limestone	2.46	17.97
5m from ore	Limestone	2.45	17.76
25m from ore	Limestone	2.96	21.86
100m from ore	Limestone	3.04	24.26
230m from ore (near Peru fissure)	Limestone	2.45	17.76
Binigno LS Cp1813 455m	Limestone	-0.56	15.48

Manganese Altered Finlay LS N West Camp

Center of alteration	Limestone	-3.92	16.25
Altered and fresh contact	Limestone	-2.61	18.16
0.5m from contact	Limestone	-1.84	21.66
Unaltered in altered area	Limestone	-1.85	21.32
Fresh 100m from alteration	Limestone	0.2	21.06

Perpendicular to skarn mineralization San Antonio Mine

In ore	Calcite	-10.12	12.82
	Calcite	-10.01	12.72
At skarn contact	Limestone	2.3	13.49
0.5m from ore	Limestone	2.44	14.48
1m from ore	Limestone	2.58	13.55
12m from ore	Limestone	2.71	14.59
50m from ore	Limestone	2.33	18.53
Benigno LS SA 955 198m	Limestone	-0.28	14.33

APPENDIX E. $^{40}AR/^{39}AR$ GEOCHRONOLOGY

E.1 Intrusive Rocks Data

The sensitivity for the intrusive rocks for the multiplier is $5.13e^{-17}$ moles/pA, while the discrimination for the multiplier is 1.006 ± 0.001.

E.1.1 Data Tables

Table E-1: Argon isotopic data for intrusive separates.

	ID	Power (Watts)	$^{40}Ar/^{39}Ar$	$^{39}Ar_K$ (x 10^{-15} mol)	K/Ca	Cl/K	$^{40}Ar^*$ (%)	^{39}Ar (%)	Age (Ma)	±1s (Ma)
	Cp 1813 92, plag (clear), 2.37 mg, J=0.0023647±0.09%, D=1.006±0.001, NM-231F, Lab#=59510-01									
Xi	A	1	408.9	0.032	0.006	0.24	12.6	2.9	220.68	39.90
	B	2	47.67	0.055	0.002	0.008	24.6	7.8	59.06	17.96
	C	3	48.44	0.144	0.003	0.015	16.4	20.5	38.56	9.82
	D	4	39.68	0.118	0.004	0.008	20.4	31.0	37.95	8.68
	E	4	22.11	0.308	0.009	0.005	44.7	58.2	43.43	3.32
	F	5	36.16	0.092	0.002	0.012	36.3	66.4	65.84	12.62
	G	5	35.13	0.112	0.003	0.010	24.1	76.3	40.40	8.88
	H	6	26.44	0.157	0.002	0.011	35.9	90.2	47.71	9.72
	I	7	61.38	0.082	0.002	0.027	24.8	97.4	76.82	13.96
Xi	J	8	53.78	0.029	0.001	0.016	51.6	100.0	157.51	35.16
	Integrated age ± 2s			1.130	0.003			K2O=0.08%	55.89	11.13
	Plateau ± 2s		steps B-I	1.069	0.004±0.004			94.6	45.03	6.19
	Isochron±2s		steps B-I		$^{40}Ar/^{36}Ar$=	316.3±26.5			38.86	8.36
	Cp 1813 92, plag (cloudy), 10.52 mg, J=0.0023657±0.09%, D=1.006±0.001, NM-231F, Lab#=59511-01									
Xi	A	1	4933.4	0.132	1.1	0.010	0.0	0.1	-8.35	92.87
Xi	B	1	1199.6	0.784	1.2	0.009	1.6	0.4	79.19	20.69
	C	1	460.5	1.041	0.63	0.008	2.5	1.0	47.81	8.46
	D	1	118.4	2.893	0.64	0.003	5.8	2.4	29.26	2.23
	E	1	69.66	3.454	0.38	0.001	10.4	4.1	30.54	1.30
	F	2	59.17	2.716	0.20	0.001	12.7	5.4	31.81	1.23
	G	2	74.60	5.94	0.14	0.002	10.5	8.3	33.35	1.31
	H	4	45.59	28.93	0.52	0.001	16.8	22.5	32.40	0.74
	I	4	42.33	25.52	0.69	0.001	18.6	35.1	33.23	0.71
	J	5	32.55	20.92	0.67	0.001	23.6	45.3	32.47	0.52
	K	5	30.72	26.36	0.92	0.001	25.7	58.3	33.41	0.47
	L	6	32.26	48.8	1.0	0.001	24.6	82.3	33.54	0.48
	M	7	29.74	36.14	0.95	0.002	26.8	100.0	33.66	0.46
	Integrated age ± 2s			203.6	0.66			K2O=3.14%	33.32	1.43
	Plateau ± 2s		steps C-M	202.7	0.80 ±0.58			99.6	33.09	0.53
	Isochron±2s		steps C-M		$^{40}Ar/^{36}Ar$=	294.7±1.8			33.43	0.85

	Cp 1813 92', Biotite, 1.6 mg, J=0.0023685±0.09%, D=1.006±0.001, NM-231F, Lab#=59512-01									
X	A	1	124.1	0.118	0.63	0.025	2.4	1.0	12.45	6.41
X	B	1	87.26	0.289	0.78	0.012	6.6	3.4	24.60	3.98
X	C	1	78.71	0.263	1.2	0.012	13.4	5.5	44.42	3.16
X	D	1	61.01	0.683	2.3	0.009	23.1	11.1	59.33	2.00
X	E	2	33.09	1.301	2.9	0.007	49.1	21.9	68.10	0.73
X	F	2	26.19	1.136	4.0	0.007	62.3	31.2	68.41	0.73
	G	2	23.42	2.678	3.4	0.006	74.3	53.3	72.90	0.38
	H	2	23.91	1.579	2.7	0.006	71.0	66.3	71.08	0.51
	I	3	21.79	4.094	1.9	0.007	80.7	100.0	73.64	0.29
	Integrated age ± 2s			12.14	2.3			K2O=1.23%	68.89	0.75
	Plateau ± 2s		steps G-I	8.351	2.526±1.546			68.8	72.98	1.31
	Isochron±2s		steps A-I		$^{40}Ar/^{36}Ar$=	261.4±3.1			75.36	0.50
	Core 1, Plag (Clear), 2.56 mg, J=0.0023702±0.09%, D=1.006±0.001, NM-231F, Lab#=59513-01									
	A	1	207.9	0.057	0.004	0.16	10.6	5.0	99.62	17.35
	B	2	38.25	0.082	0.002	0.016	27.1	12.2	55.13	12.90
	C	3	53.29	0.140	0.003	0.027	18.8	24.6	49.08	8.15
	D	4	146.9	0.151	0.002	0.039	6.7	37.8	48.63	12.18
	E	4	380.8	0.126	0.003	0.045	4.6	48.9	83.09	19.12
	F	5	56.63	0.093	0.002	0.039	21.2	57.1	60.12	12.41
	G	5	61.51	0.108	0.002	0.047	23.9	66.6	72.98	12.54
	H	6	57.37	0.124	0.002	0.034	17.3	77.5	50.53	10.92
	I	7	48.37	0.121	0.002	0.028	31.5	88.2	75.40	10.11
	J	8	45.76	0.134	0.004	0.015	24.4	100.0	52.21	7.12
	Integrated age ± 2s			1.137	0.002			K2O=0.07%	62.34	14.20
	Plateau ± 2s		steps A-J	1.137	0.003±0.002			100.0	59.12	8.81
	Isochron±2s		steps A-J		$^{40}Ar/^{36}Ar$=	300.9±6.2			53.06	7.52
	Core 1, Plag(Cloudy), 10.88 mg, J=0.0023718±0.09%, D=1.006±0.001, NM-231F, Lab#=59514-01									
Xi	A	1	2120.7	0.037	0.57	0.068	1.8	0.0	155.64	55.94
	B	1	629.3	0.376	0.81	0.010	1.5	0.2	40.55	12.66
	C	1	244.5	0.942	0.53	0.004	2.4	0.7	25.41	4.95
	D	1	191.9	1.960	0.37	0.005	4.5	1.7	36.42	3.45
	E	1	106.3	3.349	0.24	0.002	7.2	3.5	32.28	1.97
	F	2	106.2	5.51	0.27	0.002	7.4	6.4	33.57	1.83
	G	2	85.92	6.74	0.24	0.001	9.0	10.0	32.86	1.49
	H	3	51.72	16.03	0.22	0.001	15.2	18.4	33.34	0.82
	I	3	47.36	24.94	0.54	0.001	16.3	31.5	32.83	0.73
	J	4	44.05	18.57	0.44	0.001	17.2	41.3	32.07	0.70
	K	4	37.99	22.88	0.68	0.001	20.8	53.3	33.59	0.64
	L	5	33.50	29.25	1.4	0.001	23.8	68.7	33.80	0.52
	M	5	31.95	27.07	1.9	0.001	24.4	82.9	33.08	0.48
	N	6	38.98	25.75	1.7	0.002	21.0	96.5	34.65	0.62
Xi	O	7	44.16	6.71	2.2	0.002	19.0	100.0	35.54	0.80
	Integrated age ± 2s			190.1	0.59			K2O=2.83%	33.47	1.45
	Plateau ± 2s		steps B-N	183.4	0.99 ±1.16			96.4	33.37	0.48
	Isochron±2s		steps B-N		$^{40}Ar/^{36}Ar$=	295.1±1.4			33.55	0.84

	Core 1, Biotite, 1.82 mg, J=0.0023732±0.08%, D=1.006±0.001, NM-231F, Lab#=59515-01									
X	A	1	220.6	0.070	0.66	0.013	0.9	0.7	8.62	12.39
X	B	1	83.84	0.180	0.62	0.008	3.6	2.5	12.82	4.51
X	C	1	126.9	0.210	0.87	0.012	3.8	4.5	20.57	4.99
X	D	1	114.1	0.379	1.5	0.010	10.7	8.3	51.41	3.71
X	E	2	55.42	0.771	1.8	0.008	24.7	15.9	57.61	1.56
X	F	2	36.97	1.105	4.2	0.006	41.7	26.7	64.81	0.95
X	G	2	27.37	1.331	3.6	0.007	57.9	39.8	66.58	0.65
	H	2	35.01	2.382	2.6	0.008	48.3	63.3	71.05	0.63
	I	2	35.35	1.249	1.9	0.009	48.2	75.6	71.54	0.77
	J	3	28.72	2.481	1.4	0.008	60.8	100.0	73.29	0.47
	Integrated age ± 2s			10.16	1.9			K2O=0.90%	66.17	1.15
	Plateau ± 2s		steps H-J	6.113	1.980±1.258			60.2	72.29	1.47
	Isochron±2s		steps A-J		$^{40}Ar/^{36}Ar$=	268.2±3.0			75.93	0.89
	Felsic Core, plag, 6.9 mg, J=0.0023751±0.07%, D=1.006±0.001, NM-231F, Lab#=59516-01									
Xi	A	1	160.1	1.058	0.053	0.050	6.4	1.8	43.58	3.87
	B	2	60.38	2.800	0.036	0.009	13.6	6.7	35.20	1.56
	C	3	46.08	6.63	0.071	0.006	17.2	18.1	33.75	0.91
	D	4	27.11	6.96	0.065	0.003	30.0	30.2	34.67	0.57
	E	4	26.68	8.58	0.11	0.002	30.6	45.0	34.76	0.51
	F	5	24.32	9.30	0.14	0.001	32.5	61.1	33.68	0.43
	G	5	36.25	3.391	0.065	0.002	21.1	66.9	32.66	0.94
	H	6	28.77	14.92	0.18	0.002	28.4	92.7	34.78	0.45
	I	7	31.28	3.618	0.087	0.004	26.3	99.0	35.05	0.84
	J	8	57.00	0.592	0.15	0.006	14.5	100.0	35.26	2.66
	Integrated age ± 2s			57.9	0.093			K2O=1.36%	34.55	1.04
	Plateau ± 2s		steps B-J	56.8	0.12 ±0.10			98.2	34.34	0.46
	Isochron±2s		steps B-J		$^{40}Ar/^{36}Ar$=	295.6±4.2			34.32	1.33
	Felsic Core, wr, 8.21 mg, J=0.0023757±0.07%, D=1.006±0.001, NM-231F, Lab#=59517-01									
Xi	A	1	28.38	9.52	9.1	0.002	26.1	4.0	31.41	0.52
Xi	B	2	12.32	39.60	3.3	0.000	62.3	20.5	32.55	0.14
	C	3	9.933	55.2	2.8	0.000	78.1	43.5	32.94	0.09
	D	4	9.601	38.27	2.9	0.000	81.3	59.5	33.11	0.09
	E	4	9.208	29.15	2.1	0.000	84.5	71.6	33.01	0.09
	F	5	8.783	27.21	4.3	0.000	88.7	83.0	33.06	0.08
Xi	G	5	8.933	17.34	8.2	0.000	87.8	90.2	33.26	0.10
Xi	H	6	9.369	16.20	19.4	0.001	84.6	97.0	33.62	0.11
Xi	I	7	9.730	4.297	10.9	0.000	78.7	98.8	32.50	0.24
Xi	J	8	10.45	2.944	18.1	0.001	73.8	100.0	32.73	0.32
	Integrated age ± 2s			239.8	3.4			K2O=4.72%	32.92	0.18
	Plateau ± 2s		steps C-F	149.9	3.0 ±1.8			62.5	33.03	0.10
	Isochron±2s		steps C-F		$^{40}Ar/^{36}Ar$=	290.7±13.4			33.13	0.32

	Cp 1813 2070', plag, 11.15 mg, J=0.0023754±0.07%, D=1.006±0.001, NM-231F, Lab#=59518-01									
X	A	1	511.2	0.076	0.58	0.38	19.4	0.1	381.80	15.66
X	B	1	178.3	0.394	0.53	0.11	23.0	0.4	167.78	4.27
X	C	1	112.3	0.589	0.30	0.065	24.3	0.8	113.49	2.82
X	D	1	71.97	0.879	0.29	0.039	27.0	1.5	81.63	1.66
X	E	1	51.95	1.399	0.22	0.029	35.4	2.6	77.23	1.11
X	F	2	42.84	4.086	0.23	0.019	36.2	5.9	65.42	0.74
X	G	3	27.63	10.71	0.34	0.012	45.2	14.4	52.72	0.37
X	H	3	19.85	12.28	0.33	0.007	55.0	24.1	46.21	0.31
X	I	4	17.89	15.48	0.32	0.006	59.2	36.4	44.84	0.24
X	J	4	17.63	17.55	0.35	0.006	60.1	50.3	44.87	0.21
X	K	5	15.41	23.87	0.30	0.006	66.2	69.2	43.23	0.19
X	L	6	14.66	35.89	0.35	0.006	69.6	97.6	43.20	0.15
X	M	7	14.29	3.034	0.30	0.007	75.4	100.0	45.61	0.43
	Integrated age ± 2s			126.2	0.32			K2O=1.83%	47.13	0.43
	Plateau ± 2s		no plateau	0.000	0.000±0.000			0.0	0.00	0.00
	Isochron±2s		steps A-M		$^{40}Ar/^{36}Ar$=		361.6±2.3		38.69	0.30
	Cp 1813 2070', K-spar, J=0.0023743±0.06%, D=1.006±0.001, NM-231F, Lab#=59519-05									
Xi	A	1	39.31	1.880	2.7	0.010	32.1	10.2	53.30	0.79
Xi	B	1	14.40	0.817	3.6	0.001	57.6	14.7	35.15	0.77
Xi	C	2	13.96	2.463	5.5	0.003	65.6	28.1	38.80	0.32
Xi	D	2	14.07	1.399	7.6	0.003	64.7	35.7	38.55	0.51
	E	2	13.80	3.061	7.5	0.004	69.2	52.3	40.41	0.28
	F	2	14.32	2.952	5.1	0.004	68.4	68.4	41.46	0.27
	G	2	14.24	4.151	5.1	0.004	69.8	90.9	42.07	0.25
Xi	H	3	14.78	0.973	5.6	0.006	69.5	96.2	43.48	0.64
Xi	I	3	15.04	0.189	5.6	0.007	60.9	97.3	38.80	2.47
Xi	J	4	15.21	0.502	5.0	0.005	61.7	100.0	39.76	1.06
	Integrated age ± 2s			18.39	5.0				41.81	0.41
	Plateau ± 2s		steps E-G	10.16	5.8 ±2.8			55.3	41.37	0.97
	Isochron±2s		steps E-G		$^{40}Ar/^{36}Ar$=		758.4±588.5		12.61	7.89

Notes:

Isotopic ratios corrected for blank, radioactive decay, and mass discrimination, not corrected for interfering reactions.

Errors quoted for individual analyses include analytical error only, without interfering reaction or J uncertainties.

Integrated age calculated by summing isotopic measurements of all steps.

Integrated age error calculated by quadratically combining errors of isotopic measurements of all steps.

Plateau age is inverse-variance-weighted mean of selected steps.

Plateau age error is inverse-variance-weighted mean error (Taylor, 1982) times root MSWD where MSWD>1.

Plateau error is weighted error of Taylor (1982).

Decay constants and isotopic abundances after Steiger and Jäger (1977).

symbol preceding sample ID denotes analyses excluded from plateau age calculations.

Ages calculated relative to FC-2 Fish Canyon Tuff sanidine interlaboratory standard at 28.02 Ma

Decay Constant (LambdaK (total)) = 5.543e-10/a

Correction factors:

$(^{39}Ar/^{37}Ar)_{Ca}$ = 0.0007 ± 5e-05

$(^{36}Ar/^{37}Ar)_{Ca}$ = 0.00028 ± 2e-05

$(^{38}Ar/^{39}Ar)_{K}$ = 0.013

$(^{40}Ar/^{39}Ar)_{K}$ = 0.01 ± 0.002

E.1.2 Step-heating Spectra

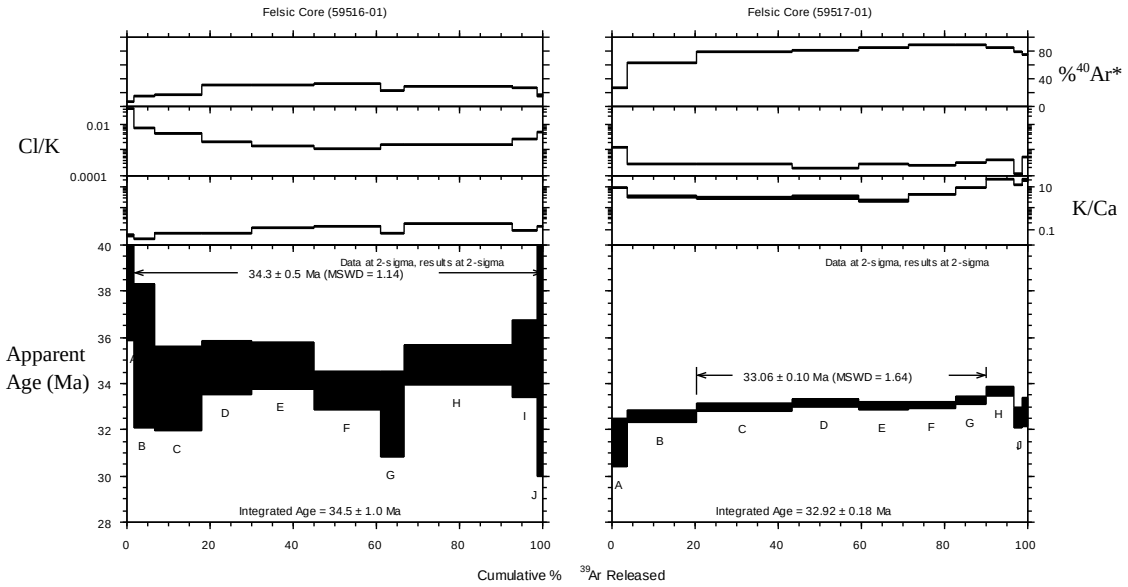

Figure E-1: Step-heating spectra for Felsic core

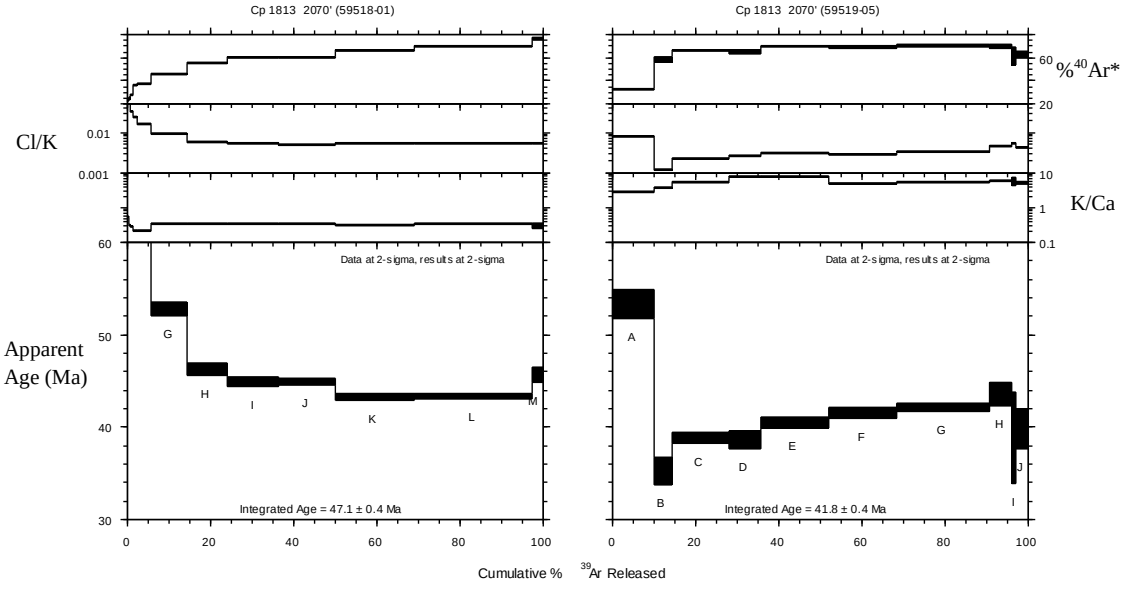

Figure E-2: Step-heating spectra for Cp1813 2070’

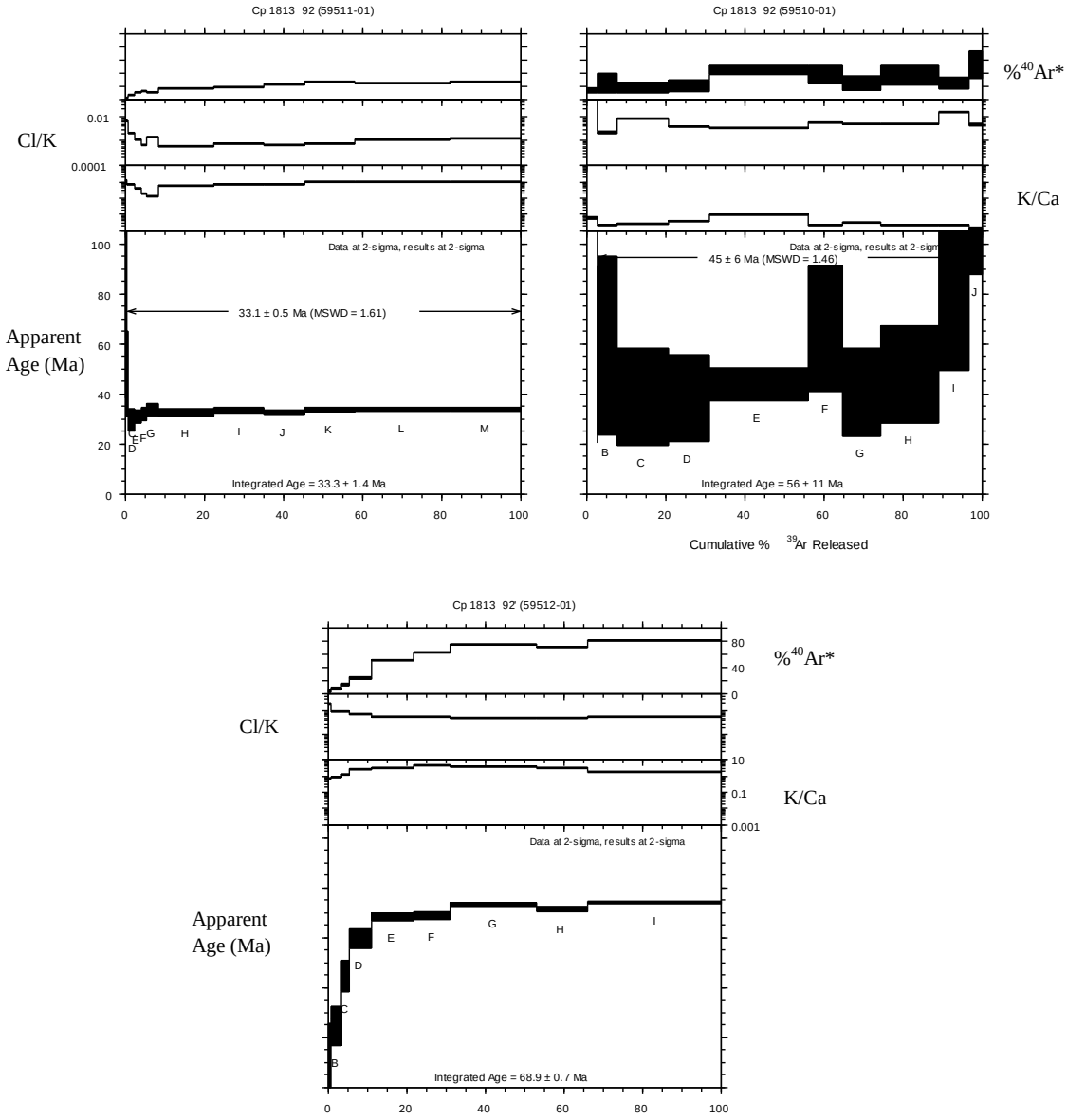

Figure E-3: Step-heating spectra for Cp1813 92’

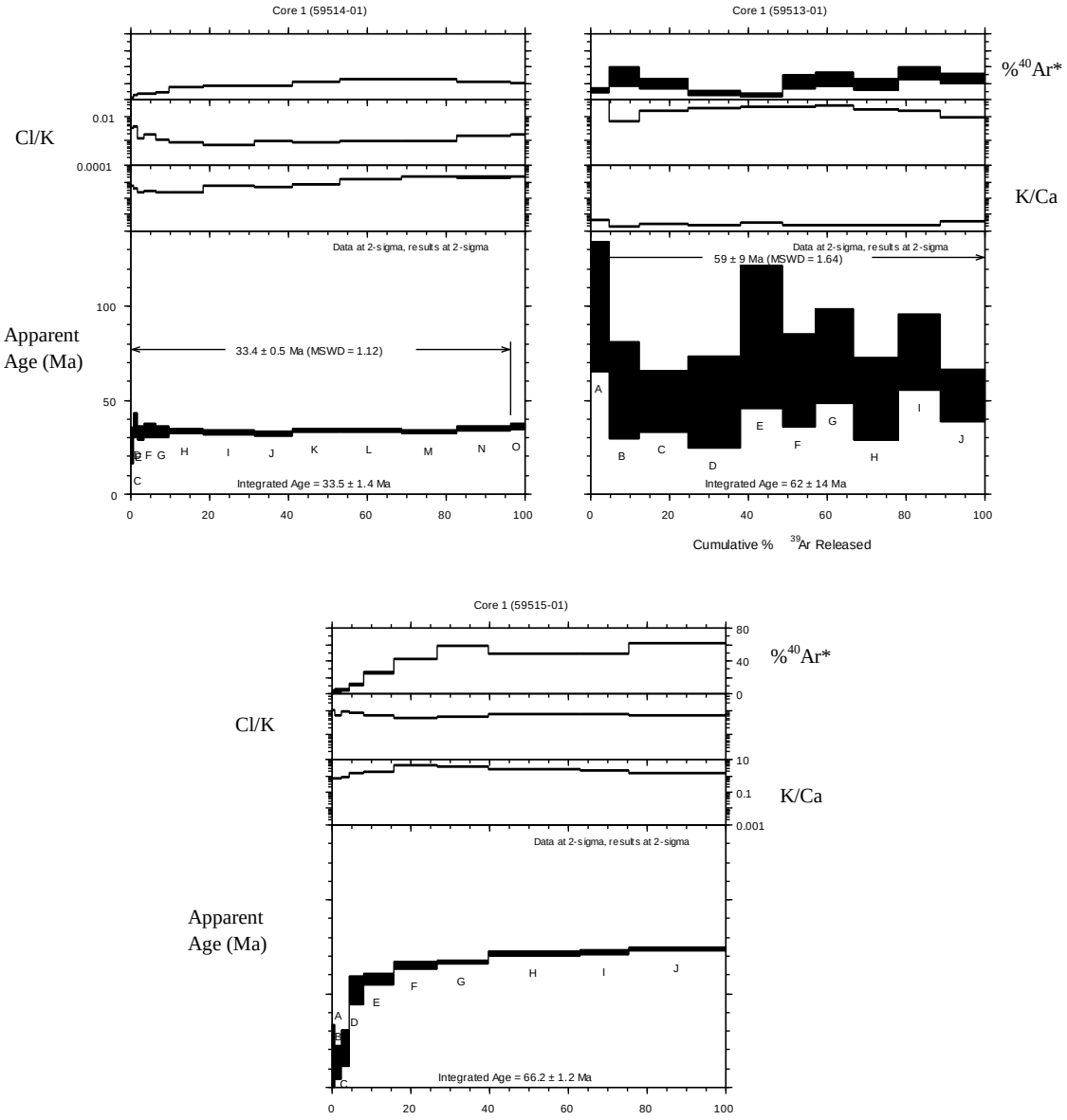

Figure E-4: Step-heating spectra for Core 1

E.1.3 Isochrons

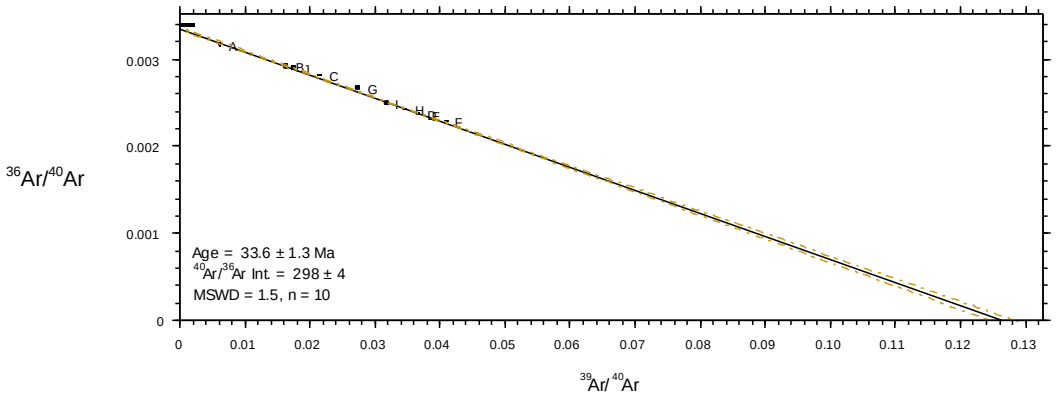

Figure E-5: Inverse Isochron for Run 59516-01 (Felsic Core, plagioclase)

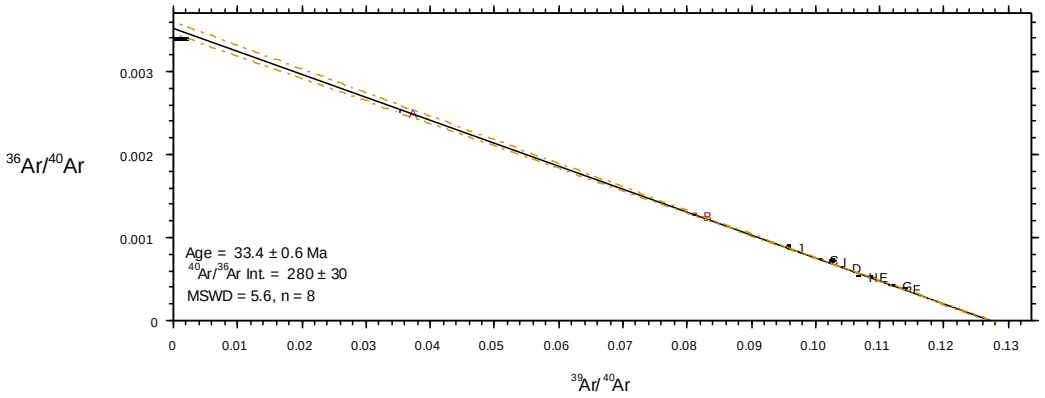

Figure E-6: Inverse Isochron for Run 59517-01 (Felsic Core, groundmass)

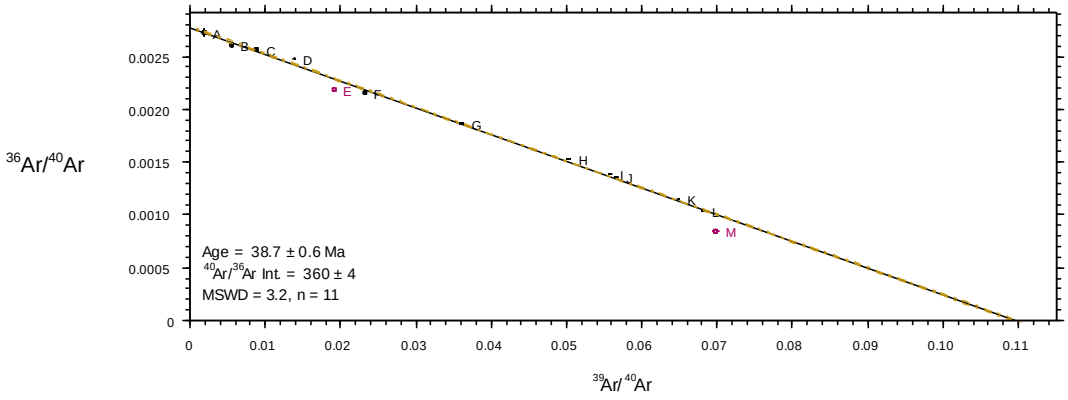

Figure E-7: Inverse Isochron for Run 59518-01 (Cp 1813 2070', plagioclase)

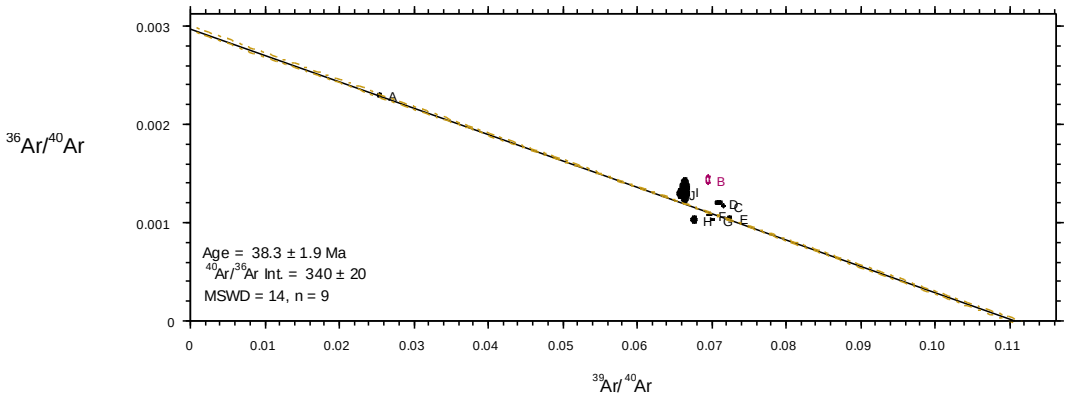

Figure E-8: Inverse Isochron for Run 59519-05 (Cp 1813 2070', K-feldspar)

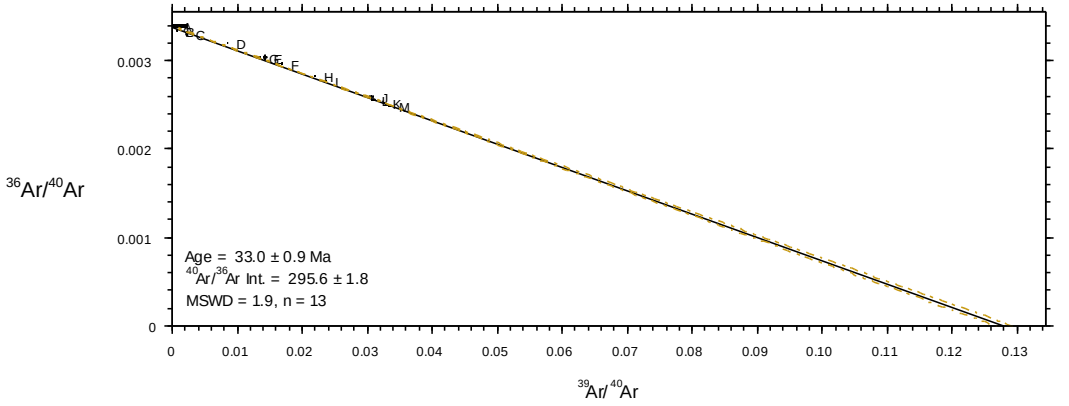

Figure E-9: Inverse Isochron for Run 59511-01 (Cp 1813 92', cloudy plagioclase)

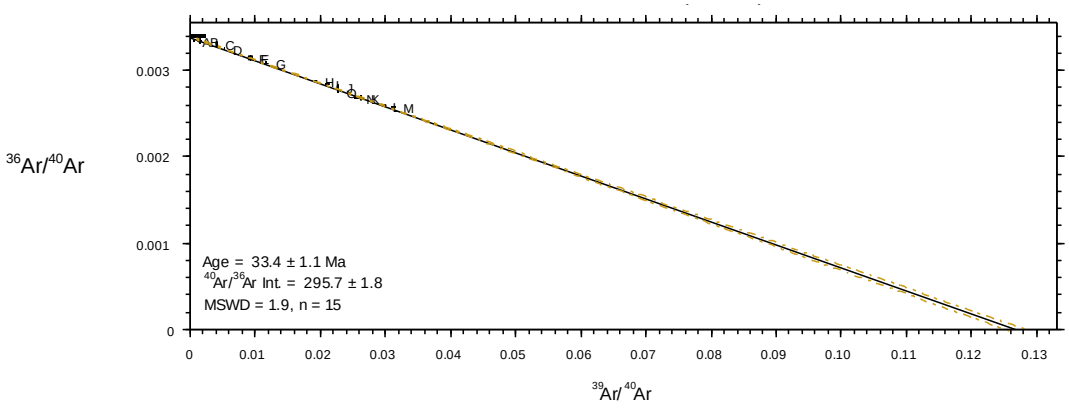

Figure E-10: Inverse Isochron for Run 59514-01 (Core 1, cloudy plagioclase)

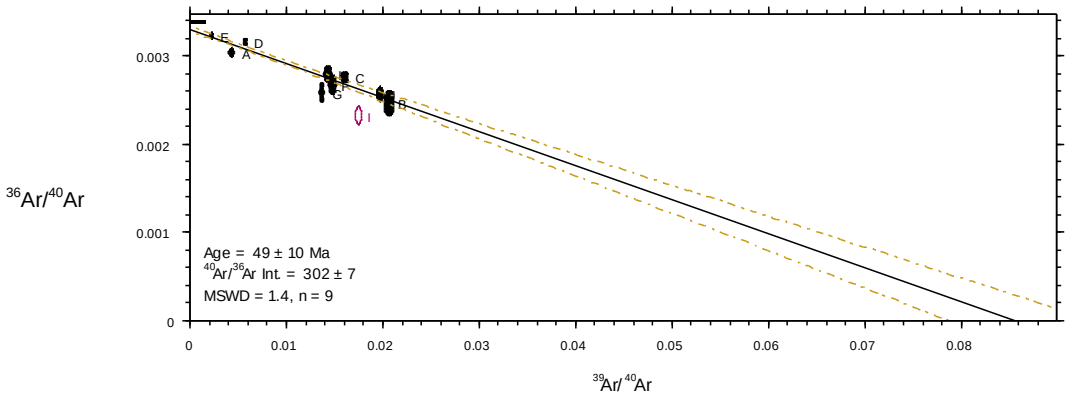

Figure E-11: Inverse Isochron for Run 59513-01 (Core 1, clear plagioclase)

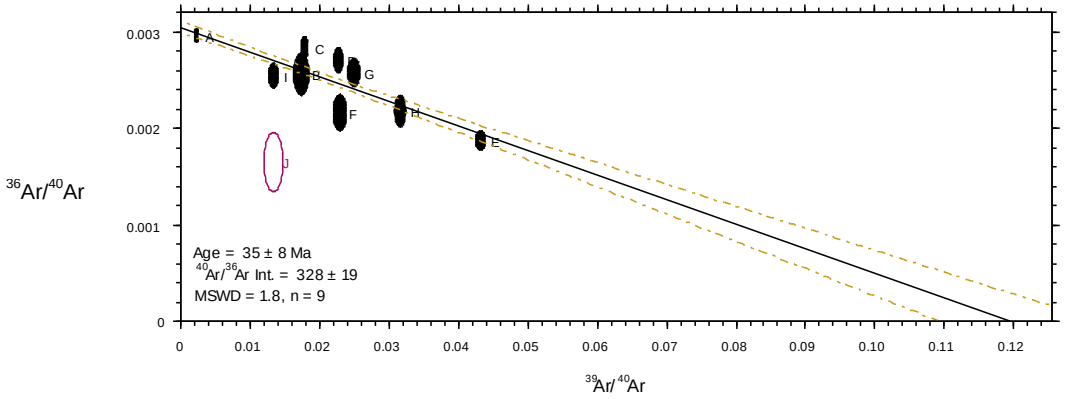

Figure E-12: Inverse Isochron for Run 59510-01 (Cp 1813 92', clear plagioclase)

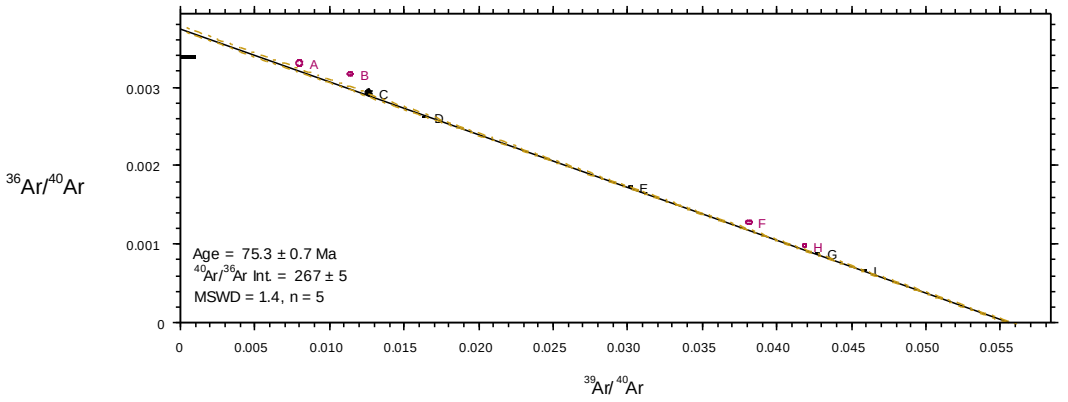

Figure E-13: Inverse Isochron for Run 59512-01 (Cp 1813 92', biotite)

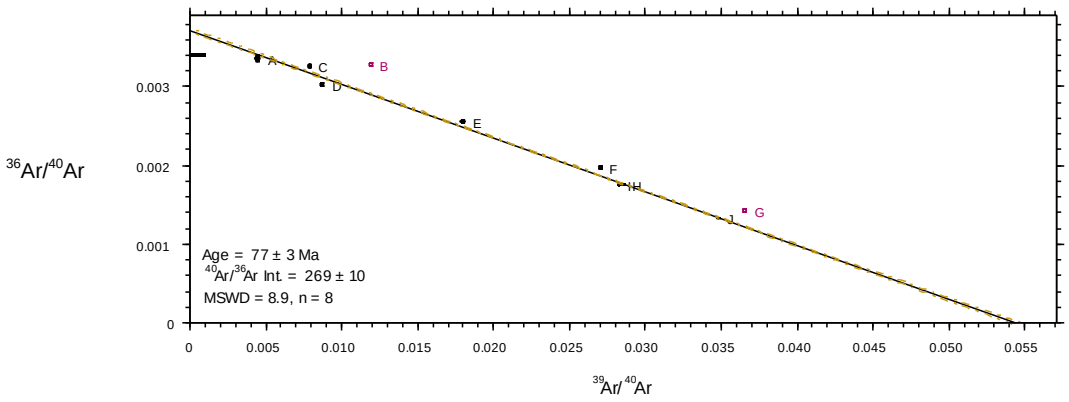

Figure E-14: Inverse Isochron for Run 59515-01 (Core 1, biotite)

E.2 Manganese Oxides Data

The detector used for the manganese oxide samples was the Multiplier with a sensitivity of $4.61e^{-17}$ moles/pA and discrimination of 1.002 ± 0.001.

E.2.1 Data Tables

Table E-2: Argon isotopic data for manganese oxide separates.

	ID	Power	40Ar/39Ar	37Ar/39Ar	36Ar/39Ar	39ArK	K/Ca	Cl/K	40Ar*	39Ar	Age	±1σ
		(Watts)			(x 10-3)	(x 10-15 mol)			(%)	(%)	(Ma)	(Ma)
	SE-PKM-1 vein A , cryptomelane, 4.92 mg, J=0.0016418±0.12%, D=1.002±0.001, NM-236H, Lab#=59771-01											
Xi	A	2	118.3	0.2470	397.2	1.37	2.1	0.22	0.8	6.2	2.8	1.9
	B	3	40.31	0.3047	133.2	1.57	1.7	0.091	2.4	13.3	2.91	0.78
	C	4	22.47	0.2223	66.09	3.16	2.3	0.032	13.1	27.6	8.71	0.45
	D	5	16.82	0.1989	45.77	5.41	2.6	0.015	19.6	52.1	9.75	0.26
	E	6	21.05	0.2061	59.94	3.81	2.5	0.014	15.9	69.3	9.89	0.35
	F	7	28.33	0.2071	85.83	4.54	2.5	0.018	10.5	89.9	8.78	0.45
	G	8	101.2	0.3826	335.2	0.985	1.3	0.063	2.2	94.3	6.5	2.0
Xi	H	9	164.5	0.5440	546.9	0.541	0.94	0.12	1.8	96.8	8.5	3.0
Xi	I	10	201.3	0.7224	676.5	0.405	0.71	0.14	0.7	98.6	4.2	3.5
Xi	J	11	240.3	0.8858	817.3	0.307	0.58	0.19	-0.5	100.0	-3.3	5.4
	Integrated age ± 2s			n=10	MSWD=10.57	22.1	2.0		K2O=1.05%		8.1	1.0
	Plateau ± 2s	steps B-G		n=6	MSWD=15.42	19.5	2.3 ±1.0			88.1	9.1	1.3
	Isochron±2s	steps B-G		n=6	MSWD=10.50		40Ar/36Ar=		284.7±3.6		11.17	0.73

	SE-PKM-1 vein A hard, cryptomelane, 5.18 mg, J=0.0016479±0.13%, D=1.002±0.001, NM-236H, Lab#=59772-(											
Xi	A	2	262.6	0.2440	895.3	0.340	2.1	0.33	-0.7	1.9	-5.8	4.9
Xi	B	3	92.03	0.2694	309.8	0.613	1.9	0.16	0.6	5.3	1.5	1.8
	C	4	58.59	0.3318	192.1	0.584	1.5	0.12	3.2	8.5	5.5	1.8
	D	5	40.18	0.2937	126.2	0.859	1.7	0.070	7.2	13.2	8.6	1.1
	E	6	29.43	0.2470	89.28	1.46	2.1	0.040	10.4	21.3	9.08	0.82
	F	7	19.42	0.2039	54.72	4.79	2.5	0.018	16.8	47.7	9.65	0.33
	G	8	27.26	0.2387	81.07	3.35	2.1	0.021	12.2	66.2	9.85	0.50
	H	9	37.08	0.2776	114.5	2.56	1.8	0.025	8.8	80.3	9.68	0.54
	I	10	50.59	0.3349	159.8	1.97	1.5	0.031	6.7	91.2	10.04	0.86
	J	11	62.14	0.4140	199.5	1.60	1.2	0.040	5.2	100.0	9.5	1.1
	Integrated age ± 2s			n=10	MSWD=3.98	18.1	1.9		K2O=0.82%		8.93	0.99
	Plateau ± 2s		steps C-J	n=8	MSWD=1.03	17.2	2.0	±0.8		94.7	9.57	0.44
	Isochron±2s		steps C-J	n=8	MSWD=1.09		40Ar/36Ar=		294.1±3.6		9.9	1.0
	SE-PKM-1 cluster D, cryptomelane, 5.09 mg, J=0.0016496±0.14%, D=1.002±0.001, NM-236H, Lab#=59773-01											
Xi	A	2	35.86	0.2908	119.3	2.12	1.8	0.10	1.8	4.9	1.91	0.72
Xi	B	3	13.89	0.2595	40.54	1.99	2.0	0.063	13.9	9.5	5.72	0.41
Xi	C	4	7.131	0.2413	14.37	2.72	2.1	0.027	40.7	15.8	8.60	0.23
	D	5	5.188	0.2179	6.008	8.94	2.3	0.006	66.1	36.5	10.155	0.090
	E	6	5.113	0.2073	5.448	11.6	2.5	0.003	68.8	63.2	10.419	0.073
	F	7	6.605	0.2372	10.61	12.6	2.2	0.003	52.8	92.3	10.329	0.088
	G	8	21.75	0.3602	62.52	2.09	1.4	0.008	15.1	97.1	9.78	0.48
	H	9	49.70	0.6670	155.4	0.662	0.76	0.020	7.7	98.7	11.4	1.2
Xi	I	10	80.23	1.154	253.0	0.342	0.44	0.036	6.9	99.5	16.5	2.1
Xi	J	11	104.0	1.691	334.4	0.229	0.30	0.055	5.1	100.0	15.7	3.7
	Integrated age ± 2s			n=10	MSWD=36.49	43.2	2.0		K2O=1.98%		9.65	0.22
	Plateau ± 2s		steps D-H	n=5	MSWD=1.82	35.8	2.2	±1.4		82.9	10.31	0.13
	Isochron±2s		steps D-H	n=5	MSWD=2.40		40Ar/36Ar=		295.3±3.9		10.32	0.13
	SE-PKM-1 cluster E, cryptomelane, 5.36 mg, J=0.0016448±0.07%, D=1.002±0.001, NM-236H, Lab#=59774-01											
Xi	A	2	80.16	0.6869	271.1	1.04	0.74	0.43	0.1	1.9	0.4	1.4
Xi	B	3	37.98	0.6078	125.1	1.83	0.84	0.30	2.8	5.3	3.20	0.74
Xi	C	4	19.17	0.6285	57.31	2.51	0.81	0.21	12.0	9.9	6.79	0.44
Xi	D	5	9.187	0.5958	21.50	3.82	0.86	0.11	31.4	16.9	8.54	0.20
Xi	E	6	6.141	0.4716	9.804	6.73	1.1	0.048	53.4	29.3	9.70	0.10
	F	7	5.394	0.4047	6.539	17.1	1.3	0.028	64.8	60.8	10.322	0.057
	G	8	5.808	0.4128	7.904	10.4	1.2	0.026	60.3	79.9	10.353	0.082
	H	9	7.342	0.4209	12.89	6.17	1.2	0.023	48.6	91.3	10.54	0.14
	I	10	10.81	0.4427	24.39	3.20	1.2	0.023	33.6	97.2	10.75	0.24
Xi	J	11	19.58	0.4966	52.82	1.54	1.0	0.028	20.4	100.0	11.84	0.50
	Integrated age ± 2s			n=10	MSWD=35.15	54.3	1.1		K2O=2.37%		9.62	0.20
	Plateau ± 2s		steps F-I	n=4	MSWD=1.54	36.9	1.2	±0.1		67.8	10.37	0.11
	Isochron±2s		steps F-I	n=4	MSWD=0.06		40Ar/36Ar=		304.5±8.7		10.15	0.22

	SE-bulk big A, todorokite, 6.76 mg, J=0.0016387±0.12%, D=1.002±0.001, NM-236H, Lab#=59775-01											
	A	2	216.1	2.056	730.1	1.58	0.25	0.23	0.2	8.5	1.5	2.9
	B	3	108.5	2.118	363.6	2.99	0.24	0.19	1.1	24.5	3.6	1.5
	C	4	51.05	4.137	172.5	3.06	0.12	0.19	0.9	40.9	1.29	0.80
	D	5	25.54	11.46	88.51	2.72	0.045	0.18	1.3	55.5	1.00	0.55
	E	6	17.25	11.69	59.71	2.25	0.044	0.16	3.3	67.6	1.70	0.54
	F	7	10.07	11.46	35.30	3.02	0.045	0.14	5.8	83.8	1.74	0.39
	G	8	8.242	10.79	28.24	1.50	0.047	0.13	9.6	91.8	2.35	0.43
	H	9	16.02	10.55	53.64	0.790	0.048	0.11	6.5	96.1	3.08	0.81
	I	10	33.76	9.429	114.3	0.459	0.054	0.10	2.3	98.5	2.3	1.5
	J	11	76.61	6.593	257.8	0.273	0.077	0.12	1.3	100.0	2.9	2.8
	Integrated age ± 2s			n=10	MSWD=0.92	18.6	0.066		K2O=0.65%		2.0	1.4
	Plateau ± 2s		steps A-J	n=10	MSWD=0.92	18.6	0.11 ±0.16			100.0	1.87	0.42
	Isochron±2s		steps A-J	n=10	MSWD=1.14		40Ar/36Ar=		295.4±1.8		1.88	0.46
	SE-PGE fingers A, todorokite, 1.99 mg, J=0.001637±0.16%, D=1.002±0.001, NM-236H, Lab#=59776-01											
	A	2	164.4	3.408	546.2	0.554	0.15	0.50	2.0	25.1	9.9	2.8
	B	3	23.97	3.270	77.18	0.613	0.16	0.60	6.1	52.8	4.3	1.1
	C	4	15.38	5.363	47.01	0.578	0.095	0.37	12.6	79.0	5.75	0.93
	D	5	14.03	5.256	45.57	0.262	0.097	0.33	7.2	90.8	3.0	1.6
	E	6	11.68	4.187	45.52	0.120	0.12	0.41	-12.1	96.3	-4.2	3.7
	F	7	14.04	3.788	42.04	0.107	0.13	0.55	14.0	101.1	5.8	4.0
	G	8	-0.0891	12.34	13.26	0.007	0.041	3.0	2813.9	101.5	-8.3	59.6
	H	9	26.60	-9.3736	-34.6886	-0.006	-	-2.359	135.0	101.2	102.3	69.6
Xi	I	10	26.67	-3.4293	-73.1894	-0.010	-	-0.952	179.8	100.7	136.0	42.3
Xi	J	11	15.56	-1.0737	-8.4573	-0.017	-	-0.499	115.3	100.0	52.1	25.1
	Integrated age ± 2s			n=10	MSWD=2.98	2.21	0.12		K2O=0.26%		4.3	2.1
	Plateau ± 2s		steps A-H	n=8	MSWD=1.95	2.24	0.13 ±0.07			101.2	4.8	1.7
	Isochron±2s		steps A-H	n=8	MSWD=1.74		40Ar/36Ar=		299.1±4.0		4.0	1.3

Notes:

Isotopic ratios corrected for blank, radioactive decay, and mass discrimination, not corrected for interfering reactions

Errors quoted for individual analyses include analytical error only, without interfering reaction or J uncertainties.

Integrated age calculated by summing isotopic measurements of all steps.

Integrated age error calculated by quadratically combining errors of isotopic measurements of all steps.

Plateau age is inverse-variance-weighted mean of selected steps.

Plateau age error is inverse-variance-weighted mean error (Taylor, 1982) times root MSWD where MSWD>1.

Plateau error is weighted error of Taylor (1982).

Decay constants and isotopic abundances after Steiger and Jäger (1977).

symbol preceding sample ID denotes analyses excluded from plateau age calculations.

Weight percent K2O calculated from 39Ar signal, sample weight, and instrument sensitivity.

Ages calculated relative to FC-2 Fish Canyon Tuff sanidine interlaboratory standard at 27.84 Ma

Decay Constant (LambdaK (total)) = 5.543e-10/a

Correction factors:

(39Ar/37Ar)Ca = 0.0007 ± 5e-05

(36Ar/37Ar)Ca = 0.00028 ± 2e-05

(38Ar/39Ar)K = 0.013

(40Ar/39Ar)K = 0.01 ± 0.002

E.2.2 Step-heating Spectra

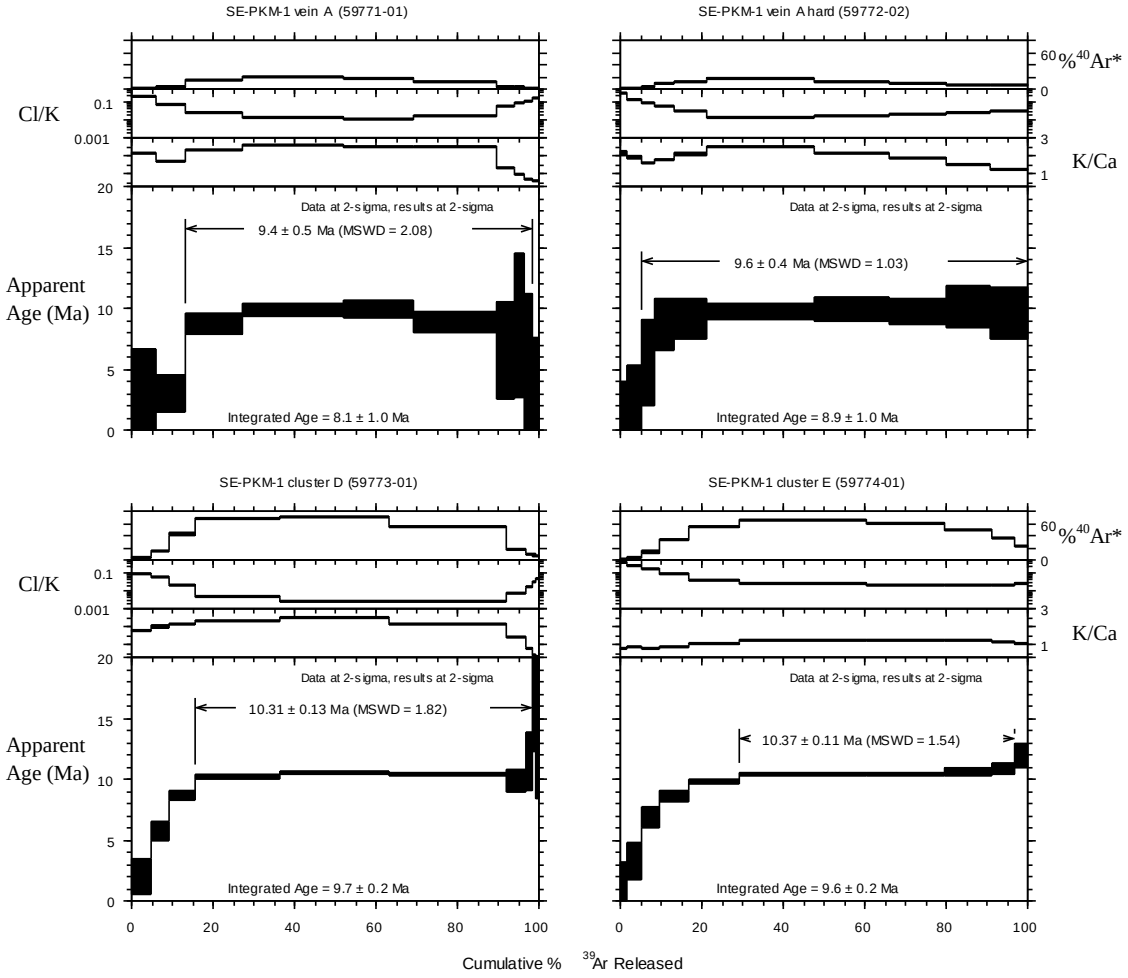

Figure E-15: Step-heating spectra for SE-PKM

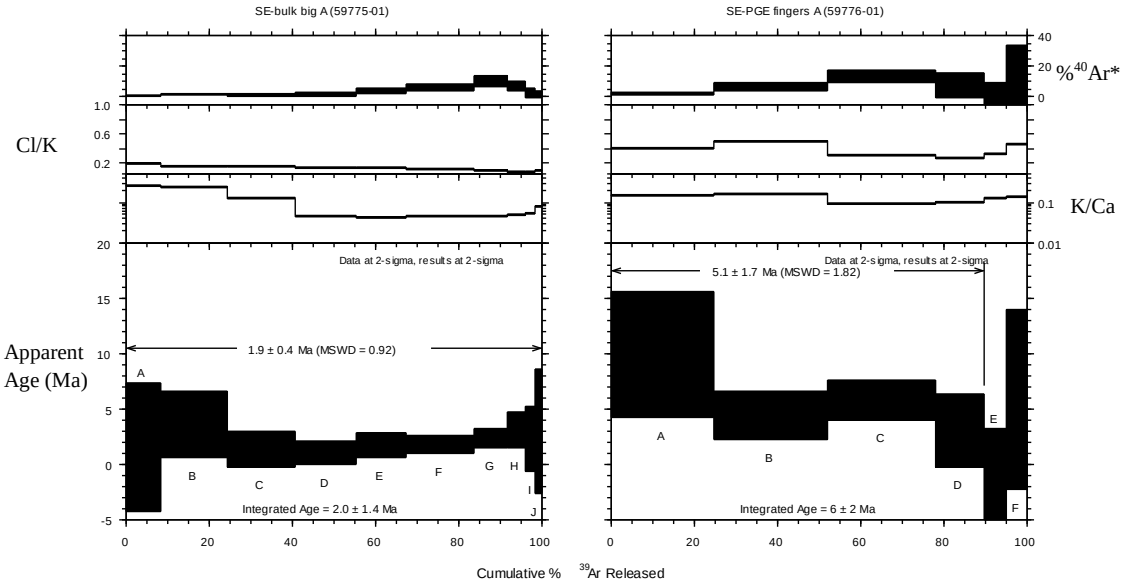

Figure E-16: Step-heating spectra from SE-bulk and SE-PGE

E.2.3 Isochrons

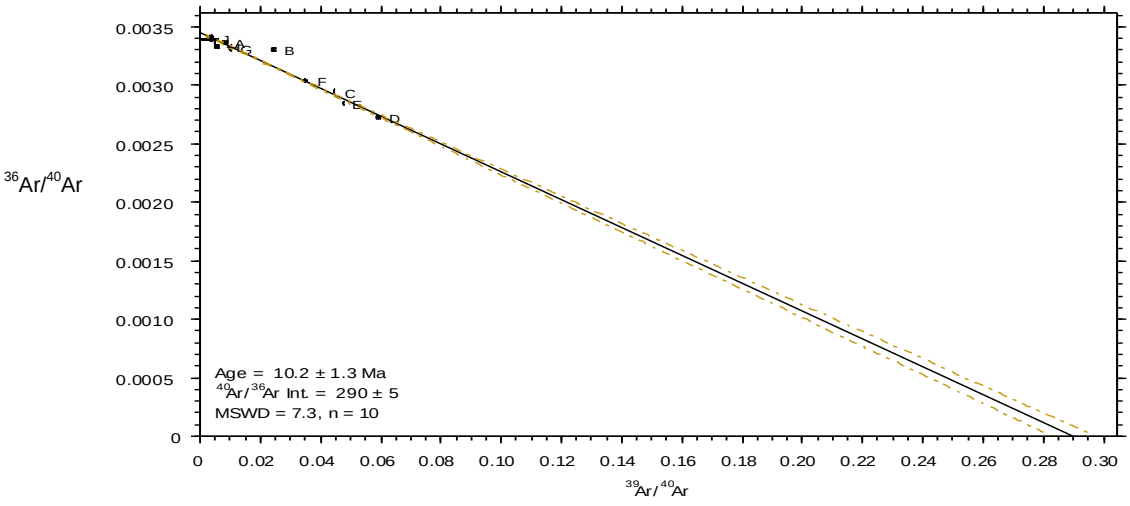

Figure E-17: Inverse isochron for SE-PKM-1 vein A

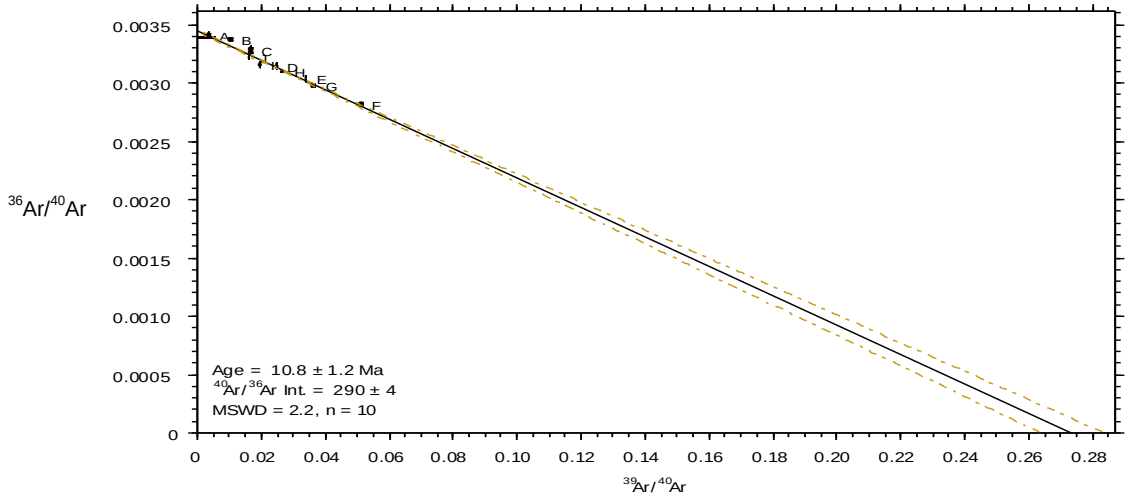

Figure E-18: Inverse isochron for SE-PKM-1 vein A (hard)

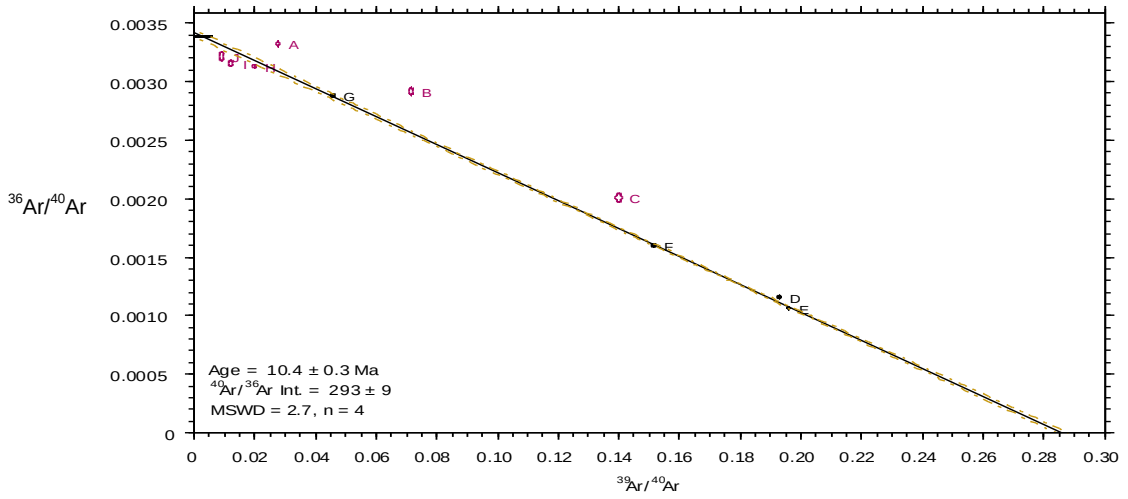

Figure E-19: Inverse isochron for SE-PKM-1 dendrite D

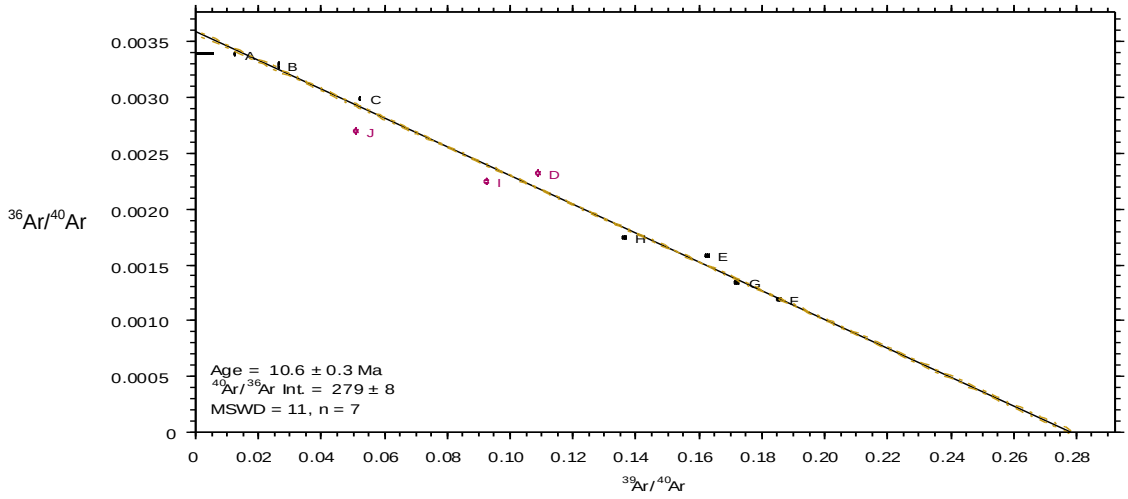

Figure E-20: Inverse isochron for SE-PKM-1 dendrite E

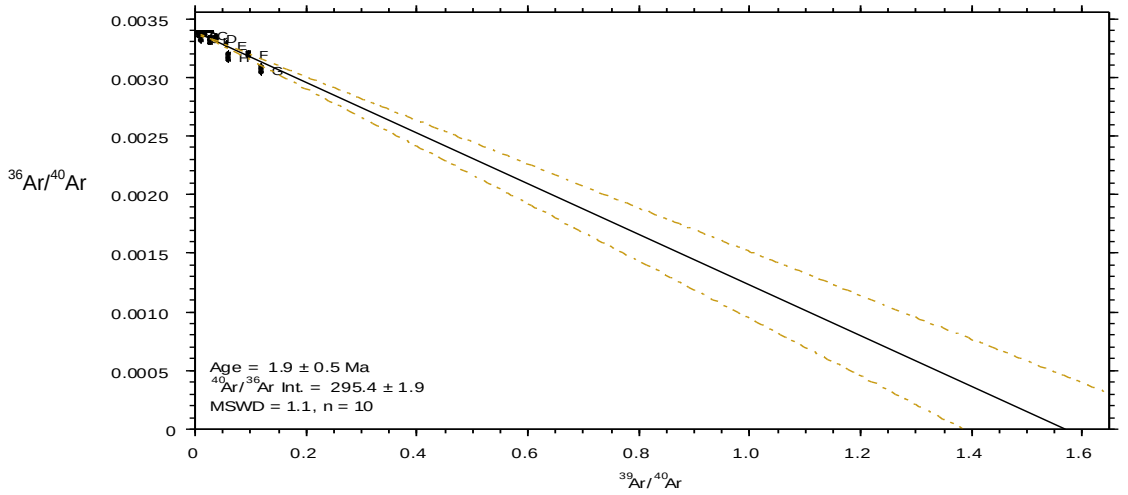

Figure E-21: Inverse isochron for SE-bulk

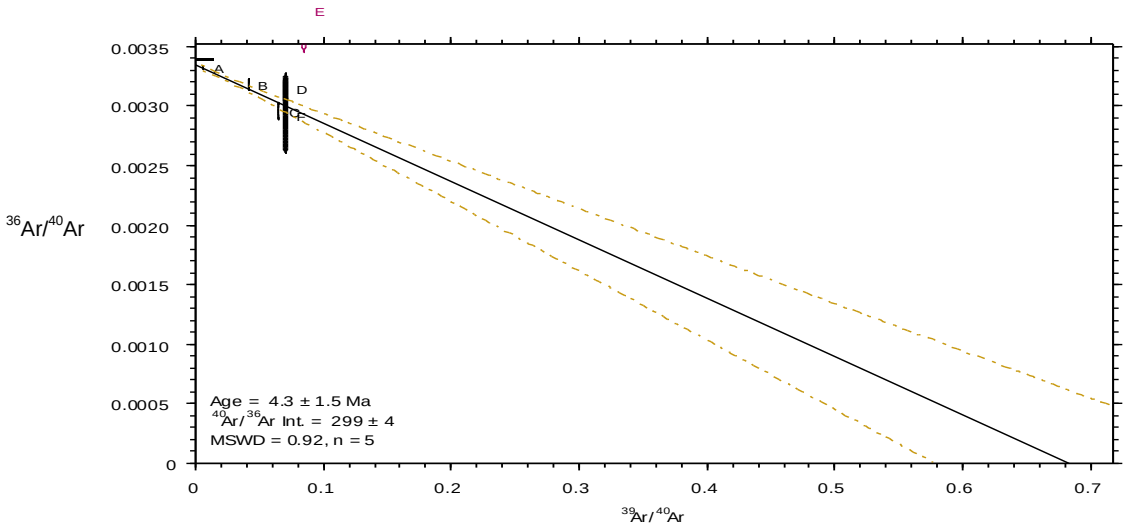

Figure E-22: Inverse isochron for SE-PGE

REFERENCES

Aguirre, E. F. d. J., 1987, Determinacion del sonamiento en las chimeneas de la Mina Buenna Tierra, a partir de los cocientes metalicos: Unpub. Professional thesis, Mexico, University of Guanajuato, 40 p.

Back, M. E., and Mandarino, J. A., 2008, Fleischer's Glossary of Mineral Species 2008: Tuscon, The Mineralogical Record Inc.

Benham, W. M., 1928a, LaCia. Minera 'LaVentura' S.A., Santa Eulalia, Chihuahua, Mexico, unpublished private report to American Smelting and Refining Co.

Benham, W. M., 1928b, Santo Domingo mine of the ASARCO, Santa Eulalia District, Chihuahua, Mexico, unpublished private report to American Smelting and Refining Co., p. 23.

Benham, W. M., 1929, The Parcionera Group, unpublished private report to American Smelting and Refining Co., p. 32.

Bish, D. L., and Post, J. E., 1989, Thermal behavior of complex, tunnel-structure manganese oxides: Am. Mineral, v. 74, p. 177-186.

Bond, B. R., 1986, Mineralogical and Geochemical Zoning, San Antonio Mine, Santa Eulalia Mining District, Chihuahua, Mexico: in Clark, K.F., Megaw, P.K.M., and Ruiz, J., eds., Lead-Zinc-Silver Carbonate -Hosted Deposits of northern Mexico: Society of Economic Geology Guidebook, Nov. 13-17, 1986, p. 233-254.

Bond, B. R., 1987, Selective trace element geochemistry, San Antonio Mine, Santa Eulalia, Chihuahua, Mexico: Unpub. M.S. thesis, University of Arizona, 193 p.

Burnham, C. W., 1959, Metallogenic Provinces of the southwestern United States and northern Mexico: New Mexico Bureau of Mines and Mineral Resources, Bulletin, v. 65, p. 75.

Burns, R. G., and Burns, V. M., 1979, Manganese oxides, *in* Ribbe, P. H., ed., Marine Mineral: Washington, DC, Mineral. Soc. Am., p. 1-46.

Campa, M. F., 1985, The Mexican Thrust Belt, *in* Howell, D. G., ed., Tectonostratigraphic Terranes of the Circum Pacific Region: Houston, Circum Pacific Council for Energy and Mineral Resources, p. 299-313.

Chafetz, H. S., Folk, R. L., and Milliken, K. L., 2004, Carbonate and Mn- and Fe-rich hot spring deposits, Belen (New Mexico, USA), Yellowstone National Park (Wyoming, USA), and northeastern Morocco: 32nd International Geological Congress: Italy, v. 32, part 2, p. 1472.

Chapin, C. E., and Lindley, J. I., 1986, Potassium metasomatism of igneous and sedimentary rocks in detachment terranes and other sedimentary basins: Economic implications: Arizona Geological Society Digest, v. 16, p. 118-126.

Chukhrov, F. V., Shanin, L. L., and Yermilova, L. P., 1966, Feasibility of absolute-age determination for potassium-carrying manganese minerals: Int. Geol. Rev., v. 8, p. 278-280.
Clark, K. F., Damon, P. E., Schutter, S. R., and Shafiqullah, M., 1979, Magmatismo en el Norte de Mexico en Relacion a los Yacimientos Metaliferos: Assoc. Ing. de Minas, Met. y Geol. de Mexico., Mem. Tec. XIII, p. 8-57.
Claypool, G. E., Holser, W. T., Kaplan, I. R., Sakai, A., and Zak, I., 1980, The Age Curves of S and O Isotopes in Marine Sulfate and their Mutual Interpretation: Chemical Geology, v. 28, p. 199-260.
Clemons, R. E., 1996, Cross section A through D. In: Kelly, R. W. (Ed.), New Mexico Geological Highway Map: New Mexico Geol. Soc., Socorro, New Mexico.
Clendenin, T. P., 1933, Report on geologic study of West Camp, Santa Eulalia District, unpublished private report to American Smelting and Refining Co., p. 72.
Crerar, D. A., Cormick, R. K., and Barnes, H. L., 1980, Geochemistry of manganese: an overview, in Varentsov, I. M., and Grassely, G., eds: Geology and geochemistry of manganese, v. 1: E. Schweizerbarst'sche Verlag, Stuttgart, p. 293-329.
Dahlgren, C. B., 1883, Historic mines of Mexico: private publication New York, p. 220.
Eggleston, T. L., Norman, D. I., Chapin, C. E., and Savin, S., 1983, Geology, alteration, and genesis of the Luis Lopez manganese district, New Mexico: in Chapin, C. E., and Callender, J. F. (eds.), Socorro region II: New Mexico Geological Society, Guidebook 34, p. 241-246.
Haynes, F. M., and Kesler, S. E., 1988, Compositions and sources of mineralizing fluids for chimney and manto limestone-replacement ores in Mexico: Economic Geology, v. 83, p. 1985-1992.
Heizler, M. T., Lux, D. R., and Decker, E. R., 1988, The age and cooling history of the Chain of Ponds and Big Island Pond plutons and the Spider Lake Granite, West-Central Maine and Quebec: American Journal of Science, v. 288, p. 925-952.
Hewett, D. F., and Radtke, A. S., 1967, Silver-bearing black calcite in western mining districts: Economic Geology, v. 62, p. 1-21.
Hewitt, W. P., 1968, Geology and Mineralization of the Main Mineral Zone of the Santa Eulalia District, Chihuahua, Mexico: Society of Mining Engineers, Transactions.
Huneke, J. C., and Smith, S. P., 1976, The realities of recoil: 39Ar recoil out of small grains and anomalous age patterns in 40Ar/39Ar dating: Geochim. Cosmochim. Acta, v. 7, p. 1987-2008 (Suppl.).
Kimball, J. P., 1870, The silver mines of Santa Eulalia District, Chihuahua, Mexico: American Journal of Science, 2nd Series, v. 49, p. 161-175.
King, W. E., and Kelley, R. E., 1980, Geology and paleontology of Tortugas Mountain, Dona Ana County, New Mexico: New Mexico Geology, v. 2, p. 33-35.
Lippolt, H. J., and Hautmann, S., 1995, 40Ar/39Ar ages of Precambrian manganese ore minerals from Sweden, India and Morocco: Miner. Deposita, v. 30, p. 246-256.
Lueth, V. W., Chamberlin, R. M., and Peters, L., 2004, Age of mineralization in the Luis Lopez manganese district, Socorro County, New Mexico, as determined by 40Ar/39Ar dating of cryptomelane: New Mexico Bureau of Mines and Mineral Resources, Bulletin, p. 239-249.

Lueth, V. W., Lucas, S. G., Giles, K. A., Kues, B. S., and Witcher, J., 2002, Third-day road log, from Alamogordo to White Sands, San Agustin Pass, Organ Quarry, and Tortugas Mountain: New Mexico Geological Society 2002 Field Conf.Guidebook.

Lueth, V. W., Megaw, P. K. M., Pingitore, N. E., and Goodell, P. C., 2000, Systematic Variation in Galena Solid-Solution Compositions at Santa Eulalia, Chihuahua, Mexico: Economic Geology, v. 95, p. 1673-1687.

Lueth, V. W., Rye, R. O., and Peters, L., 2005, "Sour gas" hydrothermal jarosite: ancient to modern acid-sulfate mineralization in the southern Rio Grande Rift: Chemical Geology, v. 215, p. 339-360.

Mailloux, B., Person, M., Kelley, S., Dunbar, N., Cather, S., Strayer, L., and Hudleston, P., 1999, Tectonic controls on the hydrogeology of the Rio Grande Rift, New Mexico: Water Resour. Res., v. 35, p. 2641-2659.

Malakhov, A. A., 1968, Bismuth and antimony in galenas as indicators of some conditions of ore formation: Geochemistry International, v. 7, p. 1055-1068.

Mauger, R. L., 1981, Geology and petrology of the central part of the Calera-del Nido Block, Chihuahua, Mexico: in Uranium in Volcanic and Volcaniclastic Rocks, Goodell, P. C. and Waters, A. C., editors, AAPG Studies in Geology No. 13, p. 205-242.

Mauger, R. L., 1983a, A geologic study of the Providencia-el Nido Area, Northeast flank of Sierra del Nido, Central Chihuahua, Mexico: El Paso Geological Society 1983 Field Conf., p. 187-193.

Mauger, R. L., 1983b, The geology and volcanic stratigraphy of the Sierra Sacramento block near Chihuahua City, Chihuahua, Mexico: El Paso Geological Society 1983 Field Conf. Guidebook, p. 137-156.

McLemore, V. T., Giordano, T. H., Lueth, V. W., and Witcher, J. C., 1998, Origin of barite-fluorite-galena deposits in the southern Rio Grande Rift, New Mexico: New Mexico Geological Society 1998 Field Conf.Guidebook, p. 251-263.

Megaw, P. K. M., 1986a, Argentiferous manganese-oxide alteration in wall and capping rocks of the Santa Eulalia District, Chihuahua, Mexico: Geologic Society of America, Abstract w/ Programs.

Megaw, P. K. M., 1986b, Geology and Geologic History of the Santa Eulalia Mining District, Chihuahua, Mexico: in Clark, K.F., Megaw, P.K.M., and Ruiz, J., eds., Lead-Zinc-Silver Carbonate -Hosted Deposits of northern Mexico: Society of Economic Geology Guidebook, Nov. 13-17, 1986, p. 213-232.

Megaw, P. K. M., 1986c, Mineralogy of the Santa Eulalia Mining District, Chihuahua, Mexico: Rochester Acad. Sci. 13th Mineral. Symposium, April 10-13, p. 21-31.

Megaw, P. K. M., 1987, Oxygen and carbon isotopic shifts between altered and unaltered limestone in the peripheries of the Santa Eulalia Mining District, Chihuahua, Mexico: Geologic Society of America, Abstract w/ Programs, v. 19, p. 769.

Megaw, P. K. M., 1990, Geology and Geochemistry of the Santa Eulalia Mining District, Chihuahua, Mexico: Unpub. PhD thesis, The University of Arizona, 461 p.

Megaw, P. K. M., and McDowell, F. W., 1983, Geology and geochronology of volcanic rocks of the Sierra Pastorias Caldera Area, Chihuahua, Mexico: El Paso Geol. Soc. Guidebook for the Fall Field Conf. Oct. 7-9, p. 195-204.

Mexicana, Sociedad Geologica, 1985, Plano Geologica Minero, Chihuahua, Mexico, Sociedad Geologica Mexicana A. C., Delegacion Chihuahua.
Miranda, M. A. G., and Megaw, P. K. M., 1986, Magmatic-Hydrothermal Breccias and Certain Silver-Lead-Zinc Chimnies of the Potosi Mine, Santa Eulalia District, Chihuahua, Mexico: in Clark, K.F., Megaw, P.K.M., and Ruiz, J., eds., Lead-Zinc-Silver Carbonate -Hosted Deposits of northern Mexico: Society of Economic Geology Guidebook, Nov. 13-17, 1986, p. 255-278.
Miura, H., 1986, The crystal structure of hollandite: Mineral. J., v. 13, p. 119-129.
Norman, D. I., Bazrafshan, K., and Eggleston, T. L., 1983, Mineralization of the Luis Lopez epithermal manganese deposits in light of fluid inclusion and geologic studies: in Chapin, C. E., and Callender, J. F. (eds.), Socorro region II: New Mexico Geological Society, Guidebook 34, p. 247-251.
Ohmoto, H., 1972, Systematics of sulfur and carbon isotopes in hydrothermal ore deposits: Economic Geology, v. 67, p. 551-579.
Ohmoto, H., and Rye, R. O., 1979, Isotopes of sulfur and carbon: in Barnes, H. L., eds.: Geochemistry of Hydrothermal Ore Deposits, p. 509-567.
Pingitore Jr., N. E., Stege, B. M., Goodell, P. C., and Lemone, D. V., 1983, Limestone stratigraphy, Central Sierra Pena Blanca, Chihuahua, Mexico: El Paso Geological Society 1983 Field Conf., p. 239-246.
Post, J. E., and Bish, D. L., 1988, Rietveld refinement of the todorokite structure: Am. Mineral, v. 73.
Post, J. E., Veblen, D. R., 1990, Crystal structure and determinations of synthetic sodium, magnesium, and potassium birnessite using TEM and the Rietveld method: Am. Mineral, v. 75.
Pracejus, B., 1989, Nature and Formation of Supergene Manganese Deposits on Groote Eylandt, N. T., Australia., University of Adelaide, 231 p.
Prescott, B., 1910, Report on the fissure systems of Mina Vieja: unpub. private rept. to ASARCO Mexicana, Oct. 15, 1910, 16p.
Prescott, B., 1916, The Main Mineral Zone fo the Santa Eulalia District: American Institute of Mining Engineers Transactions, v. 51, p. 57-99.
Radtke, A. S., Taylor, C. M., and Hewett, D. F., 1967, Aurorite, argentian todorokite, and hydrous silver-bearing lead manganese oxide: Economic Geology, v. 62, p. 186-206.
Renne, P. R., Swisher, C. C., Deino, A. L., Karner, D. B., Owens, T. L., and Depaolo, D. J., 1998, Intercalibration of standards: absolute ages and uncertainties in $^{40}Ar/^{39}Ar$ dating: Chemical Geology, v. 145, p. 117-152.
Rice, C. T., 1908, The ore deposits of Santa Eulalia, Mexico: Eng. Mining Jour., v. 85, p. 1229-1233.
Ruffet, G., Innocent, C., Michard, A., Feraud, G., and Beauvais, A., 1996, A geochronological 40Ar/39Ar and 87Rb/86Sr study of K-Mn oxides from the weathering sequence of Azul, Brazil: Geochim. Cosmochim. Acta, v. 60, p. 2219-2232.
Seager, W. R., Hawley, J. W., and Clemons, R. E., 1971, Geology of San Diego Mountain Area Dona Ana County, New Mexico: New Mexico Bureau of Mines and Mineral Resources, Bulletin, v. 97.

Segev, A., Halicz, L., Lang, B., and Steinitz, G., 1991, K-Ar dating of mangenese minerals from the Eisenbach region, Black Forest, southwest Germany: Schweiz. Mineral. Petrogr. Mitt., v. 71, p. 101-114.

Spurr, J. E., 1911, Geology of the Main Mineral Belt of Santa Eulalia District, Chihuahua, Mexico, unpublished report to American Smelting and Refining Co., p. 46.

Tsuji, M., Komarneni, S., and Abe, M., 1993, Ion exchange selectivity for alakali metal ions on a cryptomelane-type hydrous manganese dioxide: Solvent Extr. Ion. Exch., v. 11, p. 143-158.

Varentsov, I. M., and Golovin, D. I., 1987, Manganese beds of Groote Eylandt, nothern Australia: K/Ar dating of cryptomelane minerals and genetic aspects: Dokl. Akad. Nauk USSR, v. 294, p. 203-207.

Vasconcelos, P. M., 1992, Timing and rates of evolution of hydrochemical systems in semi-arid and humid environments by application of 40K-40Ar and laser-heating 40Ar/39Ar dating of K-bearing weathering product minerals, University of California, 242 p.

Vasconcelos, P. M., 1999, K-Ar and 40Ar/39Ar geochronology of weathering processes: Annu. Rev. Earth Planet Sci., v. 27, p. 183-229.

Vasconcelos, P. M., Becker, T. A., Renne, P. R., and Brimhall, G. H., 1992, Age and duration of weathering 40K-40Ar and 40Ar/39Ar analysis of K-Mn Oxides: Science, v. 258, p. 451-455.

Vasconcelos, P. M., Becker, T. A., Renne, P. R., and Brimhall, G. H., 1994a, Direct dating of weathering phenomena by K-Ar and 40Ar/39Ar analysis of supergene K-Mn oxides: Geochim. Cosmochim. Acta, v. 58, p. 1635-1665.

Vasconcelos, P. M., Renne, P. R., Becker, T. A., and Wenk, H. R., 1995, Mechanisms and kinetics of atmospheric, radiogenic, and nucleogenic argon release from cryptomelane during 40Ar/39Ar analysis: Geochim. Cosmochim. Acta, v. 59, p. 2057-2070.

Vasconcelos, P. M., Wenk, H. R., and Echer, C., 1994b, In situ study of the thermal behavior of cryptomelane by high voltage and analytical elctron microscopy: Am. Mineral, v. 79, p. 80-90.

Veizer, J., and Hoefs, J., 1976, The Nature of 18O/16O and 13C/12C Secular Trends in Sedimentary Carbonate Rocks: Geochimica et Cosmochimica Acta, v. 40, p. 1387-1395.

Walker, R. T., and Walker, W. J., 1956, The Origin and Nature of Ore Deposits: Walker Association, p. 130-131.

Walter, T. G., 1985, Metals distribution at the San Antonio mine, Santa Eulalia mining district, Chihuahua, Mexico: Unpublished M.S. thesis, Tuscon, AZ, University of Arizona, 102 p.

Witcher, J. C., 1998, The Ricon SLH1 Geothermal Well: New Mexico Geological Society 1998 Field Conf.Guidebook, p. 35-40.

Yahvili, L. P., and Gukasyan, R. K., 1974, Use of cryptomelane for potassium-argon dating of manganese ore of the Sevkar-Sarigyukh Deposit, Armenia: Trans. Acad. Sci. USSR Dokl. Earth Sci. Sect., v. 212, p. 49-51.